

AD A 054023

18

19

AFML TR-77-163

FOR FURTHER TRAN

(1)

6

Fracture Mechanics for Structural Adhesive Bonds. - Final Report

10

T. R./Brussat S. T./Chiu/Lockheed-California Company
S./Mostovoy/Materials Research Laboratory, Inc.
Glenwood, Illinois 60425

DDC FILE COPY

Lockheed-California Company
A Division of Lockheed Corporation
Burbank, California 91520

DDC
MAY 12 1978
F

11

Oct 1977

12 126 p.

Technical Report AFML-TR-77-163

9

Final Report 15 Jun 1975 - 15 Jul 1977

14

LR-28196

15

F 33615-75-C-5224

16 4864

17 $\phi\phi$

Approved for public release: distribution unlimited

63211F

Prepared for

AIR FORCE MATERIALS LABORATORY
AIR FORCE WRIGHT AERONAUTICAL LABORATORIES
AIR FORCE SYSTEMS COMMAND
WRIGHT-PATTERSON AIR FORCE BASE, OHIO 45433

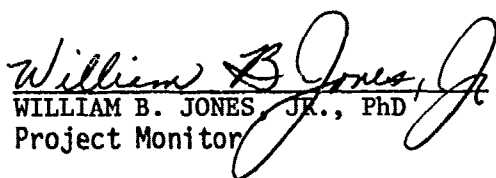
209 970

mt

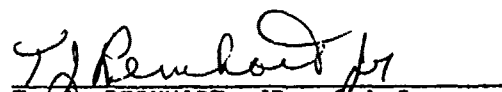
NOTICE

When Government drawings, specifications, or other data are used for any purpose other than in connection with a definitely related Government procurement operation, the United States Government thereby incurs no responsibility nor any obligation whatsoever; and the fact that the government may have formulated, furnished, or in any way supplied the said drawings, specifications, or other data, is not to be regarded by implication or otherwise as in any manner licensing the holder or any other person or corporation, or conveying any rights or permission to manufacture, use, or sell any patented invention that may in any way be related thereto.

This technical report has been reviewed and is approved for publication.


WILLIAM B. JONES, JR., PhD
Project Monitor

FOR THE COMMANDER


T. D. REINHART, JR., Chief
Composite & Fibrous Matls Branch
Nonmetallic Materials Division

J. M. KELBLE, Chief
Nonmetallic Materials Division

Copies of this report should not be returned unless return is required by security considerations, contractual obligations, or notice on a specific document.

UNCLASSIFIED

①

SECURITY CLASSIFICATION OF THIS PAGE (When Data Entered)

REPORT DOCUMENTATION PAGE		READ INSTRUCTIONS BEFORE COMPLETING FORM
1. REPORT NUMBER AFML-TR-77-163	2. GOVT ACCESSION NO.	3. RECIPIENT'S CATALOG NUMBER
4. TITLE (and Subtitle) FRACTURE MECHANICS FOR STRUCTURAL ADHESIVE BONDS - FINAL REPORT		5. TYPE OF REPORT & PERIOD COVERED 15 June 1975 - 15 July 1977
		6. PERFORMING ORG. REPORT NUMBER LR 28196
7. AUTHOR(s) T. R. Brussat and S. T. Chiu, (Lockheed-California Company) and S. Mostovoy (Materials Research Laboratory, Inc., Glenwood, Illinois 60425)		8. CONTRACT OR GRANT NUMBER(s) F33615-75-C-5224 <i>new</i>
9. PERFORMING ORGANIZATION NAME AND ADDRESS LOCKHEED-CALIFORNIA COMPANY Burbank, California 91520		10. PROGRAM ELEMENT, PROJECT, TASK AREA & WORK UNIT NUMBERS 486U0009
11. CONTROLLING OFFICE NAME AND ADDRESS Air Force Materials Laboratory/Code FY-1457 Air Force Systems Command Wright-Patterson Air Force Base, Ohio 45433		12. REPORT DATE October 1977
		13. NUMBER OF PAGES 125
14. MONITORING AGENCY NAME & ADDRESS (if different from Controlling Office)		15. SECURITY CLASS (of this report) UNCLASSIFIED
		15a. DECLASSIFICATION/DOWNGRADING SCHEDULE
16. DISTRIBUTION STATEMENT (of this Report) Approved for public release: distribution unlimited.		
17. DISTRIBUTION STATEMENT (of the abstract entered in Block 20, if different from Report)		
18. SUPPLEMENTARY NOTES		
19. KEY WORDS (Continue on reverse side if necessary and identify by block number)		
Fracture Mechanics Adhesive Bond Test Specimens Fracture Properties	Crack Propagation Fatigue Testing Sustained Load Testing Analysis Bonded Joints	ic Testing Finite Element Flaw Growth Monitoring Ultrasonic NDI
20. ABSTRACT (Continue on reverse side if necessary and identify by block number)		
<p>Tests and analyses were conducted to develop and demonstrate the fracture mechanics methodology to predict the growth of bondline flaws in adhesively bonded primary aircraft structure. The development and use of a new baseline specimen for testing bondline cracks in combined Modes I and II is described. Specimen development work on other adhesive fracture mechanics specimens including combined Modes I and III is described. Fracture mechanics data for AF-55S adhesive are presented covering fatigue, sustained and monotonically</p>		

DDC
RECEIVED
MAY 12 1978
F

increasing loading, in laboratory air and hot water, in Pure Mode I, and mixed Modes I and II.

Adhesive bondline crack growth data are presented from fatigue tests of larger structural bonded single lap joints with initial bondline flaws. Techniques are demonstrated for growth monitoring both ultrasonically and by a compliance technique. A fracture mechanics analysis estimate of bondline crack growth rates in these tests is described, and the estimated rates are compared to the actual monitored crack growth rates.

Based on this work an evaluation is made of fracture mechanics methodology as applied to bondline cracks in adhesively bonded aircraft structure.

BY
AVAILABILITY CODES
SPECIAL
A

FOREWORD

This document describes the research conducted for the Air Force Materials Laboratory (AFML) to fulfill the Phase I objectives of Contract F33615-75-C-5224. The Structural Methods Group of Lockheed-California Company had primary responsibility for the project. Materials Research Laboratory (MRL) was the major subcontractor and performed the experimental specimen development and baseline testing.

The continuing support and cooperation of Dr. W. B. Jones, the responsible AFML technical monitor, is appreciated. The technical involvement and consultation of A. C. Novelli and his broad expertise in aircraft structural adhesive bonding has been an asset to the program. Dr. E. J. Ripling of MRL and E. K. Walker of Lockheed are acknowledged for their leadership and, in particular, for maintaining the spirit of cooperation between the two companies.

Some others at Lockheed who made significant contributions are hereby acknowledged: A. L. Pulido for his workmanship in the bonding of test specimens; D. E. Pettit for coordination of structural testing; W. G. Browne and R. R. Sederman for guidance in program management and administration; R. J. Van Ness, Mae Roosman, and Shirley Nash for their assistance in preparation of reports; and J. C. Wordsworth and J. C. Ekvall of the Structural Methods Group for their technical consultation and support.

In Phase II of this AFML contract, Lockheed and MRL are currently extending the results reported herein to FM-73, the adhesive selected for the PABST program.

NO.
 Preceding Page BLANK - FILM

TABLE OF CONTENTS

SECTION		PAGE
	FOREWORD	ili
	LIST OF ILLUSTRATIONS	vii
	LIST OF TABLES	x
I	INTRODUCTION	1
II	SPECIMEN DEVELOPMENT	5
	1 ANALYSIS OF THE CRACKED LAP SHEAR (CLS) SPECIMEN	10
	1.1 Total Strain Energy Release Rate	15
	1.2 Beam Bending Solution	16
	1.3 Estimation of G_I	18
	2 TEST METHODS FOR THE CLS SPECIMEN	21
	2.1 Fatigue Test Method	21
	2.2 Side Notching for Increasing-Load Testing	23
	2.3 Special Test Methods for Environmental Tests	29
	3 DEVELOPMENT WORK ON OTHER SPECIMENS	30
	3.1 The Width-Tapered Beam (WTB) Specimen	30
	3.2 Diagonal Loading of the CDCB Specimen	33
	3.3 Beam and Column (BC) Specimen	35
	3.4 The Mode III Test Specimen	40
III	BASELINE TESTING	47
	1 INCREASING LOAD TESTS	47
	1.1 Mode I (G_{Ic}) Tests	47
	1.2 Mixed Mode I and Mode II Tests	47
	2 SUSTAINED LOAD STRESS CORROSION CRACKING TESTS	53
	2.1 Mode I SCC Testing	53
	2.2 Mixed Mode SCC Testing	55

TABLE OF CONTENTS (Continued)

SECTION	PAGE	
3	FATIGUE TESTS	57
3.1	Mode I Testing in Laboratory Air at 3 Hz	58
3.2	Mixed-Mode Testing in Laboratory Air at 3 Hz	60
3.3	Elevated Temperature Fatigue Testing	63
3.4	High Frequency Testing	63
3.5	Discussion of Baseline Fatigue Test Results	66
IV	METHODOLOGY DEMONSTRATION	71
1	TEST PROGRAM	72
1.1	Thick-Adherend Single Lap Joint Tests	72
1.1.1	Specimen Configuration and Fabrication	72
1.1.2	Crack Growth Monitoring	74
1.2	Thin-Adherend Single Lap Joint Tests	75
2	ANALYSIS OF THE SINGLE LAP JOINT SPECIMENS	82
2.1	Thick-Adherend Specimens	82
2.2	Thin-Adherend Specimens	88
3	TEST RESULTS AND DISCUSSIONS	94
3.1	Thick-Adherend Specimens	94
3.2	Thin-Adherend Specimens	97
V	CONCLUSIONS AND RECOMMENDATIONS	111
	REFERENCES	117

LIST OF ILLUSTRATIONS

Figure		Page
1	Contoured double-cantilever beam (CDCB) specimen for pure mode I testing	6
2	Cracked lap shear specimen (CLS) for combined Mode I and mode II loading	7
3	Width tapered beam (WTB) specimen for mode I testing	9
4	Combined $\mathcal{G}_I - \mathcal{G}_{II}$ test grips for CDCB specimen	10
5	Beam and column (BC) specimen for mixed modes I, II, and III testing	11
6	MZKG specimen for mode III testing	12
7	Mode mix for baseline specimens	13
8	CLS specimen and its deformed shape	14
9	Symmetric and antisymmetric component problems for the cracked lap shear specimen in bending	19
10	Three views of specimen CLS-1	22
11	CLS specimen load-displacement curves	24
12	Increasing load test record for side-notched specimen CLS-1	25
13	Load-displacement record for specimen CLS-3	28
14	Width-tapered beam (WTB) specimen shown with gripping bolts	33
15	Load-displacement record for width-tapered beam specimen (WTB-1)	34
16	Single actuator test assembly for two-axis loading of BC specimens	36
17	Close-up view of mode I - mode II test frame	37
18	MZKG specimen with $M_o = 1.89 \text{ mm}^{-1}$ (48 inch^{-1}) for mode II testing	41
19	Cross section of the MZKG specimen	42
20	Overlap length, b_N , inches	44
21	Fracture surface photographs of MZKG specimens	45
22	Comparison of mode III fatigue crack growth curves for two overlap dimensions	46

LIST OF ILLUSTRATIONS (Continued)

Figure		Page
23	Fracture surface of specimen CLS-1	51
24	Magnified fracture surface photographs for specimen CLS-1	52
25	Pure mode I sustained-load crack growth	54
26	Pure mode I SCC Data in 327°K - 333°K (130°F - 140°F) Water	56
27	Mode I fatigue crack growth in room temperature air	59
28	Fatigue crack growth data from mixed-mode CLS specimens	62
29	CLS fatigue data using $\Delta\mathcal{G}_{eff}$ to account for mode II	64
30	Mode I fatigue crack growth rate data, RT air and 333°K (140°F) water immersion	55
31	Effect of 30 Hz frequency on crack growth in room temperature air	67
32	Structural single lap joint specimen with thick adherends	73
33	Compliance of SLJ specimen as computed by finite element analyses	76
34	Single lap joint (SLJ) specimen with thin adherends	77
35	Test setup for thin-adherend SLJ specimens in hot water	79
36	Environmental box and displacement gage	80
37	Compliance of thin-adherend SLJ specimen as computed by finite element method	81
38	Finite element model of the profile section of the test specimen	83
39	Distributions of bending moment in the splice plate	85
40	Calculated strain energy release rates at various bondline crack lengths	86
41	Finite length correction factor for a split beam subjected to uniform bending	87
42	Bending moment distributions for thin-adherend SLJ specimen	91
43	Estimated crack growth rates at two applied stress levels	93
44	Total lives of SLJ specimens with or without initial bondline flaws	95

LIST OF ILLUSTRATIONS (Continued)

Figure		Page
45	Bondline crack growth histories	96
46	Crack growth rate by ultrasonic and compliance measurements	98
47	Estimated and empirical crack growth rates	99
48	Final damage configuration, specimen A. No initial flaw	102
49	Final damage configuration, specimen B. No initial flaw	103
50	Final damage configuration, specimen C. Initial flaw a 7.6 mm (0.3 in.) deep across-the-width flaw	104
51	Final damage configuration, specimen D. Initial flaw is a 7.6 mm (0.3 in.) deep across-the-width flaw	105
52	Final damage configuration, specimen E. Initial flaw is a 12.7 mm (0.5 in.) wide longitudinal flaw at the center line	106
53	Final damage configuration, specimen F. Initial flaw is a 12.7 mm (0.5 in.) wide longitudinal flaw at the center line	107
54	Predicted and experimental bondline crack growth	108

LIST OF TABLES

Table		Page
1	Bondline Thicknesses of CDCB Specimens	48
2	\mathcal{C}_{Ic} Values for 36 CDCB Specimens of AF-55S Adhesive	49
3	CLS Specimen Dimensions	61
4	Conservative Fatigue Threshold Values by Extrapolation	69
5	Estimated Effective Strain Energy Release Rates, and Crack Growth Rates, Thick Adherend SLJ Specimen	80
6	Estimated Effective Strain Energy Release Rates and Crack Growth Rates, Thin Adherend SLJ Specimens	92
7	Test Lives, Thin-Adherend Single-Lap Joint	100

SECTION I

INTRODUCTION

Adhesive bonding has been used as a joining technique of secondary aircraft structural details for several decades. It offers the potential advantages of improved fatigue life, improved fail-safe capability, and reduced manufacturing costs (References 1, 2). With the development of improved adhesive systems, adherend surface treatment methods, and coating and sealing techniques, adhesive bonding is now being considered as an alternative to mechanical fasteners in primary aircraft structure. The United States Air Force is sponsoring an integrated series of programs under the general title of Primary Adhesively Bonded Structure Technology (PABST) to study the technical and economic feasibility of primary adhesively bonded structure.

The Air Force aircraft structural integrity program document MIL-STD-1530A requires that the growth of initial flaws be considered in the design of primary structure. MIL-STD-1530A specifies that damage tolerance design of mechanically fastened metallic structure must meet the requirements of USAF Specification MIL-A-83444, "Damage Tolerance Design Requirements." However, the necessary fracture mechanics technology has not been developed to apply the philosophy and requirements of MIL-A-83444 to bondline cracks (or flaws) in adhesively bonded structure.

In order to apply fracture mechanics technology to predict the growth of bondline cracks, it is important to understand the three crack tip loading modes. The local stresses near the tip of any crack consist of three independent components, Modes I, II, and III. The Mode I or opening mode stresses result from tensile loading normal to the crack plane, tending to separate the crack surfaces. The Mode II or sliding-mode stresses result from shear loading

perpendicular to the leading edge of the crack. The Mode III or tearing-mode stresses result from shear loading parallel to the leading edge of the crack.

The strain energy release rate, \mathcal{G} , for a cracked body is defined as the change in the strain energy of the body per unit of crack extension. If W is the total strain energy and A is the fracture surface area of the extending crack, then

$$\mathcal{G} = \frac{\partial W}{\partial A} \quad (1)$$

The total strain energy release rate consists of the sum of the components due to Mode I, Mode II, and Mode III loading; that is

$$\mathcal{G} = \mathcal{G}_I + \mathcal{G}_{II} + \mathcal{G}_{III} \quad (2)$$

A substantial amount of fracture mechanics testing of structural adhesives had preceded the work reported herein (e.g., References 3 - 7). This testing was almost exclusively performed in Pure Mode I using double cantilever beam-type specimens.

Unlike cracks in homogeneous metals, which tend to align themselves in a direction normal to the maximum principal tension stress and propagate subsequently in Pure Mode I, adhesive bondline cracks are constrained in their orientation to follow the bondline direction. Thus a bondline crack can (and in large area bonds in fuselage structure it often will) have a high percentage of Mode II or III loading, compared to Mode I.

The preponderance of shear in the bondline of adhesive bonded structure demands that simple mixed mode test specimens containing bondline cracks be developed for damage tolerance testing. Ideally, these specimens should simulate bonded structure, the cracks should be measurable, and a fracture mechanics analysis should be developed to quantitatively relate the specimen to the structure.

Using such specimens, prediction methodology should then be developed to predict the growth of bondline flaws under cyclic loading over the full range of mode-mix that could occur in bonded primary aircraft structure. It should

be assured that the fundamental aspects of this methodology are applicable for any realizable service environment.

As part of the overall PABST effort, the research program reported herein was conducted to develop and demonstrate the fracture mechanics methodology needed to predict the growth of bondline flaws in adhesively bonded primary aircraft structure. In this research, new baseline fracture mechanics test specimens were developed for Modes I, II, III and mixed-mode loading as summarized in Section II. Then baseline fracture mechanics data were obtained on these specimens and on the Mode I CDCB specimen, as reported in Section III. Finally, a methodology for crack growth prediction was demonstrated on 12 tests of structural joints with initial bondline flaws, using baseline data and analytical estimates of the strain energy release rate, as presented in Section IV.

All tests in this program were done using bare 7075-T6 Aluminum sheet, plate and extrusion. Surface treatment was accomplished using a Phosphoric Acid Anodize process equivalent to Boeing's Specification 5555. The primer used was BR-127A, which is equivalent to BR-127 but easier to apply. The adhesive film was AF-55S ("S" meaning a scrim carrier was present). Unless otherwise stated the cure conditions were 389° - 400° K (240° - 260° F) and 276-345 kPa (40-50 psi) pressure.

Although regarded as an initial step, this program provides much of the technology required to assess the influence of pre-existent bondline flaws which may occur in adhesively bonded aluminum fuselage structure. It is shown that fracture mechanics methodology does provide a practical means for predicting flaw growth in adhesive bondlines.

SECTION II
SPECIMEN DEVELOPMENT

Because prior fracture mechanics testing had been limited to testing in Pure Mode I, the first major task in this program was to design and develop new baseline specimens and loading fixtures for cyclic and static testing of bondline cracks under substantially shear (Modes II and III) loading. For each specimen it had to be determined whether or not:

- The crack could be made to propagate
- Crack growth could be measured and monitored
- G_I , G_{II} , and G_{III} could be calculated

The effort involved specimen design, mathematical stress analysis, and the design of special loading fixtures, antibuckling supports, and load and crack-length monitoring setups.

In the development of new specimens, much was learned from the example of the Mode I contoured double-cantilever beam (CDCB) specimen, which had been a successful fracture mechanics specimen for years. The loading of this specimen (Figure 1) produces bending moments which tend to split the beams apart along the bondline. The beams are contoured such that the specimen compliance, C , increases linearly with increasing crack length ($\partial C/\partial A$ is constant). Since

$$G_I = \frac{P^2}{2} \frac{\partial C}{\partial A} \quad (3)$$

the strain energy release rate of the CDCB specimen is crack-length independent, varying only with the square of the applied load.

There are several advantages to this crack-length independence of G_I . First, the value of G_I can be obtained without knowing the crack length.

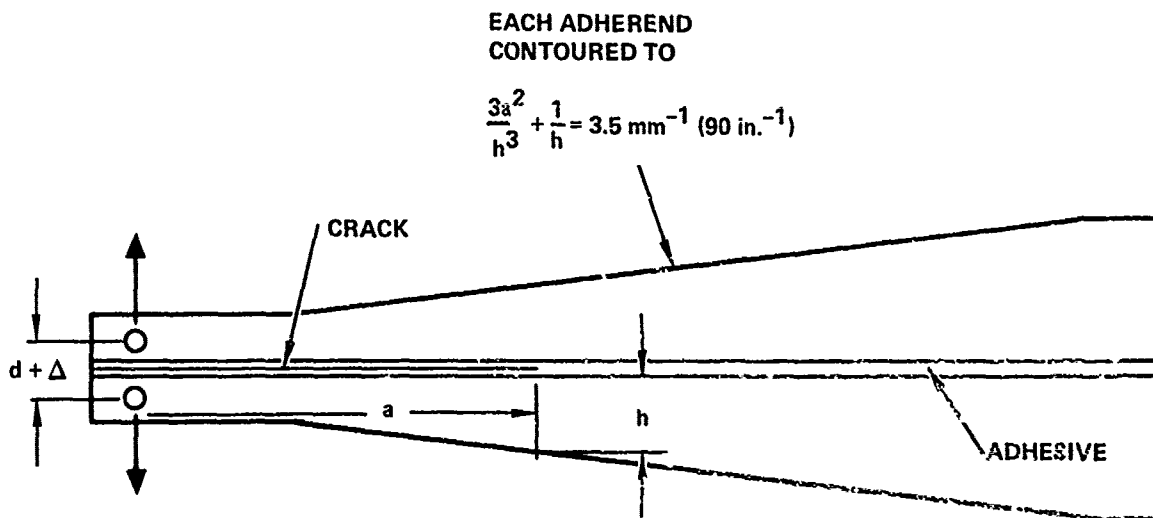


Figure 1. Contoured double-cantilever beam (CDCB) specimen for pure mode I testing

Secondly, because the compliance varies linearly with the crack length, the crack length is easily estimated from the measured displacement at the load point. This eliminates the necessity for visual monitoring of the crack, which is difficult and ambiguous for adhesives, or for some other more exotic, expensive crack-length monitoring method.

In addition to the crack-length independence of \mathcal{G} , a goal in the specimen development effort was that the specimens should, if possible, simulate structure in the method of loading. Also, since a large percentage of the bonds used in fuselage structure consists of large area bonded sheet, another goal was that the specimens could be easily machined from large-area bonded sheet or plate, thus optimizing the simulation of bondline thickness and bond quality. It was these goals that led to the development of the long cracked lap shear (CLS) specimen shown in Figure 2. The CLS specimen consists of a long piece bonded to a shorter piece. Tension is applied through pin loading to both pieces on one end and to just the longer piece on the opposite end. Because of its large

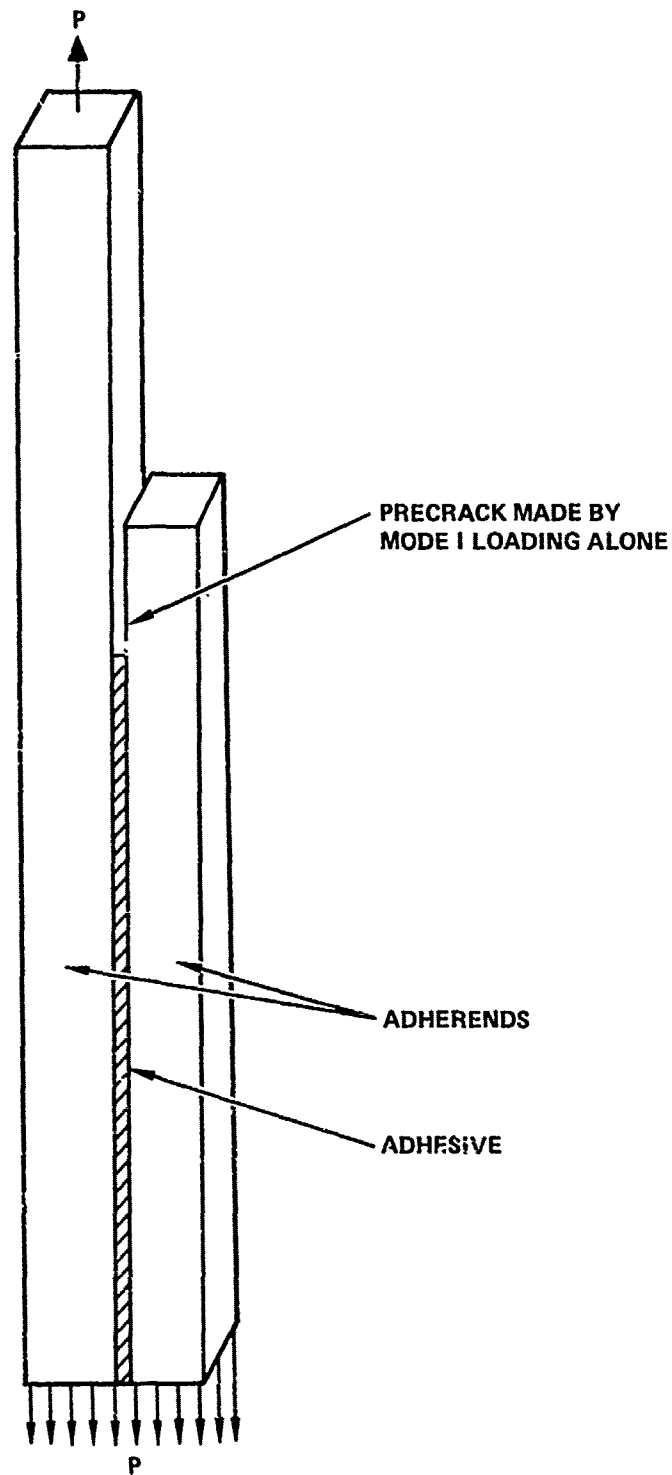


Figure 2. Cracked lap shear specimen (CLS) for combined mode I and mode II loading

length-to-thickness ratio the CLS specimen is a constant-strain-energy-release-rate specimen. The loading is applied parallel to the bondline so it has a substantial Mode II loading component. In addition, a significant Mode I component is induced by the eccentricity at the crack tip. The result is a mode mix fairly typical of bonded aircraft structure.

The CLS and CDCB specimens turned out to be the two primary baseline specimens used in this research program. A great deal of additional work was done on developing several other specimens.

A Pure Mode I specimen, the width-tapered beam (WTB) specimen shown in Figure 3, was developed late in the program primarily to overcome the problem of maintaining proper adhesive layer thickness encountered in the fabrication of the CDCB specimen. Like the CDCB specimen, the WTB specimen consists of two cantilever beams, contoured to vary the bending stiffness so as to provide a crack-length independent value of \mathcal{G}_I . In this specimen however, the beam height is constant and the width is tapered linearly. Thus it is possible to bond two large plates face to face and machine the specimens from the bonded plate, the same method that was used for the CLS specimens.

A special fixture (Figure 4) was designed and used to apply an oblique load to the CDCB specimen, inducing a small component (2 to 5 percent) of Mode II loading in addition to the Mode I.

The design concept for the beam-and-column (BC) specimen is shown in Figure 5. In concept, the specimen can be tested in any combination of Modes I, II and III. The vertical forces P , aligned with the bondline, induce pure \mathcal{G}_{II} . The concentrated moments M , applied independently of P , induce a selected combination of \mathcal{G}_I and \mathcal{G}_{III} . All three components of \mathcal{G} are crack-length independent.

The modified zero K-gradient (MZKG) specimen for Mode III testing is shown in Figure 6. In this specimen as in the CDCB, the contour leads to a constant strain energy release rate.

The triangular area in Figure 7 represents all the possible combinations of loading in Modes I, II and III. All of the baseline specimens considered

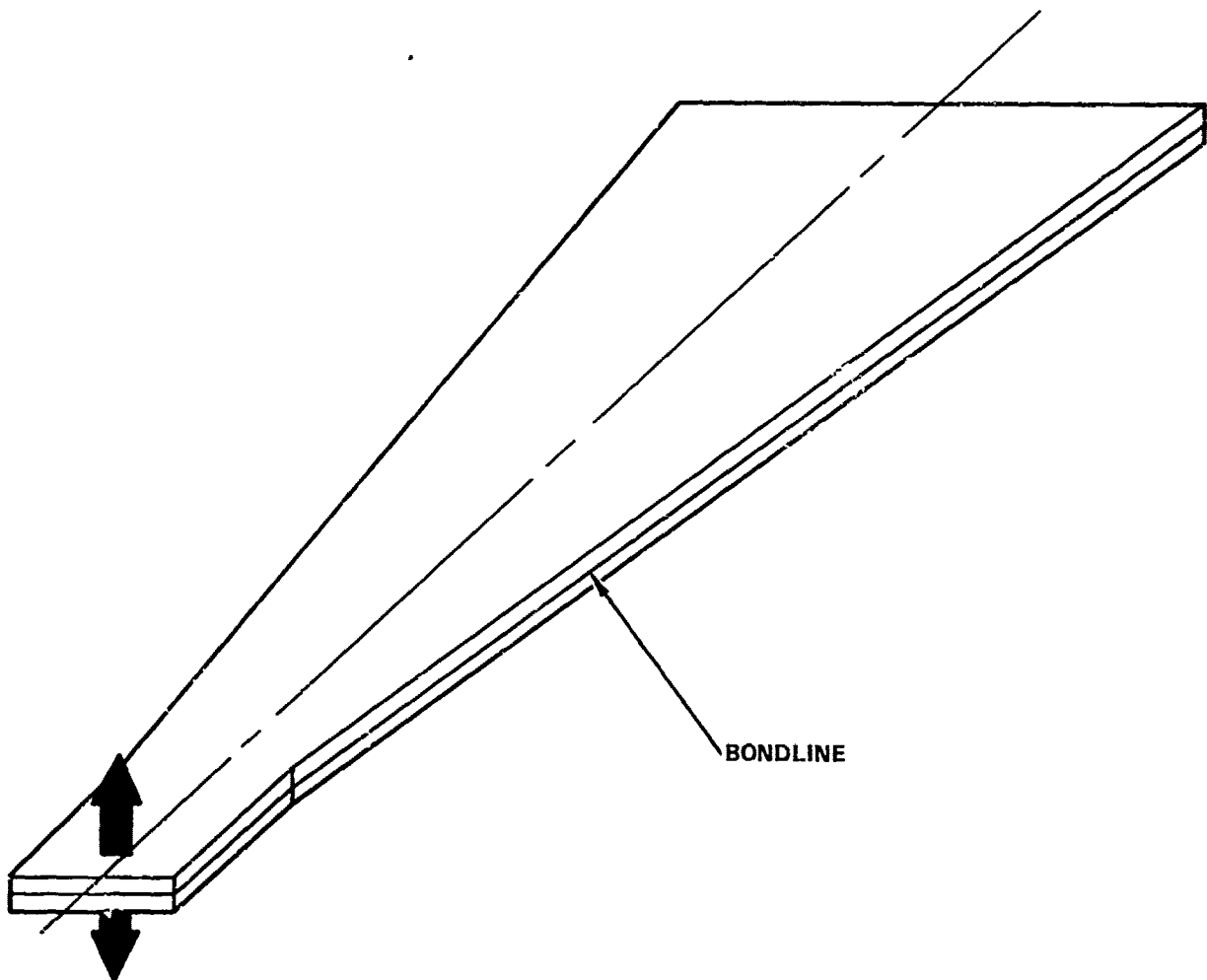


Figure 3. Width tapered beam (WTB) specimen for mode I testing

in this program are either Pure Mode specimens, covering corner points on the diagram, or combinations of 2 modes, covering regions on the boundaries of this diagram as shown. In concept, the BC specimen was supposed to have the capability to test combinations of all three modes covering the interior of the triangular region, but development of the BC specimen never successfully progressed beyond combinations of Modes I and II.

Subsection 1 presents the mathematical analyses for the CLS specimen, and Subsection 2 discusses the test equipment and procedures that were developed for the CLS specimen. The development of the WTB, diagonally-loaded CDCB,

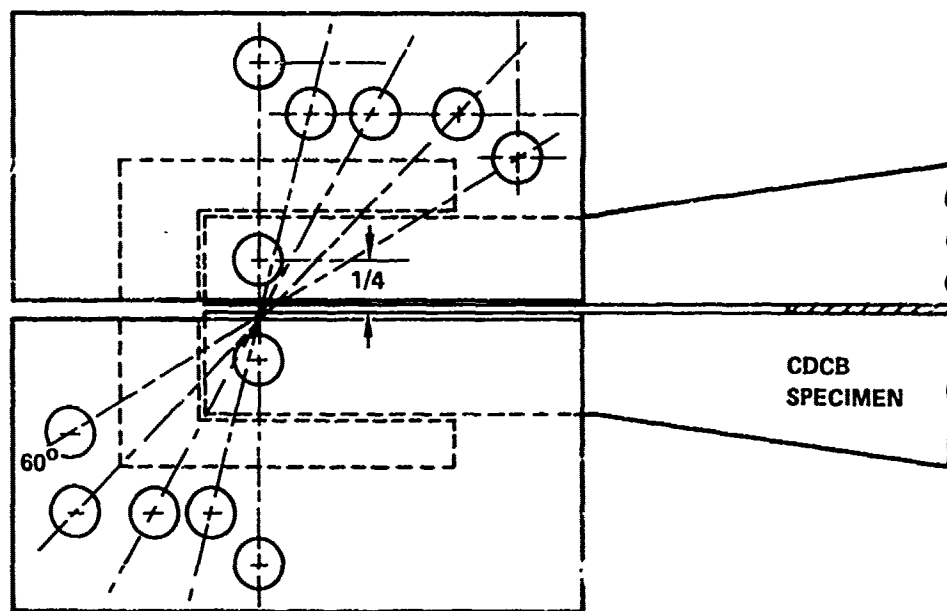


Figure 4. Combined $G_I - G_{II}$ test grips for CDCB specimen

BC, and MZKG specimens (as far as it progressed in each case) is discussed in Subsection 3.

1. ANALYSIS OF THE CRACKED LAP SHEAR (CLS) SPECIMEN

Major accomplishments in this research program have been the specimen development; fatigue, environmental sustained load, and increasing load testing; crack-growth monitoring; and mathematical stress analysis of the cracked lap shear (CLS) specimen. This specimen is extremely important to this program because, by its resemblance to typical bonded structure, the baseline data that it provides is most directly applicable to predicting the growth of bondline flaws in adhesively bonded structure. Also, since loading of the CLS is predominantly Mode II, predictions for structure over a wide range of combined Modes I and II can be obtained by simple interpolation between results from the CLS specimen and a Pure Mode I specimen like the CDCB or WTB.

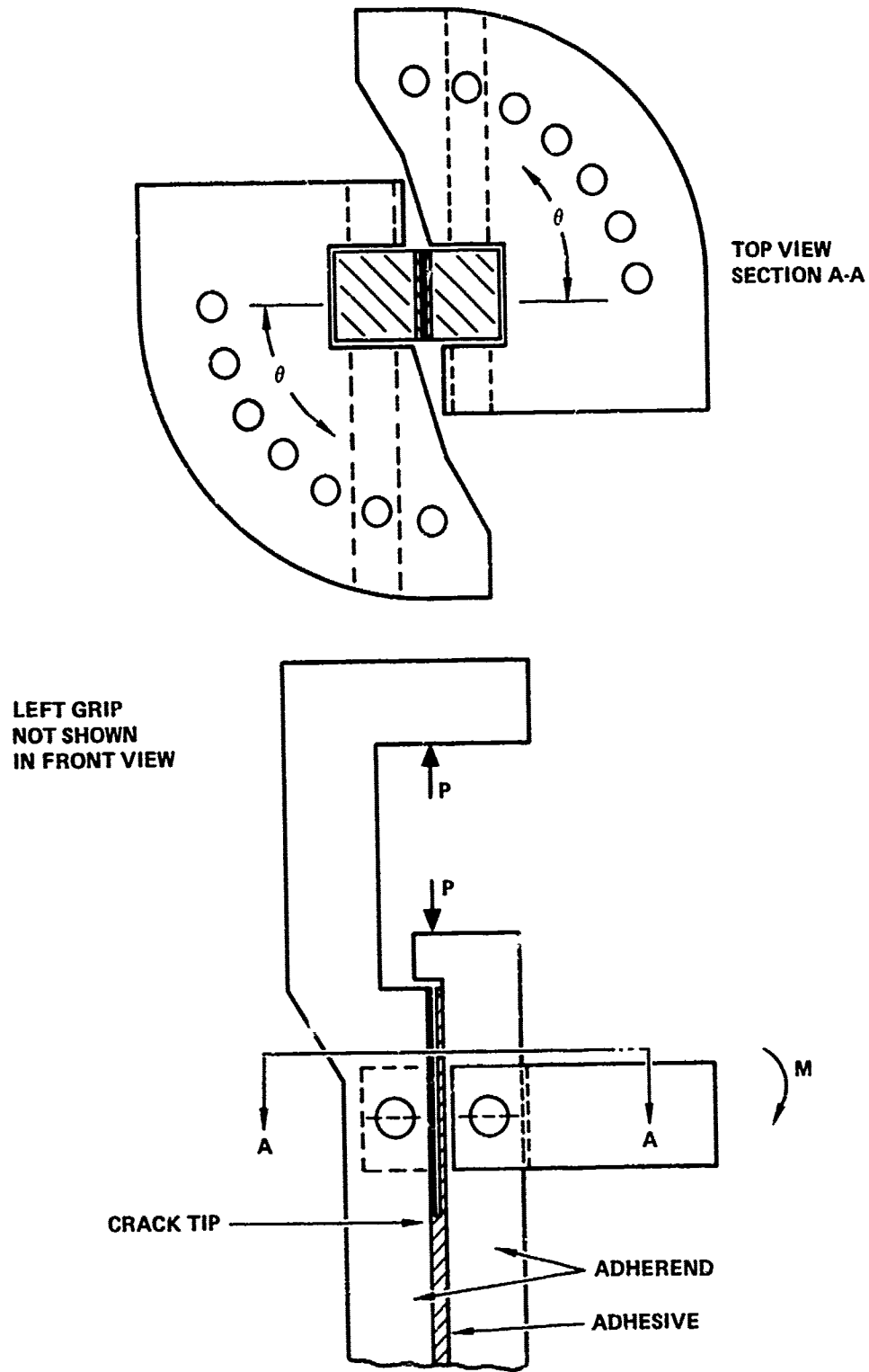


Figure 5. Beam and column (BC) specimen for mixed modes I, II, and III testing

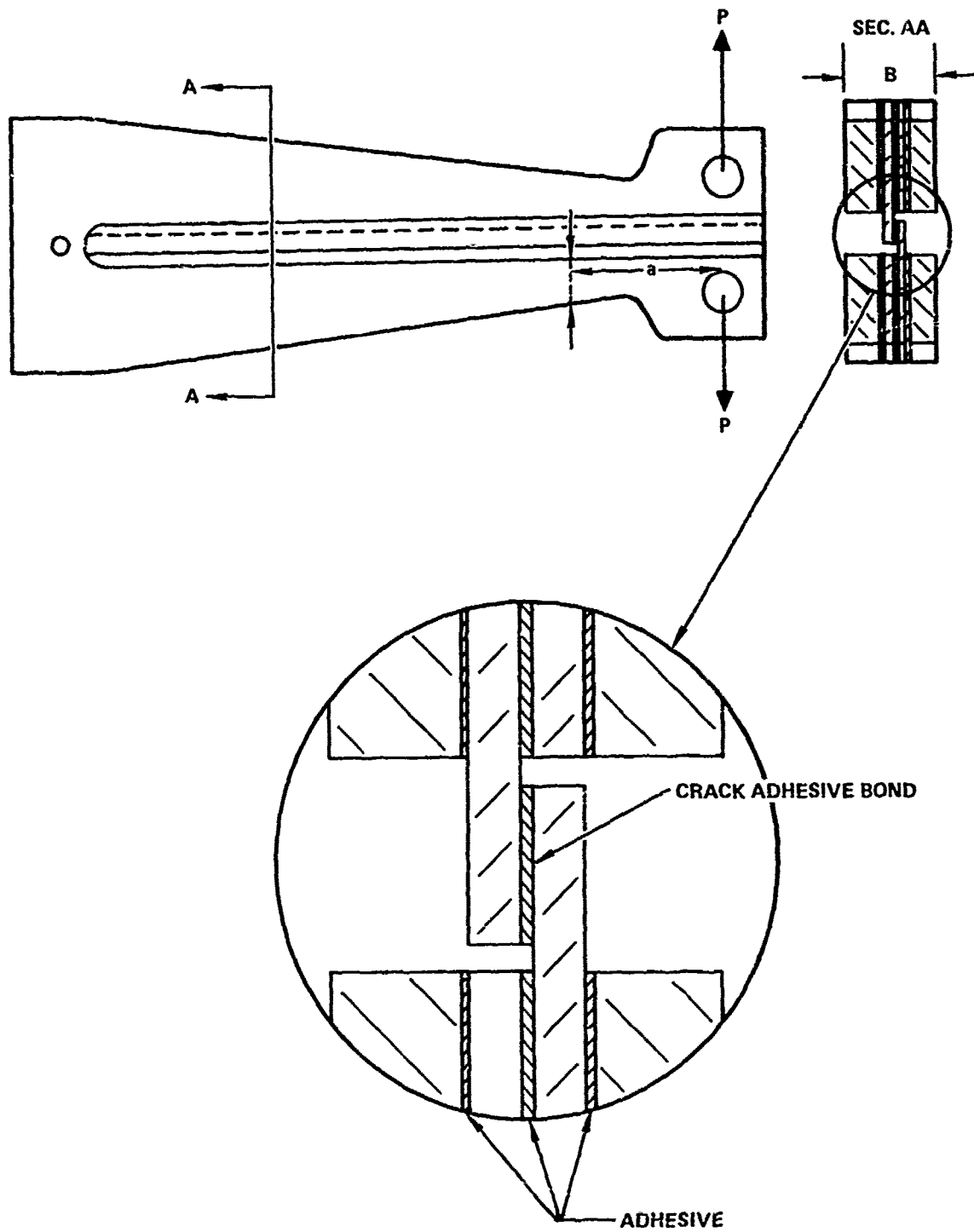


Figure 6. MZKG specimen for mode III testing

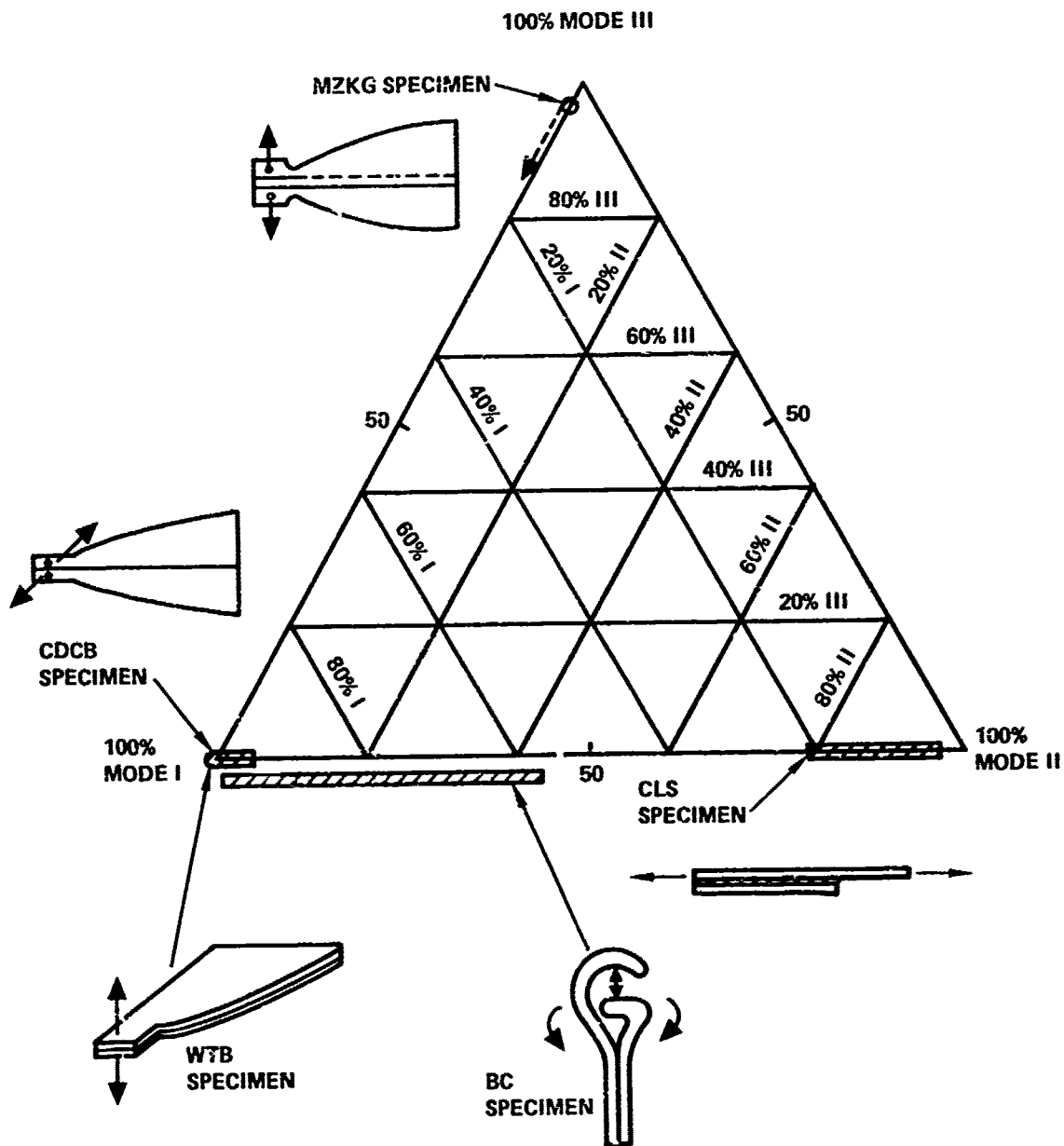


Figure 7. Mode mix for baseline specimens

The specimen is shown schematically in Figure 8(a). In general, the specimen may be side notched, so that the width b_N of the bondline may be less than the nominal width of the metal adherends. All the adherend materials, thicknesses, and cross-section shapes may differ from one another. Let $(EI)_2$ and $(EA)_2$ denote the bending and tensile stiffnesses of the single adherend on the right-hand end of the specimen. Likewise let $(EI)_0$ and $(EA)_0$ denote the bending and tensile stiffnesses of the two-layer beam at the left-hand end of the specimen. Let \bar{y}_2 be the location of the centroid on the right-hand end, and let \bar{y}_0 be the location (measured from the same reference axis) of the stiffness-adjusted centroid of the two-layer beam on the left-hand end.

On the left-hand end of the specimen the applied tensile load P distributes proportionally between the two adherends, while on the right-hand end, P is carried in adherend 2. As shown, the adhesive layer terminates at a crack tip. In addition to the obvious Mode II crack tip loading, there is a significant Mode I component due to the eccentricity of the load path at the crack tip.

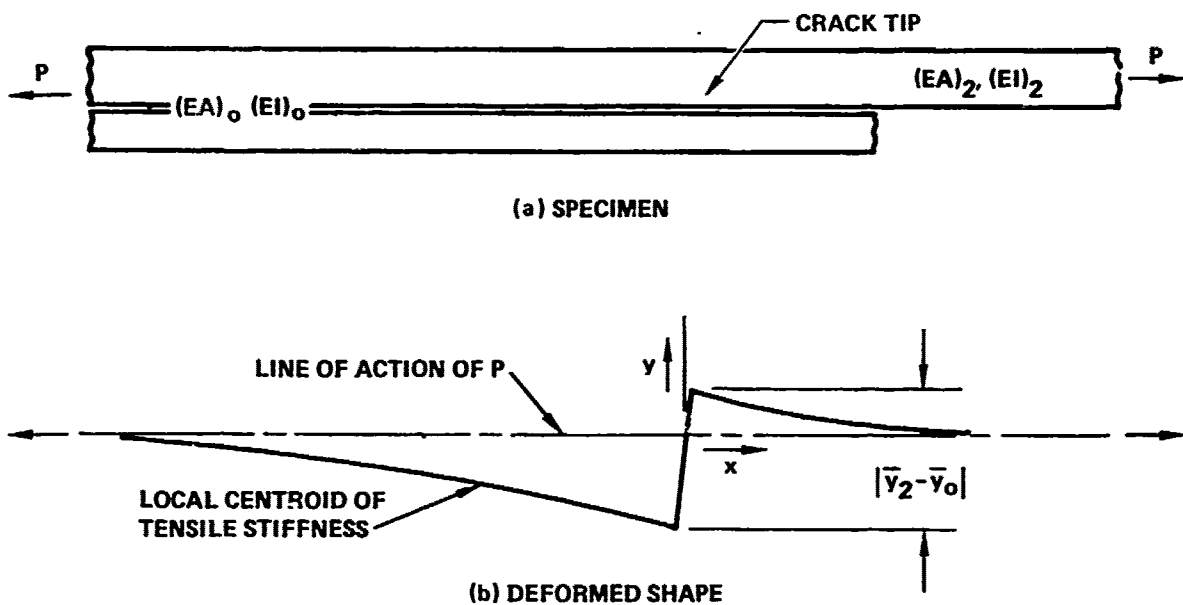


Figure 8. CLS specimen and its deformed shape

The analysis of the CLS specimen consisted of 3 parts. First, linear elasticity was utilized to develop an exact expression for the change in total strain energy per unit crack extension, which by definition is the total strain energy release rate, $\mathcal{G} = \mathcal{G}_I + \mathcal{G}_{II}$. Secondly, the induced bending moments were calculated by beam theory. Finally, the bending moments were used to estimate \mathcal{G}_I for the CLS specimen in tension, using an exact strain energy release rate analysis of the same specimen in pure bending.

1.1 Total Strain Energy Release Rate

When an increment of crack extension δa occurs in the CLS specimen, it causes a change δW in the total strain energy of the specimen. From Equation (1)

$$\mathcal{G} = \lim_{\delta a \rightarrow 0} \left(\frac{\delta W}{b_N \delta a} \right) \quad (4)$$

Consider a coordinate system fixed with respect to the crack tip. With respect to this coordinate system, nothing changes in the neighborhood of the crack tip when the crack grows. However, far to the left of the crack tip lies a uniformly strained volume of length δa that disappears when the crack elongates, and its strain energy is lost. Far to the right lies a uniformly strained volume of material of length δa that is added when the crack elongates, adding strain energy to the system. The strain energy change due to the crack growth increment δa is the difference between the strain energies within these two uniformly strained volumetric elements. Since the adhesive layer is very thin and compliant, its contribution to the strain energy can be neglected. Computing δW and substituting the result into Equation (4) leads to

$$\mathcal{G} = \frac{P^2}{2b_N(EA)_2} \left[1 - \frac{(EA)_2}{(EA)_0} \right] \quad (5)$$

1.2 Beam Bending Solution

Figure 8(b) shows schematically the way the centroidal axis of the CLS specimen deforms under the applied tensile load P . At the crack tip there is a finite change in the location of the centroidal axis. The magnitude of this step change is $\bar{y}_2 - \bar{y}_0$. As a result, the local centroid at any location x is offset a distance $y(x)$ from the line of action of the force P . With this offset there is, in addition to the uniform tension field, a local bending moment $M(x)$, given by

$$M(x) = P y(x) \quad (6)$$

By beam theory the bending moment is related to the second derivative of the deflection. This leads to a pair of second order differential equations for the deflection of the beam, $y(x)$, as follows:

$$y''(x) - \lambda_2^2 y(x) = 0, \quad x > 0 \quad (7)$$

$$y''(x) - \lambda_0^2 y(x) = 0, \quad x < 0 \quad (8)$$

where

$$\lambda_2 = \sqrt{P/(EI)_2} \quad (9)$$

$$\lambda_0 = \sqrt{P/(EI)_c} \quad (10)$$

The solution to Equations (7) and (8) must satisfy the following side conditions:

$$\lim_{|x| \rightarrow \infty} [y(x)] = \lim_{|x| \rightarrow \infty} [y'(x)] = 0 \quad (11)$$

$$\lim_{|x| \rightarrow 0} [y(|x|) - y(-|x|)] = \bar{y}_2 - \bar{y}_0 \quad a, b, c$$

$$\lim_{|x| \rightarrow 0} [y'(|x|) - y'(-|x|)] = 0$$

The following solution satisfies (7) (8), and (11):

$$y(x) = \frac{(\bar{y}_2 - \bar{y}_0) \lambda_0}{\lambda_2 + \lambda_0} e^{-\lambda_2 x}, \quad x \geq 0 \quad (12)$$

$$y(x) = \frac{-(\bar{y}_2 - \bar{y}_0) \lambda_2}{\lambda_2 + \lambda_0} e^{\lambda_0 x}, \quad x < 0$$

a, b

The separation of the two adherends at a distance (a) to the right of the crack tip is monitored during testing as a measurement of crack length, and is given by

$$\Delta(a) = y(a) - \lim_{|x| \rightarrow 0} [ay'(|x|) + y(|x|)] \quad (13)$$

Using Equation (12a) and its derivative, the following displacement solution is obtained from Equation (13):

$$\Delta(a) = \frac{(\bar{y}_2 - \bar{y}_0)\lambda_0}{\lambda_2 + \lambda_0} \left(e^{-\lambda_2 a} + \lambda_2 a - 1 \right) \quad (14)$$

The limiting value of bending moment at the crack tip, M_0 , is used to estimate \mathcal{G}_I as discussed subsequently. From Equations (8) and (12),

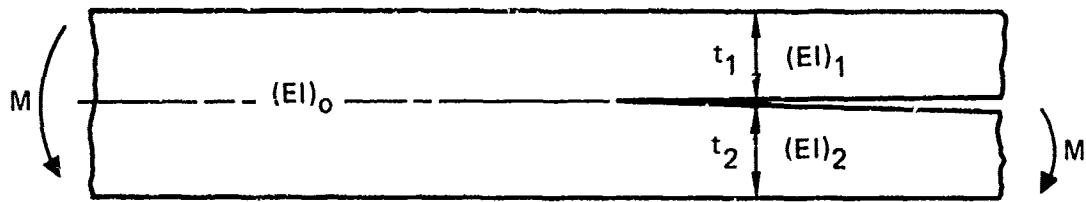
$$M_0 = P \lim_{|x| \rightarrow 0} [y(|x|)] = P \frac{(\bar{y}_2 - \bar{y}_0)\lambda_0}{\lambda_2 + \lambda_0} \quad (15)$$

1.3 Estimation of \mathcal{G}_I

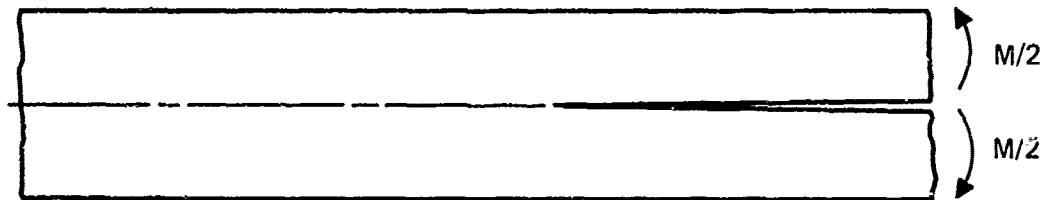
An approximate solution for \mathcal{G}_I in the CLS specimen under tension loading was sought by consideration of the related problem of the CLS specimen subjected to a uniform bending moment M , Figure 9(a). The total strain energy release rate for this loading condition can be computed in a manner parallel to that used to obtain Equation (5) for the tension loading case. This leads to the following result for the pure bending case:

$$\mathcal{G} = \frac{M^2}{2b_N (EI)_2} \left[1 - \frac{(EI)_2}{(EI)_0} \right] \quad (16)$$

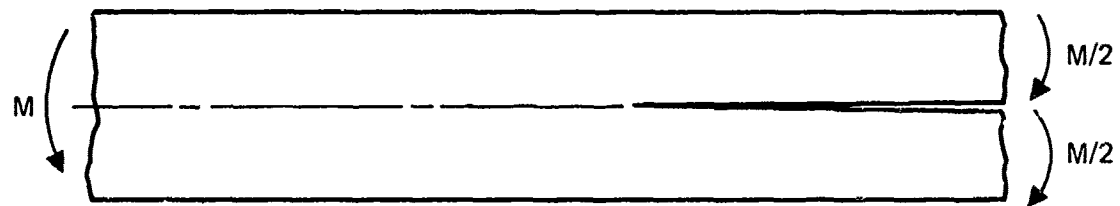
Since the loading and geometry are not symmetric about the crack plane, the CLS specimen in pure bending is not a Pure Mode I case. However, the special case of adherends of the same material and cross section can be decomposed into symmetric and antisymmetric parts (Figure 9(b) and 9(c)), each of which can be solved by the same virtual strain energy procedure. The \mathcal{G}_I and \mathcal{G}_{II} solutions are



(a) THE CRACKED LAP SHEAR SPECIMEN
SUBJECTED TO BENDING



(b) THE SYMMETRIC PROBLEM



(c) THE ANTISYMMETRIC PROBLEM

Figure 9. Symmetric and antisymmetric component problems for the cracked lap shear specimen in bending

$$\psi_I = \frac{M^2}{4b_N(EI)_2} \quad (17)$$

$$\psi_{II} = \frac{3M^2}{16b_N(EI)_2} \quad a,b$$

In other words, the ratio ψ_I/ψ for this special case is 4/7.

In lieu of further exact analysis, two approximations are made in order to estimate ψ_I for a CLS specimen loaded in tension:

- The ψ_I value due to the induced bending moment at the crack tip is assumed to be equivalent to ψ_I due to an equal uniform bending moment, applied as in Figure 9(a).
- For pure bending of a CLS specimen the ψ_I/ψ ratio of 4/7, exact for equal thickness aluminum adherends, is assumed to be a good approximation when the thicknesses are not equal.

Under these assumptions, the ψ_I value for the tension-loaded CLS specimen is approximated as

$$\psi_I = \frac{2M_o^2}{7b_N(EI)_2} \left[1 - \frac{(EI)_2}{(EI)_o} \right] \quad (18)$$

where M_o is given in Equation (15). Thereby, for a given specimen geometry, ψ_I is expressed as proportional to the square of the load:

$$\frac{\psi_I}{\psi_o} = C_{LS} \left(\frac{P}{P_o} \right)^2 \quad (19)$$

where standard normalization factors ψ_o and P_o are defined as

$$\psi_o = 0.1751 \text{ kJ/m}^2 \text{ (1.00 lb/in.)} \quad (20)$$

$$P_o = 4.4482 \text{ kN (1.00 kip)} \quad (21)$$

and the proportionality constant C_{LS} is given by

$$C_{LS} = \frac{2(\bar{y}_2 - \bar{y}_o)^2}{7b_N(EI)_o} \left[\frac{\sqrt{(EI)_o / (EI)_2} - 1}{\sqrt{(EI)_o / (EI)_2} + 1} \right] \quad (22)$$

2 TEST METHODS FOR THE CLS SPECIMEN

The CLS specimen was designed and fabricated; test methods and crack monitoring procedures were developed; and tests were attempted for fatigue loading, increasing loading, and sustained loading in hot water. All the major goals of this specimen development effort were met, as described in the following subsections.

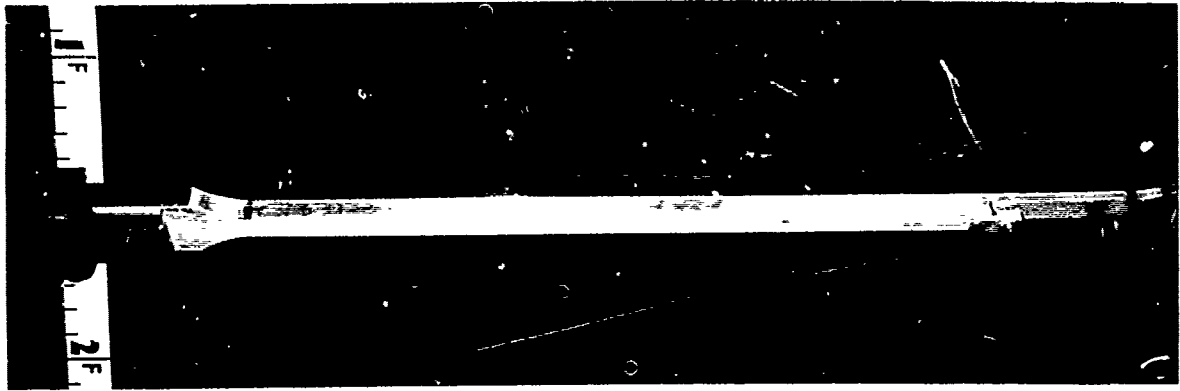
2.1 Fatigue Test Method

The first CLS specimen successfully fatigue tested was CLS-1, which had equal adherend thicknesses of 12.7 mm (0.50 in.). Each adherend was itself laminated from available 7075-T6 aluminum sheet and plate stock, 4.8 mm (0.19 in.) and 7.9 mm (0.31 in.) in thickness. Three views of this specimen are shown in Figure 10.

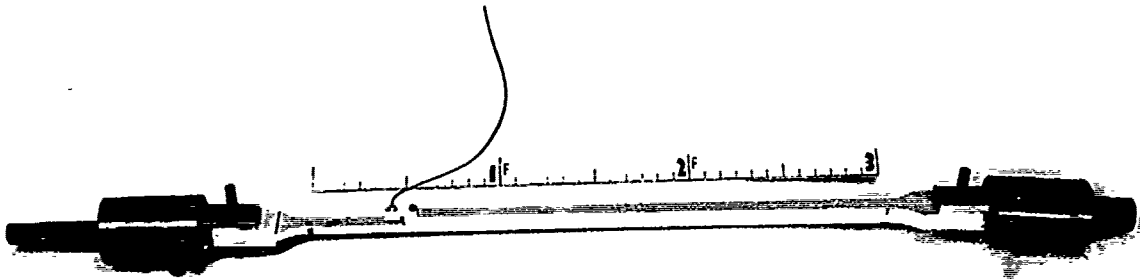
The strain energy release rate solution for Specimen CLS-1 prior to side notching can be obtained from the equations of subsection 1. From Equations (18) and (5), $\mathcal{G}_I/\mathcal{G} = 0.205$. From Equation (22), $C_{LS} = 0.0102$.

The crack-length independence of the CLS specimen is exact only if the length-to-thickness ratio is infinite. The use of the double universal end grips instead of fixed end grips is to maximize the effective length of the specimen. The total length of CLS specimens used in this work was 1.17 m (46 in.), the maximum panel length that can be accommodated by the dip tanks used in the surface preparation prior to bonding.

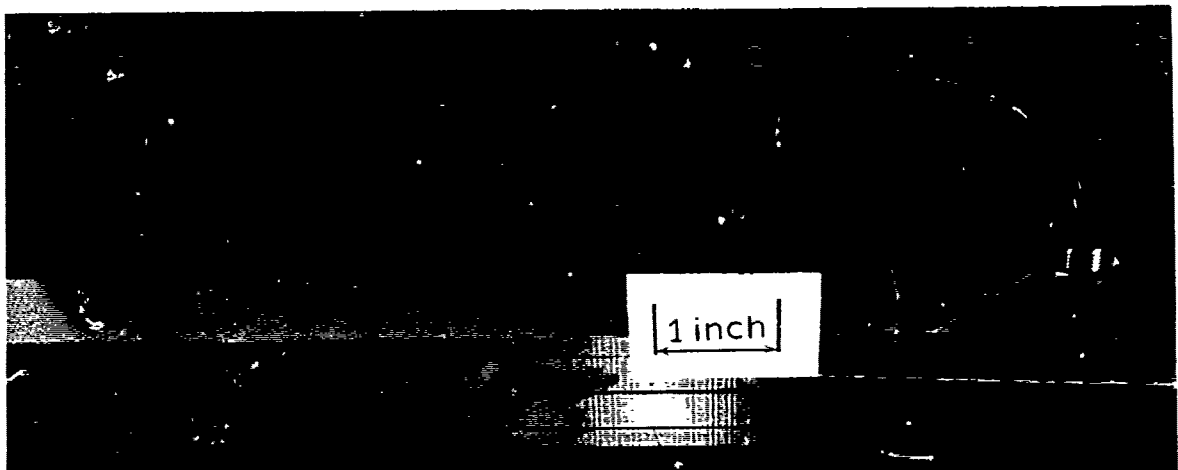
Fatigue loading was applied at 3 Hz to a maximum of 89 kN (20 kips). This cyclic rate was selected on the basis of earlier MRL work which indicated



(a) In Fatigue Test Frame



(b) With Double Universal End Grips



(c) Crack-Tip Area, Extensometer

Figure 10. Three views of specimen CLS-1

major effects of cyclic frequency on da/dN for structural adhesive systems at rates above 3 Hz.

Crack growth was followed using compliance as obtained from an x-y recorder which recorded the applied tensile load vs. the opening displacement obtained from a noncontacting type extensometer located 14.5 mm (0.57 in.) from the lap-shear step. The extensometer was bolted to the shorter of the two strips and read the distance observed from the longer of the strips.

Crack length was also followed visually by marking a series of equally spaced lines perpendicular to and crossing the crack line and observing, at 5x, the shear displacement of the lines. The crack could be found quite easily by locating the position where, during 0.5 Hz fatigue, one marked line appeared to have shear displacement at the bond plane while a succeeding line did not.

A series of observations of crack length, extensometer displacement, and load were made. Equation (14) of Section 1.2 was used to construct a series of theoretical load-displacement curves for CLS-1 for different crack lengths, shown as solid lines in Figure 11. At visually observed crack lengths of 180, 184, and 197 mm (7.08, 7.23 and 7.74 in.), load-displacement records were made and traced onto Figure 11. The shapes of these experimental curves match the theoretical shapes. Note that the theory suggests slightly longer crack lengths than visually observed; approximately 187, 193, and 201 mm (7.35, 7.60 and 7.90 in.). The errors, respectively, are 3.7%, 4.9% and 2.0%.

2.2 Side Notching for Increasing-Load Testing

Prior to fatigue testing an attempt was made to propagate the crack in Specimen CLS-1 by gradual application of a monotonically-increasing load of 89 kN (20 kip), but no crack extension occurred. No higher load could be used because the maximum adherend stress (tension plus induced bending) was very near to the tensile yield stress of the 7075-T6 aluminum adherends. At this load the applied total \mathcal{G} was 3.43 kN/m^2 (19.6 lb/in) and the \mathcal{G}_I component was 0.72 kN/m^2 (4.09 lb/in).

Subsequent to fatigue testing, CLS-1 was side notched as shown in the sketch in Figure 12, and crack extension under an increasing load was obtained. Side notching reduced the width of the adhesive layer by 81.5 percent while

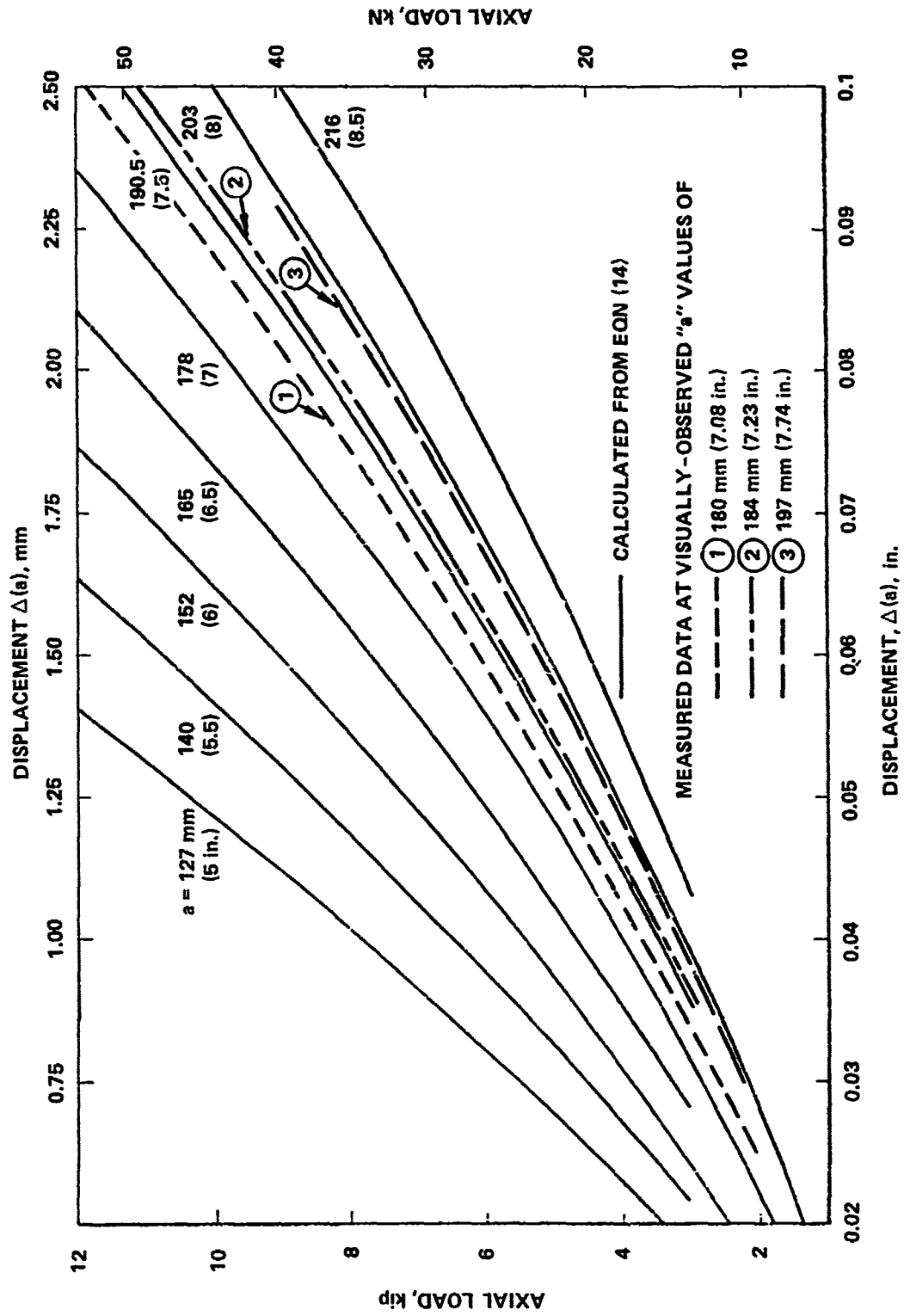


Figure 11. CLS specimen load-displacement curves

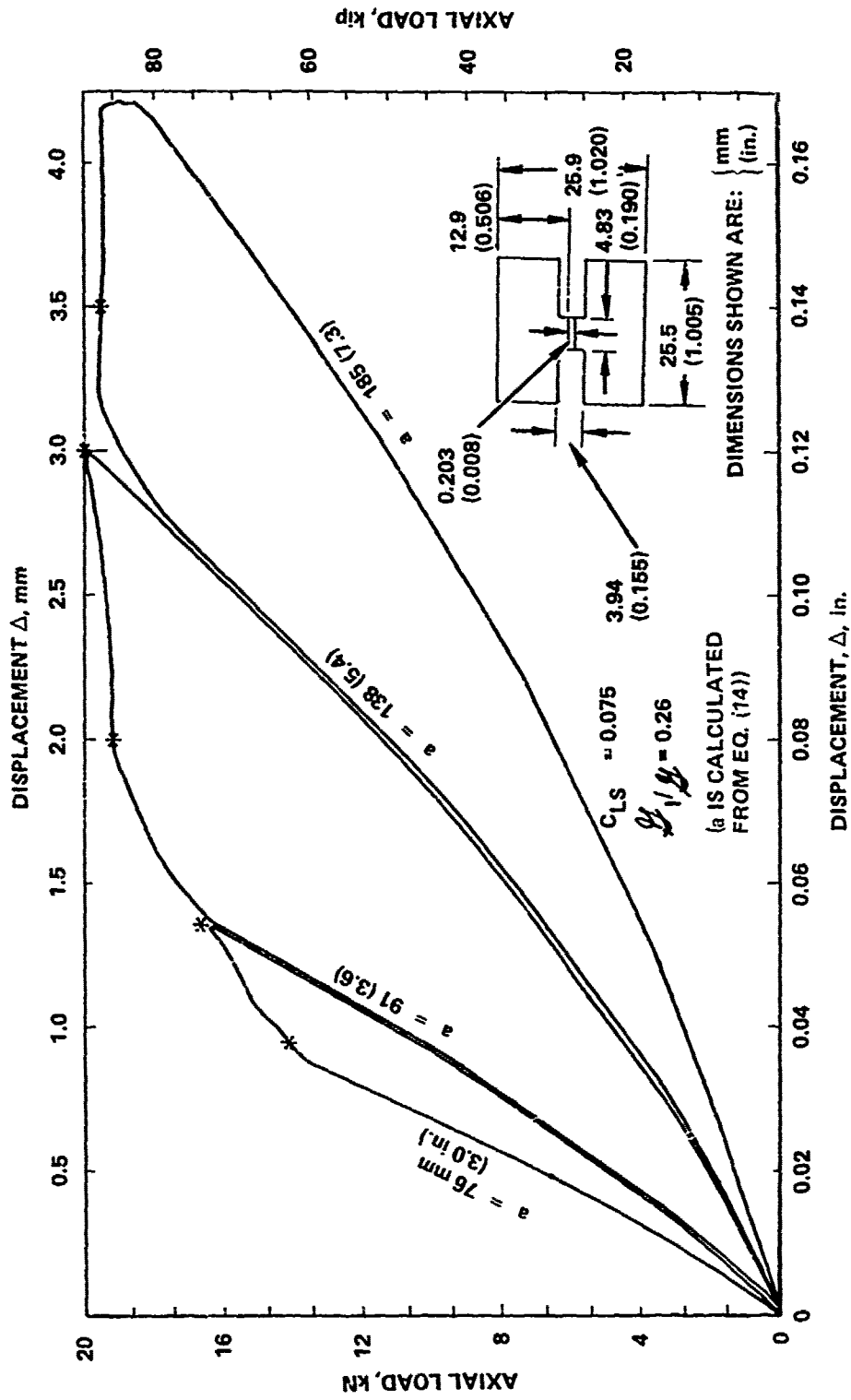


Figure 12. Increasing load test record for side-notched specimen CLS-1

leaving the metal substantially intact. This greatly increased the ratio of adhesive stress to adherend stress, so that crack propagation in the bondline could precede metal yielding. For this configuration, $\mathcal{G}_I/\mathcal{G} = 0.257$; $C_{LS} = 0.0753$.

The load-displacement record (Figure 12), obtained for slow crack extension from the prior fatigue crack, is described as follows. Initially, at a calculated crack length of 76 mm (3.0 in.), the record follows the load-deformation curve described by Equation (14). It began to deviate from the theoretical curve (indicating crack extension) at $P = 60$ kN (13.5 kip) and $\mathcal{G}_I = 2.40$ kJ/m² (13.7 lb/in), but the load continued to rise. At $P = 73.4$ kN (16.5 kip) and $\mathcal{G}_I = 3.59$ kJ/m² (20.5 lb/in) the specimen was unloaded and examined for evidence of large scale shear motion during unloading which was not apparent. Calculated crack length was 91 mm (3.6 in.).

The specimen was reloaded and cracking began again at $P = 73.4$ kN (16.5 kip) and $\mathcal{G}_I = 3.59$ kJ/m² (20.5 lb/in). The load continued to rise during crack extension until a plateau was reached at $P = 85.4$ kN (19.2 kip) and $\mathcal{G}_I = 4.86$ kJ/m² (27.75 lb/in). The load remained almost constant for 25 mm (1 in.) of growth, rising gradually to $P = 89$ kN (20 kip) and $\mathcal{G}_I = 5.27$ kJ/m² (20.1 lb/in). The unloading curve followed the theoretical curve for a crack length of $a = 138$ mm (5.4 in.). Upon reloading to $P = 80$ kN (18 kip) and $\mathcal{G}_I = 4.27$ kJ/m² (24.4 lb/in) crack growth began again, and the load became constant at $P = 86.7$ kN (19.5 kip) and $\mathcal{G}_I = 5.01$ kJ/m² (28.6 lb/in) until unloading at $a = 185$ mm (7.3 in.).

Further increasing-load testing was done on Specimen CLS-3, which had adherend thicknesses t_1 and t_2 , respectively, of 19.4 and 9.7 mm (0.762 and 0.380 in.). After fatigue data were obtained, CLS-3 was side notched to the configuration sketched in Figure 13, with all of the metal removed from the thicker adherend. For side-notched Specimen CLS-3, $\mathcal{G}_I/\mathcal{G} = 0.241$; $C_{LS} = 0.157$.

After side notching but before the increasing-load testing, additional fatigue data were obtained at $R = 0.1$ to verify that side notching does not affect da/dN at a specified $\Delta\mathcal{G}_I$ value. These fatigue data are shown in Figure 28 and 29 of Section III as data points containing an X. The three data points obtained are roughly within the scatterband of the other CLS specimens.

Specimen CLS-3 was then increasing-load tested to complete fracture. The total load, P , versus the Mode I displacement, Δ_I , is shown in Figure 13. The test was begun at a compliance-measured crack length of 68 mm (2.7 in.). The first indication of gross crack extension occurred where the curve began to bend over at $P = 43.1$ kN (9.7 kip) and $\mathcal{G}_I = 2.59$ kJ/m² (14.8 lb/in). However, the load continued to rise to a maximum value of $P = 46.7$ kN (10.5 kip) and $\mathcal{G}_I = 3.04$ kJ/m² (17.3 lb/in). The crack extended at approximately constant load for about 25 mm (1 in.), then dropped to a plateau value of $P = 44.5$ kN (10.5 kip) and $\mathcal{G}_I = 2.76$ kJ/m² (15.7 lb/in) with additional crack extension. The specimen was then unloaded and reloaded. While some deviation of the P - Δ curve occurred at low loads, the curve shapes at higher loads corresponded closely to the theoretical curves for $a = 138$ mm (5.42 in) for unloading and 148 mm (5.84 in) for loading. The load reached a peak value of $P = 43.6$ kN (9.8 kip) and $\mathcal{G}_I = 2.65$ kJ/m² (15.1 lb/in). Further extension occurred at a nearly constant load of $P = 41.8$ kN (9.4 kip) and $\mathcal{G}_I = 2.43$ kJ/m² (13.9 lb/in). The specimen was then unloaded at a crack length of 288 mm (11.3 in.) and cut to expose the fracture surface.

For the 68 mm (2.7 in.) crack the experimental load-displacement curve was not the same shape as the theoretical curve. This crack length was estimated from the curve using an average slope. For the longer cracks the upper end of the load displacement curve matched theoretical shapes perfectly for the crack size selected, except near the load peak where crack extension probably occurred. However, the unloading curve for $a = 138$ mm (5.4 inch) and the loading curve for $a = 148$ mm (5.8 in.) deviated from the theoretical shape near zero load.

What is remarkable about this test result is the constancy of \mathcal{G}_c over 220 mm (8.6 in.) of crack length.

The equilibrium value of \mathcal{G}_c (or \mathcal{G}_{Ic}) for CLS-3 does not match that obtained on CLS-1. The average value of \mathcal{G}_{Ic} for CLS-1 was about 5.0 kJ/m² (28.5 lb/in) compared to about 2.7 kJ/m² (15.4 lb/in) for CLS-3.

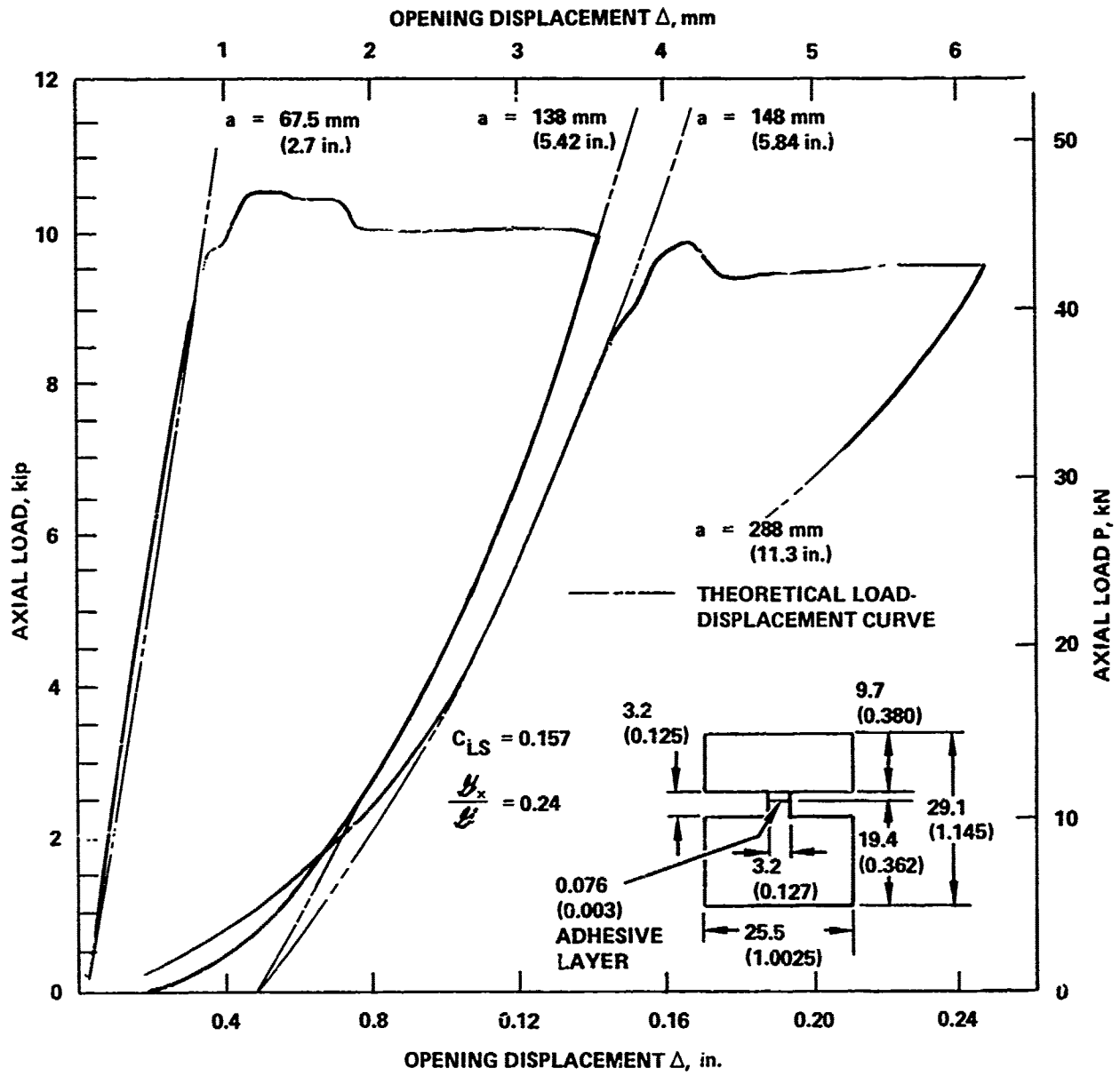


Figure 13. Load-displacement record for specimen CLS-3

2.3 Special Test Methods for Environmental Tests

Fixturing and apparatus were prepared for elevated temperature exposure in water for both fatigue and stress corrosion cracking (SCC) testing. The fatigue test fixturing consisted essentially of modification to the CLS loading train to permit constant temperature water to circulate around the specimen. The normal loading train, assembled as shown in Figure 10(a), consisted of a double universal at both ends of the specimen, the outer universal couplings ending in a threaded rod for connection to the test machine. For fatigue testing the test machine was a closed-loop servo-hydraulic type; however, for SCC testing an enlarged opening creep-rupture test machine was used. This enlarged opening machine was needed because the total length of the specimen with the universals was more than 1.5 m (5 ft). The need for the water bath apparatus required that the upper part of the lower universal be modified to accept and retain a water bath tube. This grip was remanufactured from 304 stainless steel, and "O" rings were used to seal a 76 mm (3 in.) inside diameter PMMA tube around the specimen. Ports for water entry were provided in the grip as well. The grip modification was the same for both the fatigue and SCC testing. Thus one was made for each test set up. The specimen water bath was provided from a heated constant temperature water reservoir designed to provide heated deionized water for a number of elevated temperature tests. Evaporative and other losses were made up by an automatic filling deionized water supply. Temperature was maintained in the water surrounding the specimen by the use of a thermostatically controlled hot water inlet valve. Temperature regulation using this system was about $\pm 2^{\circ}\text{K}$ (3.8°F) at worst. Since the containment tube was more than 0.9 m (3 ft) long, the water inlet was located in the bottom grip to minimize temperature variations due to convection. The specimen itself was fitted to the grips with a stainless pin coated with a thin layer of plastic to avoid electrical contact between the specimen and the grips. To avoid general corrosion in this environment the specimen was taped using polytetrafluoroethylene (PTFE) tape in all areas except that of the bond line.

Monitoring of crack growth is done using compliance measurements for both fatigue and SCC tests. For fatigue testing the use of the gage shown in

Figure 10(c) described earlier is well understood and its accuracy correlated with visual observations of the crack length. Compliance monitoring for sustained load tests is somewhat more difficult because of a gradual shift in the displacement corresponding to zero load. This effect was noted after a long exposure test indicated a greater crack growth than could be visually observed. To verify the actual compliance the specimen was unloaded and re-loaded periodically. The slope of the load-displacement curve gave a measurement of the true crack length, whereas the absolute displacement has been misleading.

3 DEVELOPMENT WORK ON OTHER SPECIMENS

A substantial amount of testing and analysis work was done on the width-tapered beam (WTB) specimen, diagonal loading of the contoured double-cantilever beam (CDCB) specimen, the beam and column (BC) specimen, and modified zero K-gradient (MZKG) specimen. This work is summarized in the following sections.

3.1 The Width-Tapered Beam (WTB) Specimen

The constant \mathcal{G}_I specimen known as the width-tapered beam (WTB) (Figure 3) was first described in Reference 7, where the applied crack extension force \mathcal{G}_I is given for a short-height pair of beams as

$$\mathcal{G}_I = \frac{P^2}{2} \frac{8}{b_N} \frac{1}{Eb} \left(\frac{3a^2}{h^3} \right) \quad (23)$$

where

P = applied load

E = elastic modulus of the adherends

b = specimen width at the crack tip

b_N = width of the adhesive layer at the crack tip

h = height of one adherend

a = crack length as measured from the loading holes

For the case where b_N equals b, this expression can be written in terms of the a/b ratio:

$$\mathcal{G}_I = \frac{12P^2}{Eh^3} \left(\frac{a}{b}\right)^2 \quad (24)$$

The maximum bending stress in the adherends can be determined from the following:

$$s = \frac{6P}{h^2} \left(\frac{a}{b}\right) \quad (25)$$

Crack length can be estimated from the following. The compliance of an ideal WTB specimen where the taper begins at the load point is given by:

$$c = \frac{12a^2}{Eh^3} \left(\frac{a}{b}\right) \quad (26)$$

In an actual specimen where there is a straight section before the start of the taper, the expression can be rewritten with a constant reduction in the compliance

$$c = \frac{12a^2}{Eh^3} \left(\frac{a}{b}\right) - c_0 \quad (27)$$

While Equations (24) and (27) are adequate to within perhaps 20 percent when used to estimate \mathcal{G}_I and crack length an accurate compliance-crack length curve must be established to define these variables for \mathcal{G}_{Ic} and fatigue testing. It should be recalled that the beam formula used for constant height beams required a rotation and shear correction to define crack length and dc/da as a function of crack length. An example of these corrections of Equation (27) might be

$$c = -c_0 + \left[\frac{12}{Eh^3} (a + a_0)^2 \left(\frac{a}{b}\right) \right] + \left[\frac{8}{Eh} \left(\frac{a}{b}\right) \ln \left(\frac{a}{b}\right) \right] \quad (28)$$

where the first bracketed term contains the rotation correction as an offset, a_o , in the actual crack length and the second bracketed term involves the natural log of the a/b ratio as the shear correction.

Specimen WTB-1, shown in Figure 14, was machined from a bonded plate with 9.5 mm (0.375 in.) adherends of 7075-T6 Aluminum and AF-55S adhesive, precracked by prying the end open, and \mathcal{G}_{Ic} tested. The a/b ratio for the specimen is set equal to 3. The load-displacement record is shown in Figure 15.

The starter crack was located 38 mm (1.5 in.) from the loading holes in a straight section of the beam where b is 28.2 mm (1.11 in.). When first applied, the load reached a maximum of 1.98 kN (446 lb). Using Equation (25), the maximum stress level in the beams was 175 MPa (25.4 ksi).

Once the crack entered the tapered section of the specimen, the load dropped to a nearly constant value of 1.47 kN (330 lb), and each adherend became a constant stress beam. Using Equation (25), the stresses in the beam were 288 MPa (41.7 ksi). While these stresses are high, they are still far less than the yield strength, 517 MPa (75 ksi), for 7075-T6 aluminum. This is verified by examination of the specimen after testing which showed no permanent deformation had occurred in the adherends. This load corresponds to $\mathcal{G}_{Ic} = 3.78 \text{ kJ/m}^2$ (21.6 lb/in). The specimen was then unloaded and reloaded, whereupon the load returned to the same constant value as crack growth continued.

The \mathcal{G}_{Ic} value obtained in this test is 1.2 to $\hat{4}$ times higher than the range of values obtained previously in the CDCB specimens. There are at least two possible explanations for the high value. The first is that there is not yet an accurate compliance calibration for the WTB. The second is that standard industry practice for producing large-area bonded panels results in significantly higher values of \mathcal{G}_{Ic} .

While it is gratifying to obtain data suggesting that commercial practice results in higher toughness values than for the narrow-area laboratory bonds, it should be recalled that there has been little, if any, relationship observed between \mathcal{G}_{Ic} and the Mode-I fatigue properties of a given adhesive bond. Therefore, it is expected that the fatigue characteristics measured on the WTB specimen will be similar to those measured on the CDCB specimen.

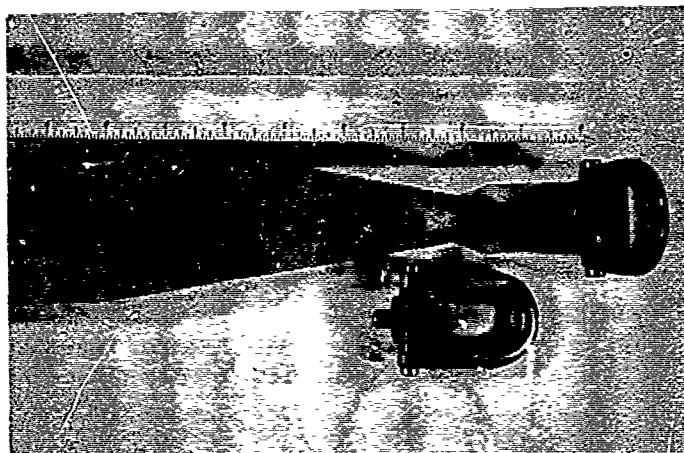


Figure 14. Width-tapered beam (WTB) specimen shown with gripping bolts

3.2 Diagonal Loading of the CDCB Specimen

The fixturing for diagonally loading the CDCB specimen is shown in Figure 4. Preliminary tests with this specimen-grip arrangement indicated an apparent decrease of as much as a 30 percent in critical strain energy release rate with the addition of no more than a 5 percent Mode II component. Reexamination of the test fixture indicated that it had been made for specimens having a grip hole separation of 12.7 mm (0.50 in.). Specimens tested in this fixture had an actual separation of 13.7 mm (0.54 in.), placing an additional Mode I moment on the specimen. New holes were then cut into the angled grips and new specimens tested.

During the 60-degree angle test, a 60-degree triangle was placed on the grips and lines were scribed on the specimen during loading that should have remained parallel to the bond line. While these lines did start out parallel to the bond line to within 1-degree, as loading progressed the loading angle continuously dropped. In some cases, the loading angle dropped to 56 degrees from the initial 60 degrees at the crack extension load. Calculation of \mathcal{G}_c for AF 55S material with the remade grips was done using the actual angle at the crack extension load. Values of \mathcal{G}_c in this test series were equal to or greater than the value of \mathcal{G}_{Ic} determined on this material.

Thus the idea of diagonally loading the CDCB specimen to achieve a mixed-mode condition has two disadvantages. One, known from the start, is that only a very small percentage of Mode II is readily achieved by this means. The

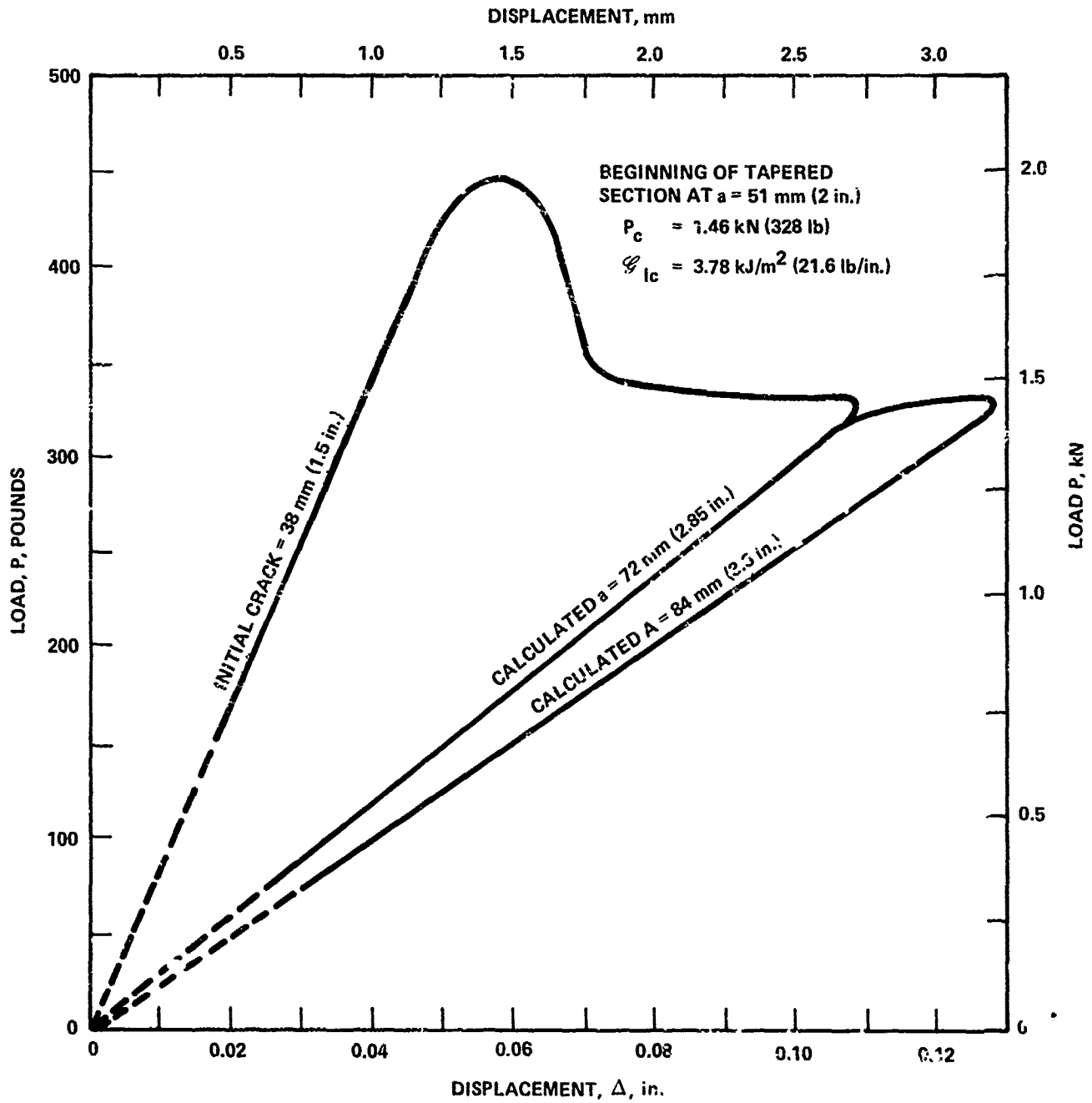


Figure 15. Load-displacement record for width-tapered beam specimen (WTB-1)

second, discovered here, is that small variations in the geometry or alignment of the specimen cause large changes in the computed strain energy release rates. When possible, such geometrically ill-conditioned specimens are to be avoided, so no further use was made of this loading configuration.

3.3 Beam-and-Column (BC) Specimen

A conceptual view of the original Beam-and-Column (BC) specimen is shown in Figure 5. In theory the specimen can be tested in any combination of Modes I, II, and III. The vertical forces P , aligned with the bondline, induce pure \mathcal{G}_{II} , while the concentrated moments M , applied independently of P , induce a selected combination of Modes I and III. \mathcal{G}_I , \mathcal{G}_{II} and \mathcal{G}_{III} are all crack length independent.

Redesign resulted in the specimen shown leaning against the test machine in Figure 16. This bending moment, applied by loading bars connected at the two pair of holes on either side of the bondline, apply pure Mode I, and $\mathcal{G}_{III} = 0$. Radii were provided on the surfaces of contact for the Mode II load P so that P , applied across rollers, would remain aligned with the bondline, despite any rotations resulting from the Mode I load. The direction of P could be reversed for fatigue cycling at negative R ratios in Mode II.

The specimens were tested in a unique test frame that permitted two-axis loading using a single actuator. Figure 16 shows the test frame installed in a 3,000-pound capacity, closed-loop type hydraulic test machine. (Note that one BC specimen is hidden in the loading members of the test frame in addition to the one shown resting against a post of the closed-loop machine.) A closeup of the test frame alone is shown in Figure 17.

The fixture applies two-axis loading as follows: Pure shear loads are applied by the pair of pin grip holders held in forced alignment by two sets of four flex plates affixed to each grip. The shear grips cannot be moved out of alignment by the Mode I component because of these flex plates. Note that each grip has two pins so that shear can be applied in both directions. The specimen itself has four contoured bearing surfaces. Radii on all four were calculated assuming the crack tip to be 102 mm (4 in.) from the start of the uniform DCB section. Thus, when the specimen responds to the Mode I load the contoured sections of the two specimen halves should rotate in opposite directions but the shear load should remain on the crack line.

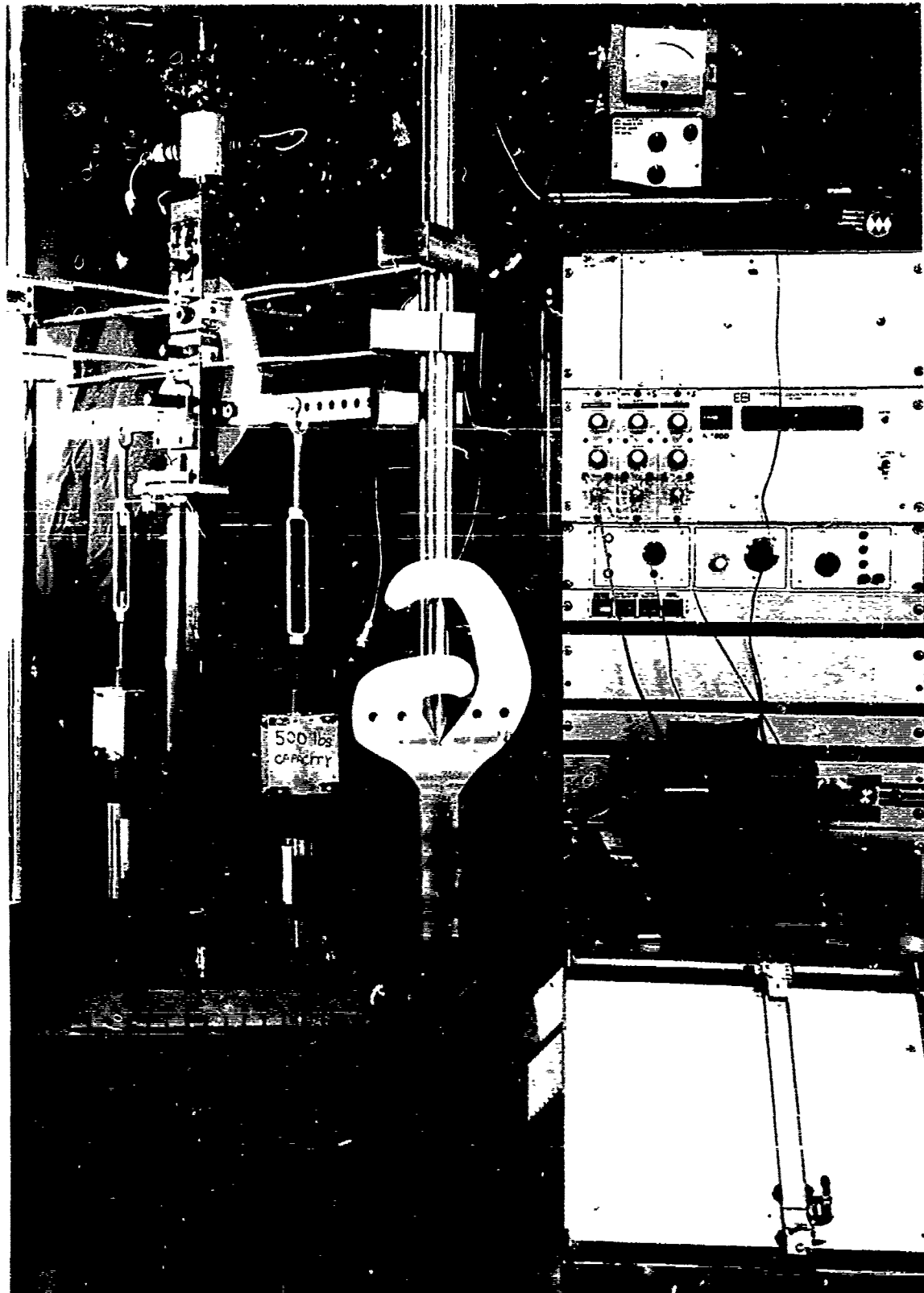


Figure 16. Single actuator test assembly for two-axis loading of BC specimens (Note that one specimen is shown in the test fixture and a second is shown resting against the post of the test frame.)

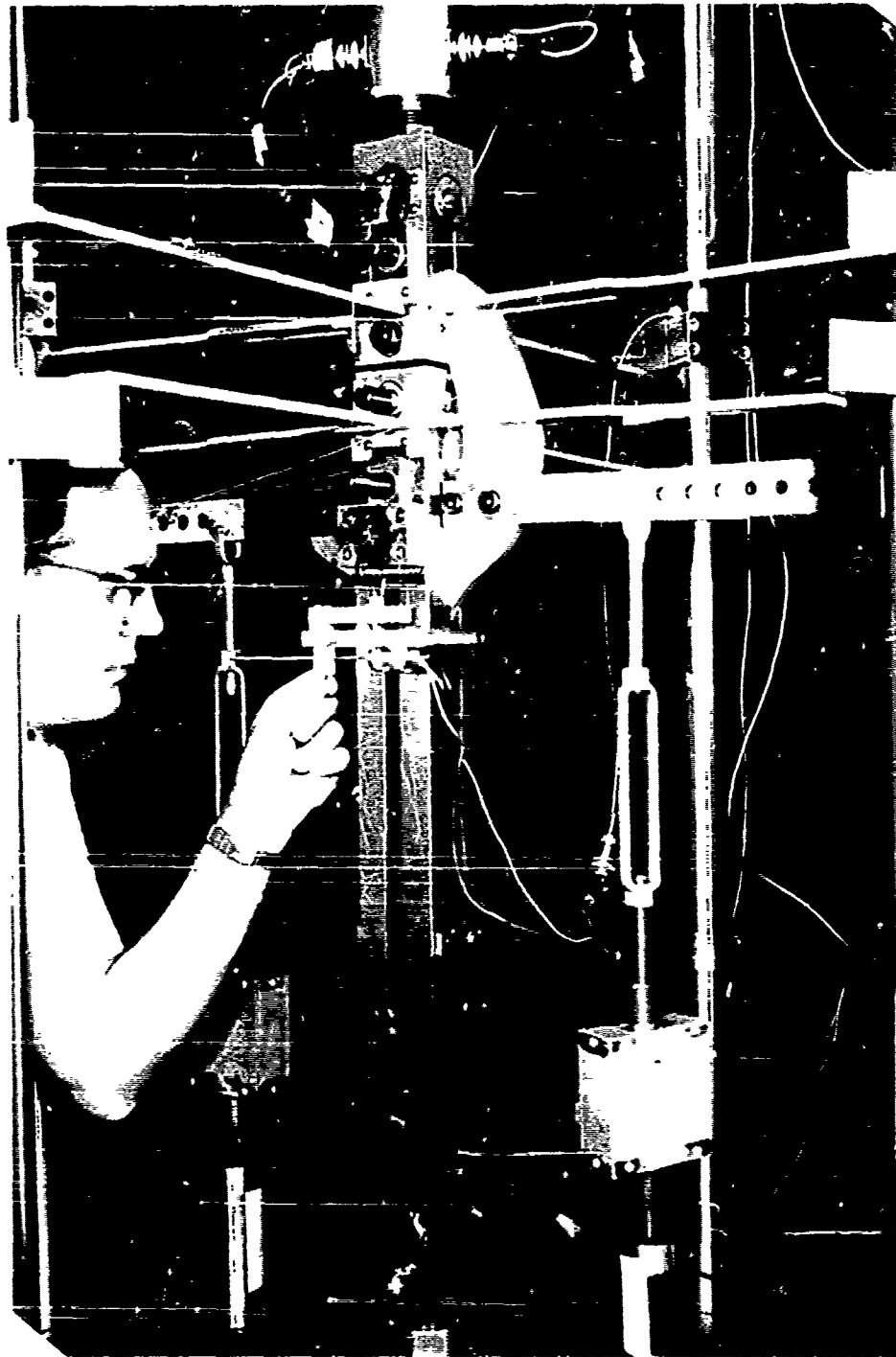


Figure 17. Close-up view of Mode I - Mode II test frame.
[Note: (1) Mode I moment applied through arms
load cells and springs; (2) Mode II load applied
through pinned grips with flex plates; (3) Deflec-
tion in both axes measured with bolt-on extenso-
meters being adjusted by technician.]

The total load on the specimen was measured with the load cell shown above the top shear grip. The extended, hollowed part of the lower shear grip, which provided clearance for the specimen, was connected through the Mode II spring assembly and the Mode I loading bar to the actuator. The Mode II spring assembly contained two springs, above and below an internally flanged loading rod, which reacted to either tension or compression. These springs were selected such that a sufficient motion would be available for the Mode I loading bar to produce the desired amount of \mathcal{G}_I on the test specimen.

The Mode I component of the load was applied through the two moment bars attached by two pins in each specimen half. These bars were attached to the Mode I loading bar through a turnbuckle, a Mode I spring assembly and load cell on each side.

The initial set-up of a BC specimen in this fixture is done by selecting a particular set of Mode I moment bar holes and applying a slight Mode I pre-load to each side of the specimen using the turnbuckles. The major load is applied using the hydraulic ram which increased \mathcal{G}_I and \mathcal{G}_{II} proportionately. Loading was increased until crack growth was observed either visually or with the instrumentation used for measuring displacements or strains.

Initially the instrumentation consisted of separate displacement gages as shown in Figure 17, one for measuring the opening (Mode I) displacement and one the sliding (Mode II) displacement. However, this instrumentation was deemed inadequate when it was determined that the Mode II loading could induce Mode I strains near the crack tip that would not be measurable on the Mode I displacement gage. New instrumentation consisted of strain gages that independently measured the adherend bending strain (Mode I) and shear strain (Mode II).

Calculation of \mathcal{G}_I and \mathcal{G}_{II} is done using the following equations

$$\mathcal{G}_I = \frac{M}{b_N EI} \tag{29}$$

$$\mathcal{G}_{II} = \frac{P_{II}^2}{b_N EA}$$

a, b

where

$$M = P_I \ell$$

ℓ = Moment arm selected for the particular test. For this fixture ℓ can be 216 to 343 mm (8.5 to 13.5 in.).

b_N = Bondline width, 25.4 mm (1 inch) intervals.

EI = Bending stiffness

EA = Tensile stiffness

Since the method of loading results in a crack length independence of both \mathcal{G}_I and \mathcal{G}_{II} , crack length need not be measured visually but instead can be estimated from the load-displacement record.

Pure Mode I and mixed Modes I and II tests were conducted for a gradually increasing load using three Beam-Column (BC) specimens. On the average, the ratio $\mathcal{G}_{II}/\mathcal{G}_I$ in the mixed mode tests was 0.26. Whereas the average \mathcal{G}_{Ic} value for the three specimens in Pure Mode I tests was 2.52 kJ/m^2 (14.4 lb/in), the average mixed-mode \mathcal{G}_{Ic} value was only 1.60 kJ/m^2 (9.15 lb/in).

The apparent drop in \mathcal{G}_{Ic} for small $\mathcal{G}_{II}/\mathcal{G}_I$ ratios as measured on the BC specimen is not consistent with the increasing-load test results for the combined-mode CLS specimens, where a much higher \mathcal{G}_{II} percentage resulted in larger \mathcal{G}_{Ic} values than 1.60 kJ/m^2 (9.15 lb/in), as discussed in subsection 2.2

It is clear from the test setup discussion that the BC specimen is difficult to test. Furthermore, the ratio of the applied Mode II load (P_{II}) to the Mode I load (P_I) producing the bending moment is typically about 20, so that a small angular misalignment can cause an inadvertent increase in \mathcal{G}_I due to the load P. Finally, further testing of the specimen indicated that it was prone to scatter. Because of the scatter and the ill-conditioned nature of the specimen, the test results were regarded with skepticism and further testing was discontinued.

3.4 The Mode III Test Specimens

One of the objectives of this program was to design a specimen to measure critical strain energy release rate \mathcal{G}_{IIIc} for Mode III and to obtain other slow crack growth or fracture data when loading in primarily Mode III. A uniform beam-type specimen was tested first to ensure that crack growth can be achieved. Then contoured specimens with constant $\partial C/\partial a$ and \mathcal{G}_{III} independent of crack length were fabricated in the configuration shown in Figure 18.

The first order analysis for \mathcal{G}_{III} for a contoured double cantilever beam specimen is obtained from Equation (3) as follows:

$$\begin{aligned} \mathcal{G}_{III} &= \frac{P_{III}^2}{2 b_N} \frac{\partial C}{\partial a} \\ &= \frac{P_{III}^2}{3 E B b_N} \left[\frac{3a^2 + h^2}{I_x/B} \right] \end{aligned} \quad (30)$$

This expression does not contain the $0.6 h$ rotation correction term which is used for noncontoured specimens. It has been found from compliance studies that this correction should not be used for contoured specimens. Using the definitions in Figure 19 the part of Equation (30) in brackets is given by

$$M_o = \left[\frac{3 a^2 + h^2}{\frac{h_1^3}{3} - \frac{\ell^3}{6} - (h_0 + \frac{\ell}{2}) h_1 - \frac{h_1^2 + h_0^2}{2(h_1 + h_0)}} \right] \quad (31)$$

and the expression for \mathcal{G}_{III} can be written as

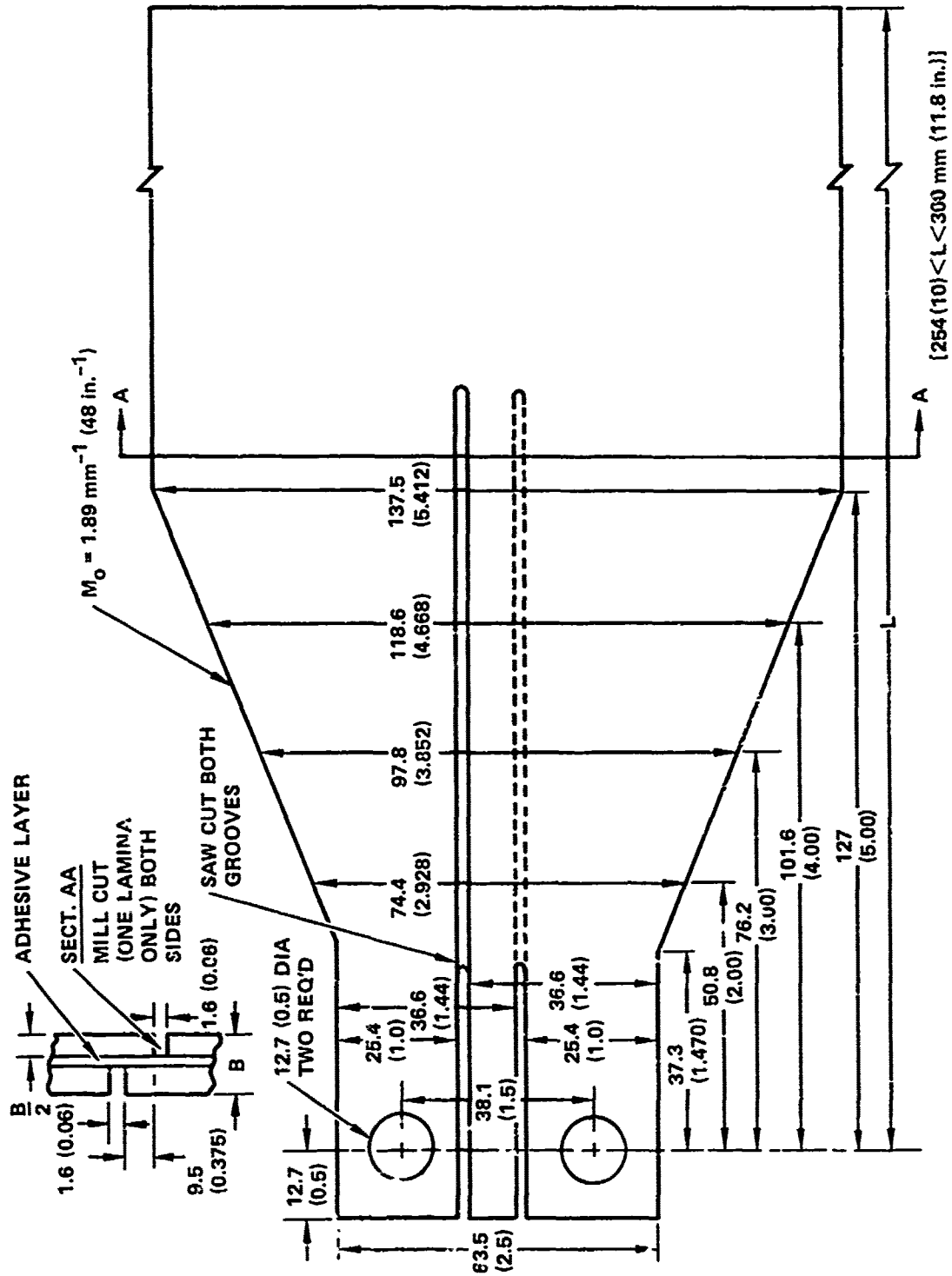


Figure 18. MZKG specimen with $M_0 = 1.89 \text{ min}^{-1} (48 \text{ inch}^{-1})$ for Mode III testing

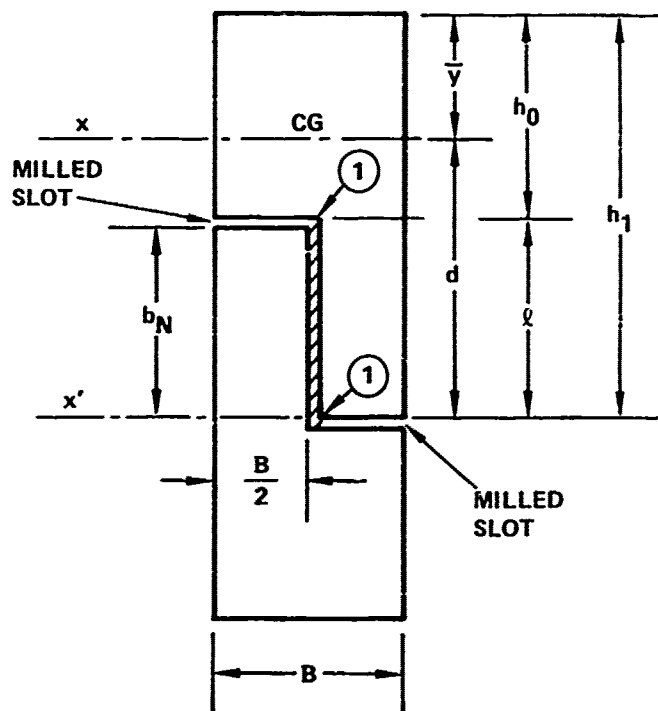


Figure 19. Cross section of the MZKG specimen

$$\mathcal{G}_{III} = \frac{P_{III}^2}{2 b_N} \frac{2}{3EB} [M_o] \quad (32)$$

This expression is independent of the crack length, a , and can be used throughout the contoured region. It should be noted that Equation (32) may not be exact because of the non-rectangular cross-section and the limitations of beam theory, and would best be verified by a compliance calibration.

Since many of the specimens were fairly thin, the grips were designed to restrict the lateral displacement at the pinned ends. The minimum height is 63.5 mm (2.5 inches) which places a reasonable limit on its susceptibility to buckling.

After preliminary \mathcal{G}_{IIIc} testing on specimens which were made from laminated 3.2 mm (0.125 in.) sheet with FM 317 adhesive, test data were obtained from nominally 12.7 mm (0.50 inch) thick specimens laminated from 6.3 mm (0.25 in.) plate using the AF-55S material.

The objective here was to obtain fracture data when loading primarily in Mode III. The simple strength of materials analysis, while adequate to design a constant compliance-change specimen, does not ensure that fracturing will occur by pure Mode III alone. For example, it is expected that there will be a substantial Mode I contribution at point (1) in Figure 19. In addition, some Mode II could be present if the crack front is not parallel to the direction of the applied load P_{III} .

To partially define the effects of extraneous Modes I and II on the value of \mathcal{G}_{IIIc} measured with this specimen configuration, the specimen geometry was varied with a view toward changing the degree of influence of the other modes.

The calculated \mathcal{G}_{IIIc} values for several values of b_N , the overlap length, are shown in Figure 20. These data indicate that at values of b_N less than 15.9 mm (0.625 in.) the value of \mathcal{G}_{III} is subject to some variation which does not appear at b_N of 15.9 and 19.1 mm (5/8 and 3/4 in.). This is not to imply that the value of 11.6 kJ/m² (66 lb/in) is a true value of \mathcal{G}_{IIIc} ; however, it appears that the contribution of Modes I and II to the measured value of \mathcal{G}_{IIIc} is constant at values of b_N of 15.9 mm (0.63 in.) or greater.

Testing of these specimens showed that there is substantial influence of the crack at regions well ahead of the apparent \mathcal{G}_{III} crack front. This had been seen in the preliminary tests by the fact that the back end on a fully slotted specimen underwent deformation and rotation hinging when the apparent crack front was still well within the constant $\partial C/\partial a$ section. These new specimens were made so that the milled slots defining b_N did not extend to the back end.

Fracture surface photographs of the specimens with $b_N = 19, 16, \text{ and } 13 \text{ mm}$ (0.75, 0.63 and 0.5 in.) are shown in Figure 21. These photographs show that slow crack growth in the tapered section occurs with a substantial interface (IF) failure area near each edge (or slot) and a mostly center-of-bond (CoB) failure area in the middle of the overlap. This fracture appearance is essentially independent of overlap size and the percentage of IF and CoB is roughly the same for all three specimens. The fracture surface in the region of

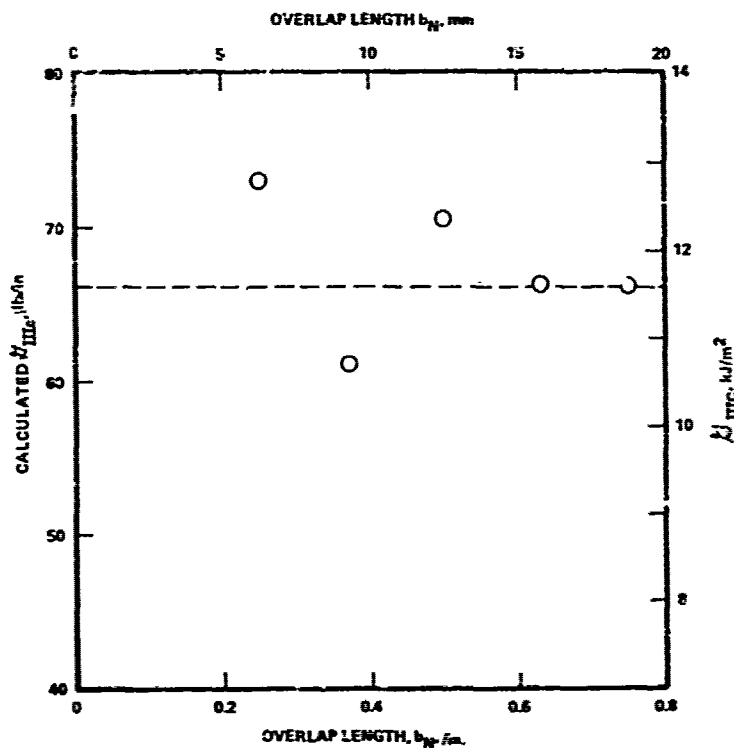
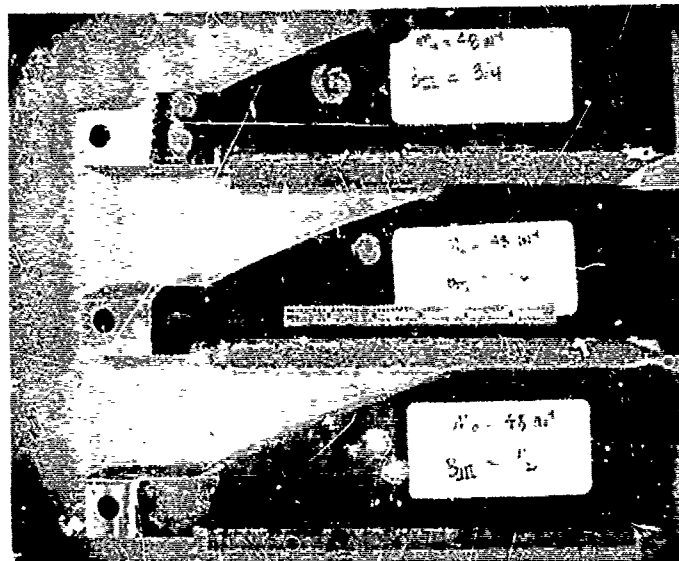


Figure 20. Effect of overlap length on K_{IIIc}

unstable crack growth from the end of the tapered section to near the end of the specimen does not show any IF areas.

Mode III MZKG specimens with b_N of 9.5 and 15.9 mm (0.375 and 0.625 in.) were fatigue tested in laboratory air. The curves of crack growth rate per cycle, da/dN , vs. applied ΔK_{III} are shown in Figure 22. These curves have the same slope, but the curve for the $b_N = 15.9$ mm (0.625 in.) specimens is shifted to the left, towards higher values of da/dN at a given applied ΔK_{III} . Both specimens were machined from the same bonded panel. Thus the overlap b_N of the Mode III specimens, which had no effect in the increasing load tests of Figure 20, appears to have had a substantial effect on the fatigue crack growth rate.

Further efforts to understand Mode III crack growth in the MZKG specimen were not particularly fruitful. Additional study is recommended.



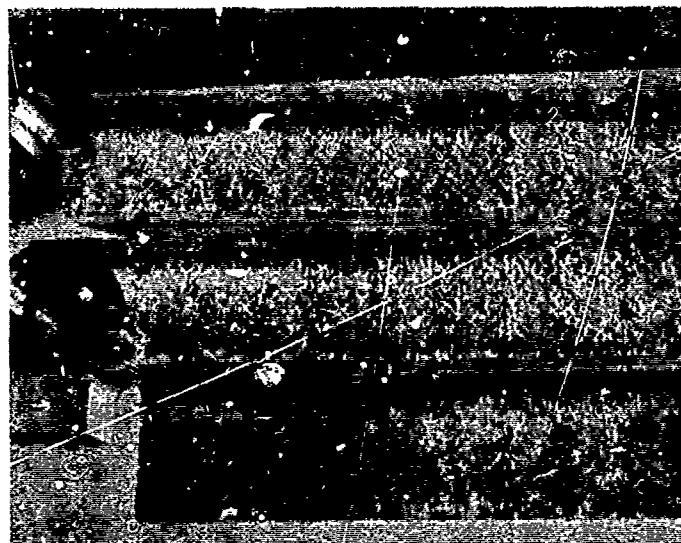
b_N

19 mm
(0.75 in.)

16 mm
(0.63 in.)

13 mm
(0.50 in.)

(a) Complete Specimens



b_N

13 mm
(0.50 in.)

16 mm
(0.63 in.)

19 mm
(0.75 in.)

(b) Enlarged View of Fracture Surfaces

Figure 21. Fracture surface photographs of MZKG specimens

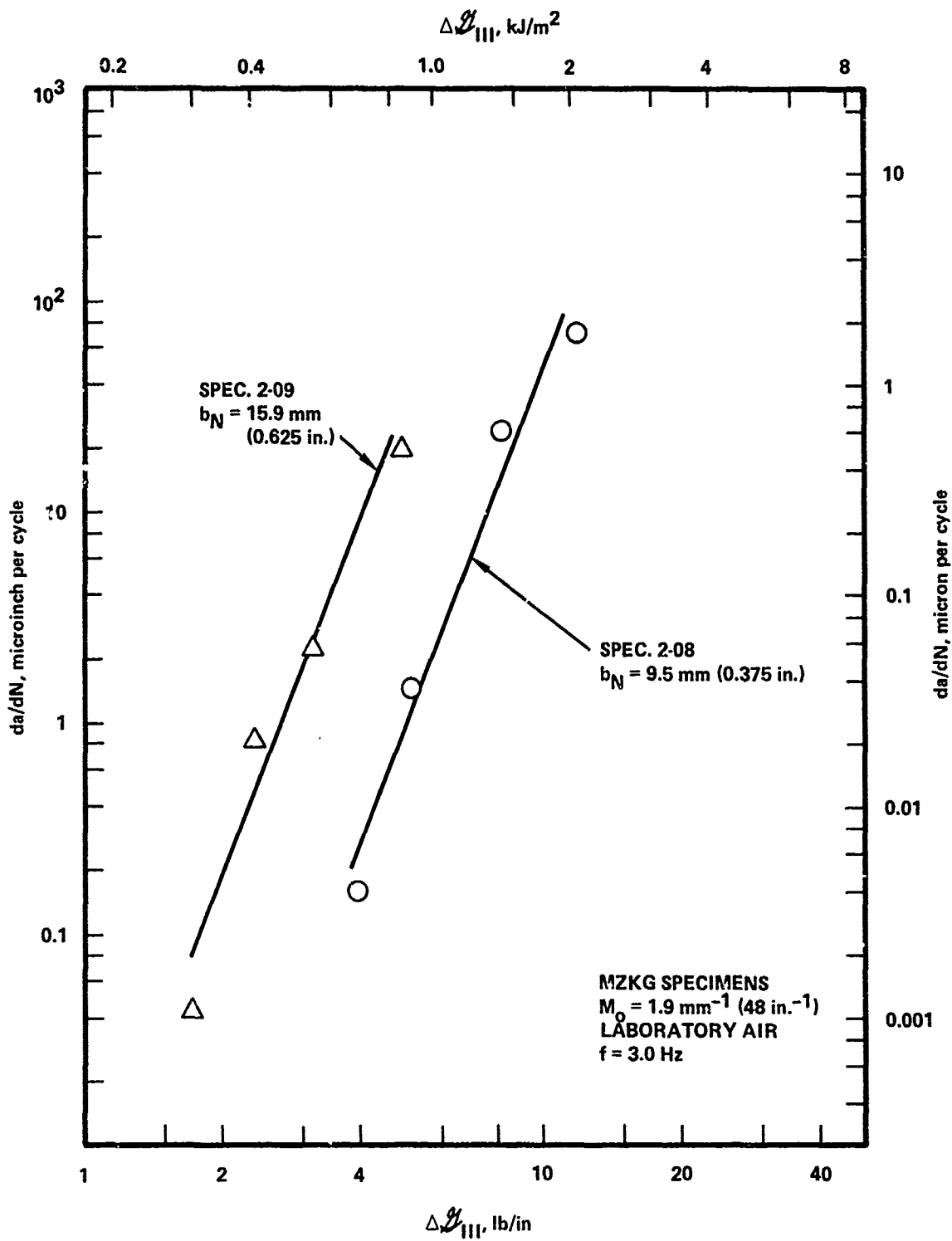


Figure 22. Comparison of Mode III fatigue crack growth curves for two overlap dimensions

SECTION III
BASELINE TESTING

1. INCREASING LOAD TESTS

1.1 Mode I (G_{Ic}) Tests

Table 1 summarizes G_{Ic} values for 12 Contoured Double Cantilever Beam (CDCB) specimens that were increasing-load tested. All 12 specimens were bonded simultaneously, four with 0.13 mm (0.005-in.) shims and eight without shims. Bonding with shims consistently produced a thicker bondline, and the G_{Ic} value for the shimmed specimens was higher. These results tend to confirm earlier suspicions that G_{Ic} increases with bondline thickness for AF-55S in the range of thicknesses tested.

Other G_{Ic} data generated for this program are summarized in Table 2. The bondline thicknesses for the 36 specimens were not measured but appeared to be thin, although the temperature and pressure (T-P) cycle was the same as used for aircraft bonding. No shims were used. The 36 G_{Ic} values varied from 1.70 to 2.68 kJ/m² (9.7 to 15.3 lb/in) with a mean of 2.19 kJ/m² (12.5 lb./in.).

It was noted after bonding that four of the 36 specimens became cocked during curing, creating a side to side tilting of the bondline. As noted in Table 2, these specimens account for four of the nine lowest G_{Ic} values.

1.2 Mixed Mode I and Mode II Tests

As discussed in Section II, the CLS specimen, by its resemblance to typical bonded structure, provides baseline data which are believed to be most directly applicable to bondline crack growth in structure. Hence the mixed mode data presented here are all generated by the CLS specimens. Three monotonically increasing load (MIL) tests were conducted after fatigue testing

TABLE 1. G_{Ic} VALUES FOR SHIMMED AND UNSHIMMED CDCB SPECIMENS

Specimen Number	Bondline Thickness, Microns (inches)		G_{Ic} kJ/M ² (lb/in)
	@ Crack Tip	@ Back End	
<u>Bonded Without Shims</u>			
7-14	152 (0.006)	152 (0.006)	2.22 (12.7)
7-42	178 (0.007)	152 (0.006)	2.28 (13.0)
7-6	127 (0.005)	152 (0.006)	2.21 (12.6)
7-41	203 (0.008)	152 (0.006)	2.28 (13.0)
7-16	203 (0.008)	178 (0.007)	2.22 (12.7)
7-10	152 (0.006)	152 (0.006)	2.38 (13.6)
7-26	178 (0.007)	178 (0.007)	2.24 (12.8)
7-92	152 (0.006)	152 (0.006)	2.28 (13.0)
	168 (0.0066) avg	160 (0.0063) avg	2.24 (12.8) avg
<u>Bonded With 0.005-Inch Shims</u>			
7-83	229 (0.009)	229 (0.009)	2.89 (16.5)
7-55	229 (0.009)	229 (0.009)	2.66 (15.2)
7-23	254 (0.010)	254 (0.010)	2.57 (14.7)
7-21	229 (0.009)	254 (0.010)	2.52 (14.4)
	236 (0.0093) avg	241 (0.0095) avg	2.66 (15.2) avg

TABLE 2. \mathcal{G}_{Ic} VALUES FOR 36 CDCB SPECIMENS OF AF-55S ADHESIVE
(Arranged in Rank Order)

Spec. No.	\mathcal{G}_{Ic} kJ/m ² (lb/in)	Rank	Spec. No.	\mathcal{G}_{Ic} kJ/m ² (lb/in)	Rank	Spec. No.	\mathcal{G}_{Ic} kJ/m ² (lb/in)	Rank
7-43	1.70 (9.7)	1	7-1	2.03 (11.6)	13	7-30	2.34 (13.4)	25
7-60 (3)	1.80 (10.3)	2	7-51	2.08 (11.9)	14	7-54	2.34 (13.4)	26
7-21 (1) (3)	1.82 (10.4)	3	7-23 (1)	2.12 (12.1)	15	7-73	2.34 (13.4)	27
7-31	1.87 (10.7)	4	7-63 (2)	2.12 (12.1)	16	7-82	2.34 (13.4)	28
7-59	1.87 (10.7)	5	7-28	2.17 (12.4)	17	7-20	2.38 (13.6)	29
7-64 (3)	1.87 (10.7)	6	7-89	2.19 (12.5)	18	7-39	2.49 (14.2)	30
7-58	1.89 (10.8)	7	7-3	2.22 (12.7)	19	7-27	2.54 (14.5)	31
7-52	1.96 (11.2)	8	7-12	2.22 (12.7)	20	7-9	2.56 (14.6)	32
7-32 (2) (3)	1.98 (11.3)	9	7-17	2.24 (12.8)	21	7-56	2.56 (14.6)	33
7-35	1.98 (11.3)	10	7-22	2.28 (13.0)	22	7-90	2.57 (14.7)	34
7-37	2.01 (11.5)	11	7-46	2.28 (13.0)	23	7-87	1.66 (15.2)	35
7-79	2.01 (11.5)	12	7-68	2.31 (13.2)	24	7-72	2.68 (15.3)	36

Mean \mathcal{G}_{Ic} = 2.19 kJ/m² (12.51 lb/in)

Standard Deviation = 0.26 kJ/m² (1.50 lb/in)

- (1) Tested to complete fracture.
- (2) Somewhat unusual P-Δ record.
- (3) Tilted bondline.

and side-notching of Specimens CLS-1, CLS-3, and CLS-4. Consequently, in addition to the usual load-displacement data obtained (see section II), examinations of fracture surfaces provided fractographic information on the extents of fatigue and static crack growth.

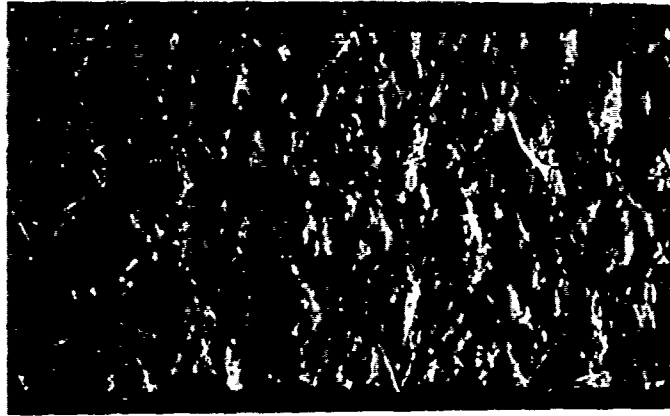
Results of a static test of Specimen CLS-1 indicated a value of \mathcal{G}_{Ic} between 2.40 and 5.27 kJ/m² (13.7 and 30.1 lb/in). The critical \mathcal{G}_I for Specimen CLS-3 was determined to be 2.43 to 3.04 kJ/m² (13.9 to 17.3 lb/in).

Specimen CLS-4 had equal adherend thicknesses of 19.3 mm (0.76 in.) and was side notched such that $b_N = 6.35$ mm (0.25 in.). Equations (5), (18), and (21) were used to compute, after side notching, that $\mathcal{G}_I/\mathcal{G} = 0.215$ and $C_{LS} = 0.0266$.

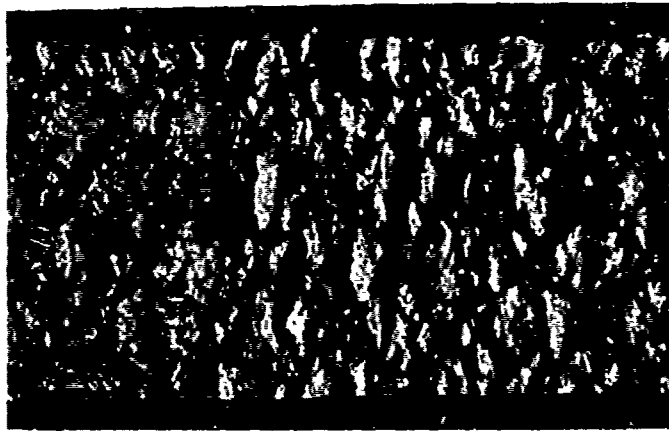
After side notching and subsequent fatigue cycling, Specimen CLS-4 was also increasing-load tested. However, the test was different from that of Specimen CLS-3 in that the loading rate was much higher. A loading rate of about 1.56 kN (350 lb) per millisecond was used. At the instant the crack began propagating the load was between 80 and 102 kN (18 and 23 kip). Thus, \mathcal{G}_{Ic} was between 1.51 and 2.46 kJ/m² (8.6 and 14.1 lb/in). Crack growth began at about 52 milliseconds and ended at about 62 milliseconds after start of ramp-type loading. The total crack growth was about 280 mm (11 inches).

Figures 23 and 24 show the overall and enlarged views of the fracture surface of CLS-1. In the overall view (Figure 23(a)) the area of the pure Mode-I precracking of the Specimen is seen as a set of center of bond (CoB) fingernail markings. The next 96.5 mm (3.8 in.) of fracture surface from the precrack is by mixed-mode fatigue, which occurs along one side of the scrim, near the primer-adhesive interface. This is best seen in the enlargement shown in Figure 23(b) and (c). Recall that the machining operation that reduced the bond width from 25.5 to 4.7 mm (1.005 to 0.186 in) was done after fatigue cycling and before MIL loading.

The point at which MIL crack growth begins is clear in the magnified views (Figure 23(d) and Figure 24(a) and (b)). To the left of this point



(a) Transition Area from top of Figure 23(d) (Approx. 10X)



(b) Transition area from bottom of Figure 23(d) (Approx. 10X)

Figure 24. Magnified fracture surface photographs for specimen CLS-1.

the fatigue area appears as a flat fracture near one interface. The scrim layer and most of the adhesive is on the top, while the impression of the scrim and a very thin layer of adhesive is on the bottom. Fracturing under mixed-mode MIL loading is radically different from that observed with Pure Mode I. The fracture surface is featured with inclined flakes on both top and bottom. These flakes appear to be areas of cracking that occur normal to the Mode I loading, originating from the interface and extending upward and left on the bottom fracture surface, and downward and right on the mating surface. Fracture surface photographs for Specimen CLS-3 are similar in appearance.

These fracture surface photographs suggest that mixed-mode fracture perhaps occurs in two stages. By this hypothesis, Stage I would be the multiple initiation and growth of microcracks that are inclined to the bond line, their density highest close to the tip of the advancing macroscopic bondline crack. Stage II would be the advancement of the macroscopic crack by linking up with the inclined microcracks.

The flake-type fracture surface that occurred in Specimen CLS-1 and CLS-3 at low-loading rate is not present in Specimen CLS-4. Instead, the fracture appearance resembles that of a pure Mode I test.

2 SUSTAINED LOAD STRESS CORROSION CRACKING TESTS

Both pure Mode I and mixed Mode I and Mode II stress corrosion cracking (SCC) tests were conducted by prolonged immersion of loaded specimens in deionized water. The pure Mode I tests were conducted using CDCB specimens at 316°K (110°F), 322°K (120°F), 327°K (130°F), and 333°K (140°F). The mixed mode tests were conducted using a CLS specimen at 333°K.

2.1 Mode I SCC Testing

The first group of SCC specimens consisted of CDCB specimen 7-22 and 7-46. Four test temperatures were used (316°, 322°, 327°, and 333°K) and crack growth rate, da/dt , values were obtained up to an applied σ_I of 0.876 kJ/m² (5 lb/in). The data are plotted in Figure 25. The four curves fall into two groups, low rate group at 316°K (110°F) to 322°K (120°F) and higher rate group at 327°K (130°F) to 333°K (140°F).

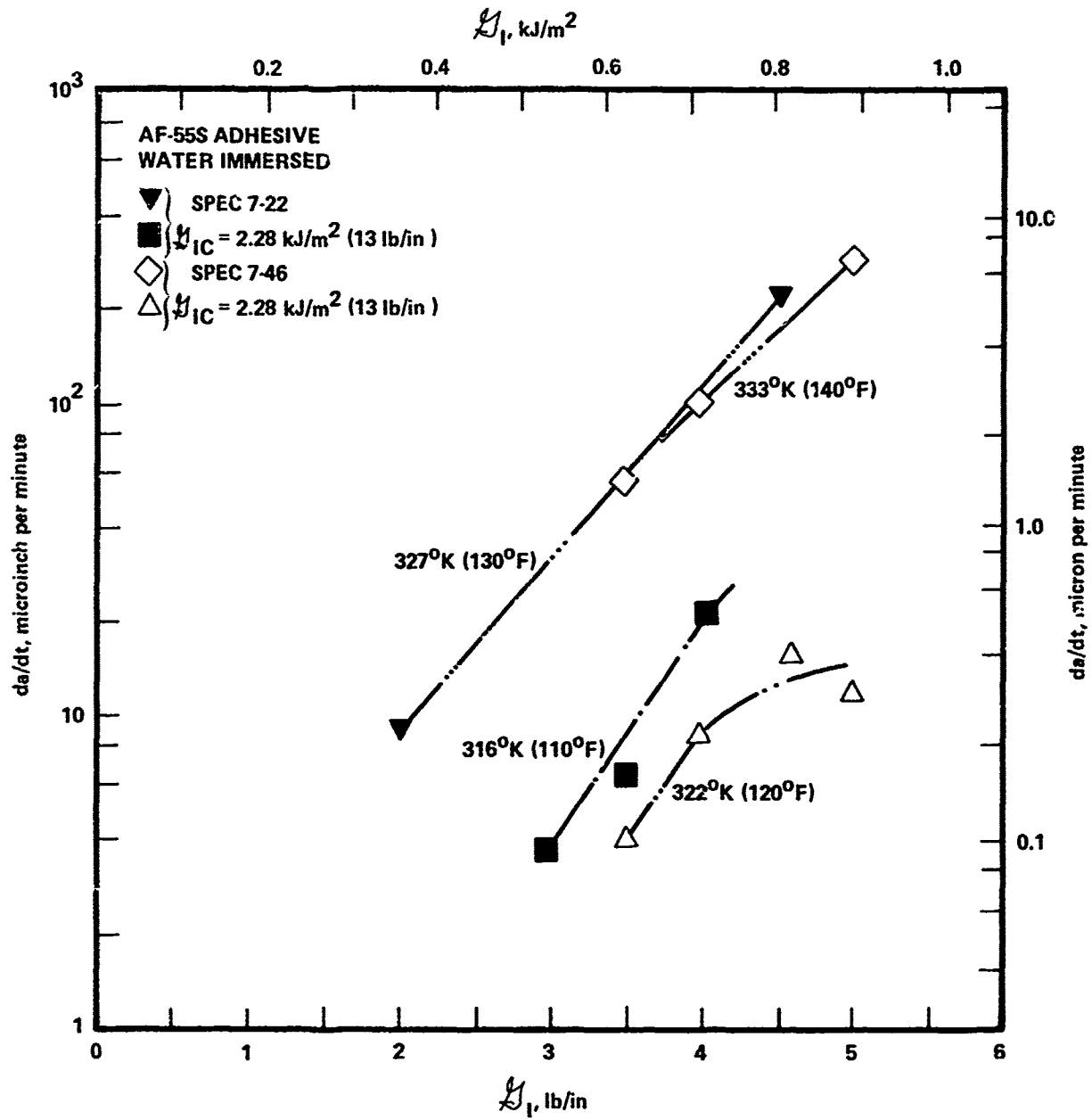


Figure 25. Pure mode I sustained load crack growth

Specimen 7-22 and 7-46 were bonded without shims and consequently had a relatively thin bond line. Data on Specimens 7-55 and 7-83, which were shimmed for bonding to a thickness of 0.13 mm (0.005 in.), are plotted as solid points in Figure 26. These data show a plateau where the crack growth rate is between 0.14 micron (5.5 microinch) and 1.0 micron (40 microinch) per minute and relatively independent of applied \mathcal{G}_I from $\mathcal{G}_I = 0.58 \text{ kJ/m}^2$ (3.03 lb/in) to $\mathcal{G}_I = 1.3 \text{ kJ/m}^2$ (7.55 lb/in).

The $\mathcal{G}_{I\text{SCC}}$ values cannot be reliably estimated from these data. To obtain $\mathcal{G}_{I\text{SCC}}$ estimates, tests would have to be carried out for a longer period of time, such as 6 months.

AF-55S adhesive, BR-127A primer and the phosphoric acid anodize (PAA) process were used to prepare the shimmed and unshimmed specimen groups. In Figure 26 the data from these two groups are compared to one another and to data from a third group tested earlier (Reference 9), also in $327^\circ - 333^\circ\text{K}$. The third group, bonded with shims, was prepared using AF-55S adhesive and BR-127A primer, but the surface preparation was FPL etch. There are differences between the shimmed and unshimmed, but the major difference is between the specimens with PAA-treated adherends and FPL-treated adherends. For example, the crack growth rate in the shimmed PAA-treated adherends at a \mathcal{G}_I of 0.61 kJ/m^2 (3.5 lb/in) is about 1000 times less than that for the FPL etched adherends using the same AF-55S adhesive system.

It is informative to examine the fracture surface to identify the location of cracking. For FPL adherends crack growth proceeded near the metal-to-primer interface, while in the PAA adherends, it occurred in the bulk adhesive. Thus the data for specimens with PAA adherends show the crack growth resistance of bulk AF-55S. Data for specimens with FPL adherends show the crack growth resistance near the interface.

2.2 Mixed Mode SCC Testing

A limited amount of mixed modes I and II sustained load testing was done using side-notched specimen CLS-8. This specimen had adherend thicknesses

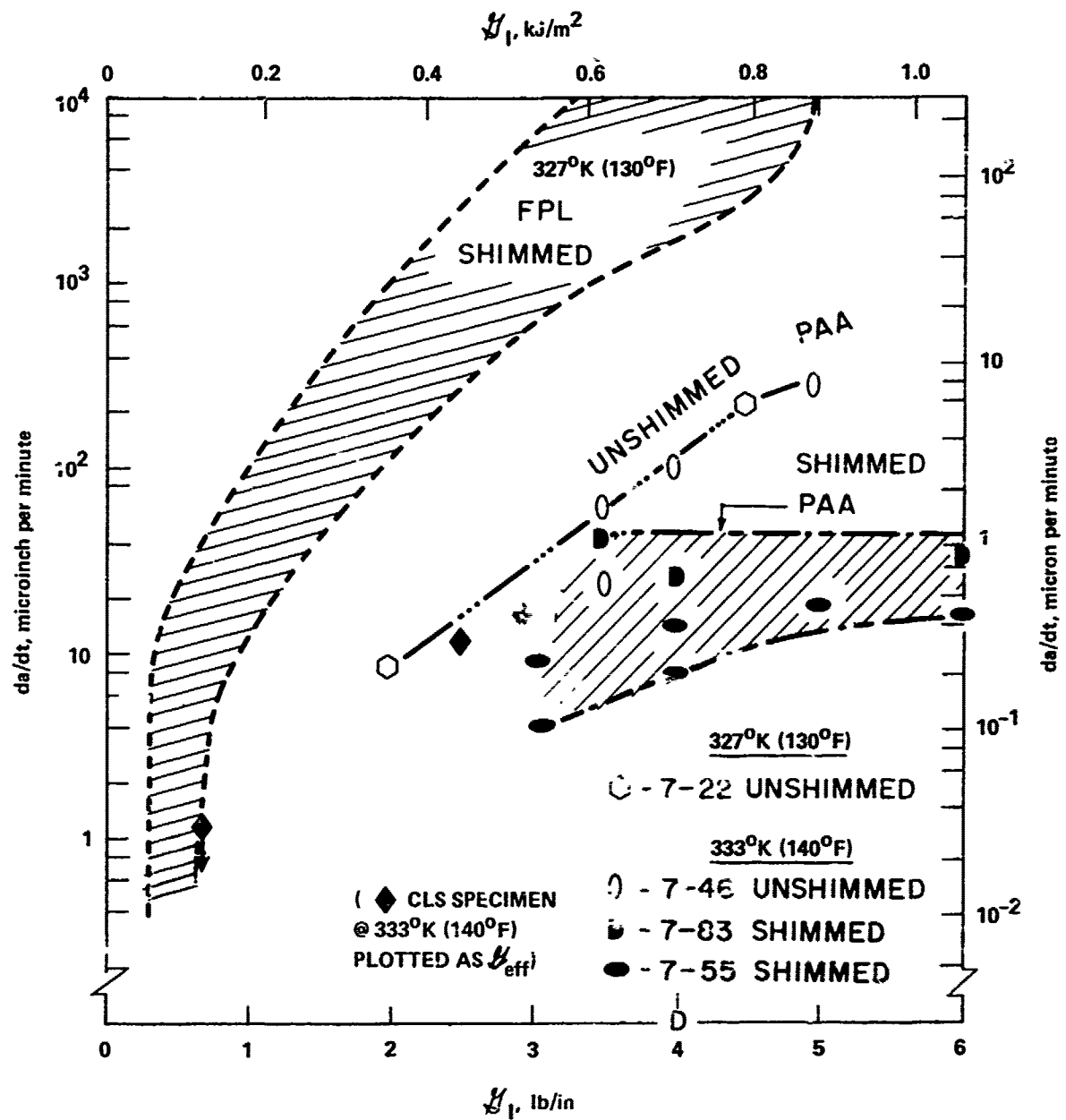


Figure 26. Pure mode I SCC data in 327°K - 333°K (130°F - 140°F) water.

$t_1 = 9.5 \text{ mm}$ (0.375 in.) and $t_2 = 19.5 \text{ mm}$ (0.767 in.) and was side notched from an initial width of 25.4 mm (0.999 in.) such that $b_N = 3.6 \text{ mm}$ (0.140 in.). From Equations (15), (18), and (21) it was calculated that after side notching $\mathcal{G}_I/\mathcal{G} = 0.106$ and $C_{LS} = 0.0129$.

Crack lengths were estimated from compliance measurements during periodic unloading and reloading as described in Section II, Subsection 2.3. This procedure was necessary because the absolute displacement gage reading gradually increased during sustained loading irrespective of crack extension.

The data points obtained on Specimen CLS-8 are as follows: $P = 40 \text{ kN}$ (9.0 kip), $\mathcal{G}_I = 0.18 \text{ kJ/m}^2$ (1.04 lb/in.), $da/dt = 0.47 \text{ micron}$ (18 microinches) per minute; and $P = 37 \text{ kN}$ (8.3 kip), $\mathcal{G}_I = 0.16 \text{ kJ/m}^2$ (0.89 lb/in.), $da/dt = 0.31 \text{ micron}$ (12 microinches) per minute. No measurable growth occurred in 4 months for $P = 29.5 \text{ kN}$ (6.63 kip) and $\mathcal{G}_I = 0.10 \text{ kJ/m}^2$ (0.57 lb/in.).

Plotted as \mathcal{G}_I versus da/dt these points would lie above and to the left of the pure Mode I data. The definition of effective strain energy release rate, obtained from the fatigue data (see Equation (37)), is

$$\mathcal{G}_{\text{eff}} = \left(1 + \frac{2\mathcal{G}_{\text{II}}}{\mathcal{G}} \right) \mathcal{G}_I \quad (33)$$

Replacing \mathcal{G}_I by \mathcal{G}_{eff} , the data points are plotted as darkened diamonds in Figure 26. Although they fall within the region of the Pure Mode I points, the data are not really sufficient to draw conclusions about the effect of \mathcal{G}_{II} on mixed-mode sustained-load induced crack growth.

3 FATIGUE TESTS

Fatigue test data were obtained using the CDCB and the CLS specimens. The Mode I CDCB specimens were tested in laboratory air at 3 Hz and 30 Hz at both $R = 0.1$ and 0.6, and immersed in 333°K (140°F) water at 3 Hz and 0.25 Hz

and $R = 0.1$. The mixed mode CLS specimens were tested in laboratory air at 3 Hz and $R = 0.1$ only.

The fatigue data are plotted as $\log(da/dN)$ vs. $\log(\Delta\mathcal{G}_I)$ and fitted with straight lines of the form

$$\frac{da/dN}{a_o} = C_a \left(\frac{\Delta\mathcal{G}_I}{\mathcal{G}_o} \right)^n \quad (34)$$

where C_a and n are dimensionless empirical constants, whereas a_o and \mathcal{G}_o are standard normalizing factors. \mathcal{G}_o was defined in Equation (20); a_o is given by

$$a_o = 0.0254 \text{ micron (1.00 microinch)} \quad (35)$$

3.1 Mode I Testing in Laboratory Air at 3 Hz.

The baseline constant-amplitude fatigue test condition was a laboratory air room temperature (RT) environment and a cyclic frequency of 3 Hz. Six Pure Mode I specimens were tested at two range ratios, $R = 0.1$ (baseline) and $R = 0.6$. The data are plotted in Figure 27.

For each plotted point the crack advanced at least 5 mm (0.2 in.). If the crack growth increment was less, the point was usually not plotted. The only exceptions are the points shown with downward arrows. For these, a large number of cycles N were applied with very little crack growth. The locations of these points on the da/dN scale are obtained by the equation

$$da/dN = \frac{5 \text{ mm (0.2 in)}}{\Delta N} \quad (36)$$

Equation (36) always overestimates the da/dN value; therefore the downward arrow is used.

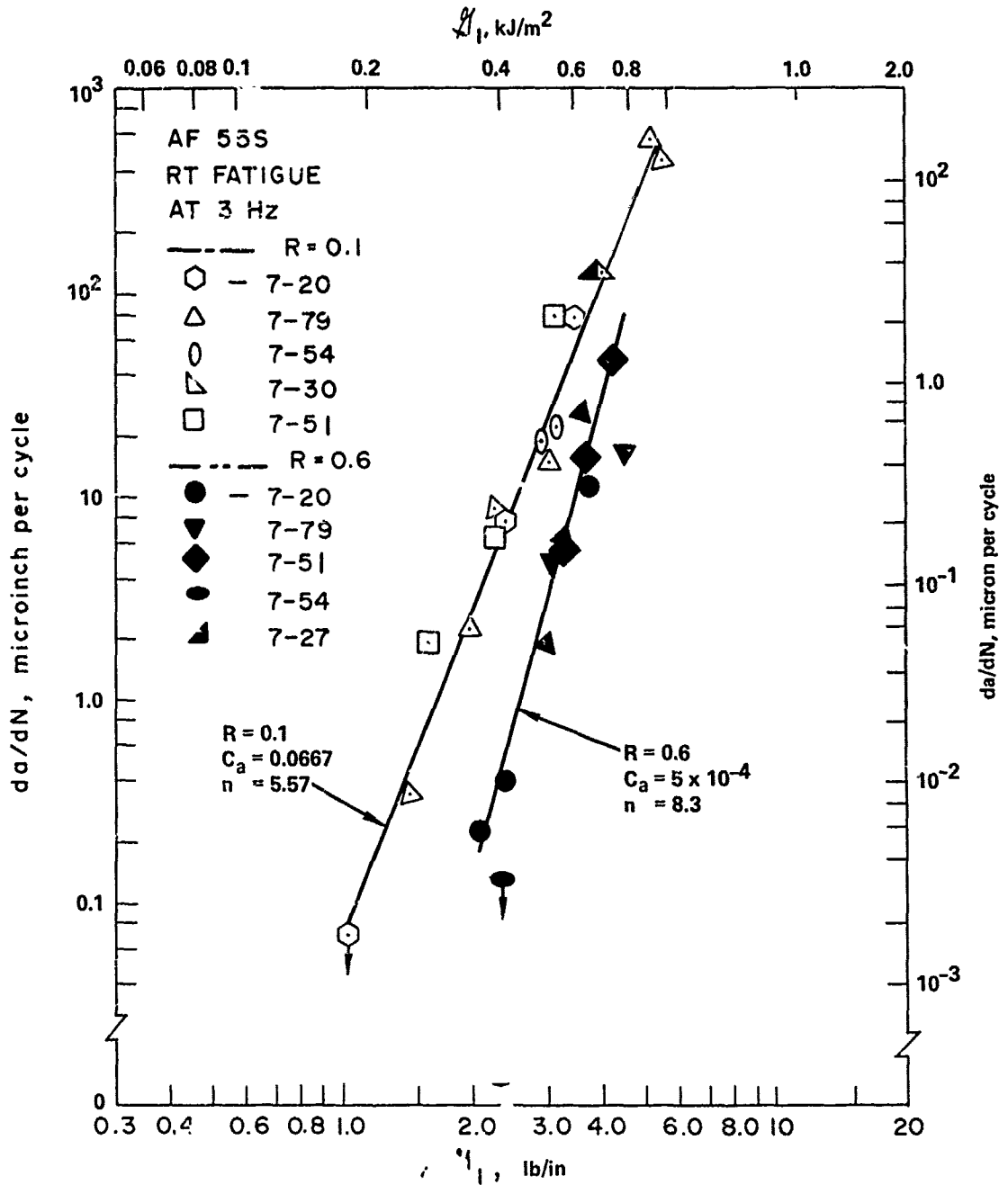


Figure 27. Mode I Fatigue Crack Growth In Room Temperature Air

The constants in Equation (34) for the best-fit lines are: $C_a = 0.0667$ and $n = 5.57$ for $R = 0.1$; $C_a = 5 \times 10^{-4}$ and $n = 8.3$ for $R = 0.6$. Although the data at $R = 0.6$ are more scattered, the main feature is the increased slope of the da/dN curve, 8.3 versus 5.57. The steepness of slope means that very small changes in $\Delta\mathcal{G}_I$ cause very large changes in da/dN . For $R = 0.6$ for example, a 5 percent increase in $\Delta\mathcal{G}_I$ (caused by a 2.5 percent increase in stress) will increase da/dN by a factor of 1.5.

3.2 Mixed-Mode Testing in Laboratory Air at 3 Hz

The overall dimensions of the eight CLS specimens fatigue tested are shown in Table 3. These specimens represent a variety of conditions. Four different adherend thickness combinations are included, leading to 4 different values of the factor C_{LS} in Equation (19). A few fatigue data points were obtained on Specimens CLS-1 and CLS-3 after side notching and before MIL testing (see Figures 12 and 13 for side notch dimensions). Further, the bonded panel from which Specimens CLS-1 and CLS-1A were machined was prepared differently from the others. First, surface preparation of these 2 specimens was by FPL etch. Secondly, the two 12.7 mm (0.5 in.) adherends were achieved by laminating a 7.9 mm (0.312 in.) plate to a 4.8 mm (0.188 in.) sheet. Despite all these variations, the ratio $\mathcal{G}_I/\mathcal{G}$ was almost constant (between 0.205 and 0.258) for all these tests.

The results of these tests are plotted in Figure 28 as da/dN versus the Mode I component of strain energy release rate, $\Delta\mathcal{G}_I$. As plotted, the points are significantly above and to the left of the best-fit line for the $R = 0.1$ Pure Mode I data from Figure 27.

To account for this difference, an effective strain energy release rate is defined as

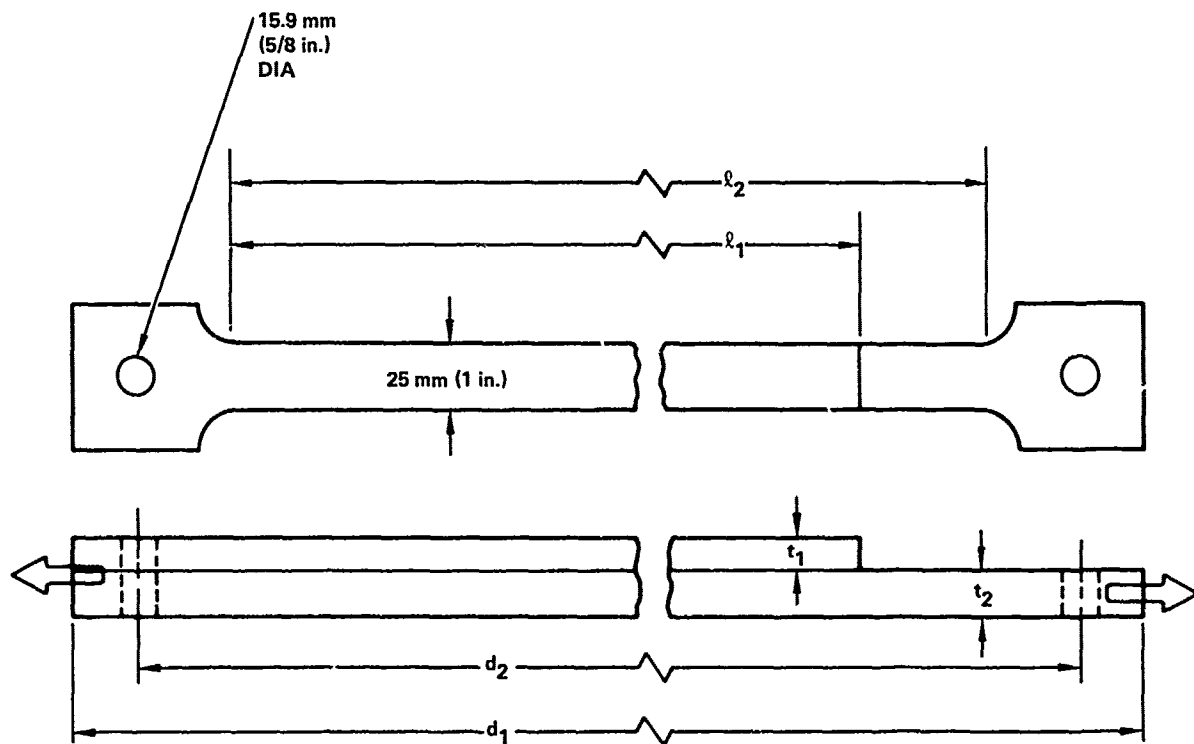
$$\Delta\mathcal{G}_{\text{eff}} = \left(1 + \frac{2\mathcal{G}_{II}}{\mathcal{G}}\right)\Delta\mathcal{G}_I \quad (37)$$

Note that for pure Mode I, $\Delta\mathcal{G}_{\text{eff}}$ and $\Delta\mathcal{G}_I$ are equal, whereas for a CLS specimen with (for example) $\mathcal{G}_I/\mathcal{G}$ of 0.205, $\Delta\mathcal{G}_{\text{eff}}$ is larger than $\Delta\mathcal{G}_I$ by a factor

TABLE 3. CLS SPECIMEN DIMENSIONS

Specimen No.	t_1 mm (in.)	t_2 mm (in.)	d_1 mm (in.)	d_2 mm (in.)	l_1 mm (in.)	l_2 mm (in.)	C_{LS} Eq.(22)	$S_{1/S}$
CLS-1*	12.7(0.5)	12.7(0.5)	1168(46)	1099(43.3)	800(31.5)	953(37.5)	0.0102	0.205
CLS-1A*	12.7(0.5)	12.7(0.5)	1168(46)	1099(43.3)	800(31.5)	953(37.5)	0.0102	0.205
CLS-2	19.3(0.76)	9.7(0.38)	914(36)	838(33)	502(19.8)	648(25.5)	0.0226	0.258
CLS-3	19.3(0.76)	9.7(0.38)	914(36)	838(33)	502(19.8)	648(25.5)	0.0226	0.258
CLS-4	19.3(0.76)	19.3(0.76)	1168(46)	1099(43.3)	800(31.5)	953(37.5)	0.0067	0.205
CLS-5	9.7(0.38)	9.7(0.38)	914(36)	838(33)	502(19.8)	648(25.5)	0.0135	0.205
CLS-6	9.7(0.38)	9.7(0.38)	914(36)	838(33)	502(19.8)	648(25.5)	0.0135	0.205
CLS-7	9.7(0.38)	9.7(0.38)	914(36)	838(33)	502(19.8)	648(25.5)	0.0135	0.205

*Laminated



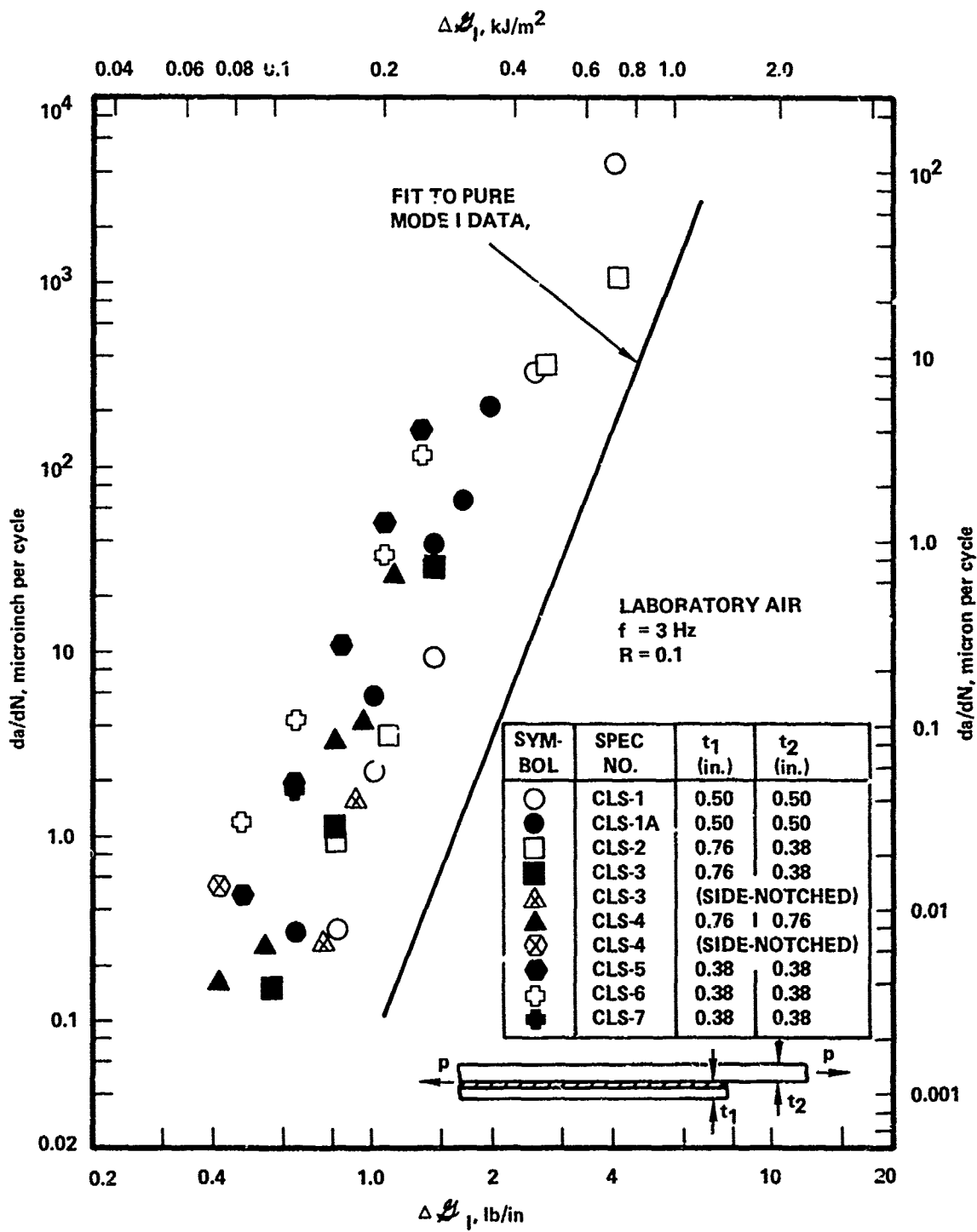


Figure 28. Fatigue crack growth data from mixed-mode CLS specimens

of 2.59. When replotted in Figure 29 as $\Delta \mathcal{G}_{\text{eff}}$ versus da/dN , the pure Mode I data fit line is a reasonably good representation of the mean of the mixed mode CLS specimen data.

Equation (37) provides a means for interpolating to estimate da/dN for mixed mode cases with $\mathcal{G}_I/\mathcal{G}$ ratios between 0.2 (as in the CLS specimens) and 1.0 (pure Mode I). The equation is strictly empirical, and its form is subject to change in the future as a variety of mixed mode fatigue crack growth data becomes available.

3.3 Elevated Temperature Fatigue Testing

Mode I CDCB specimens were fatigue tested at $R = 0.1$ and 3 Hz or 0.25 Hz while immersed in hot water. The da/dN data from these tests are compared in Figure 30 to the baseline result, $R = 0.1$, $f = 3$ Hz., RT air environment. While the slope of the curve does not change much, da/dN increases by about one order of magnitude due to the hot water environment. Based on the two specimens tested at 3 Hz., there is not a substantial difference in da/dN between water immersion at 327°K and 333°K (130°F and 140°F). There does appear to be a small cyclic frequency effect, however. The da/dN value is higher by about a factor of 3 when the cyclic frequency is 0.25 Hz. instead of 3 Hz.

The elevated temperature fatigue data at both frequencies are fitted by Equation (34) with a slope n of 5.03. The constant C_a is 1.75 for $f = 3$ Hz. and 5.25 for $f = 0.25$ Hz.

3.4 High Frequency Testing

Four Mode I CDCB specimens were fatigue tested in room temperature air (RT) at $R = 0.1$ and $R = 0.6$ and a cyclic frequency of 30 Hz. Based on past test results on other structural adhesives, it was expected that increasing the cyclic frequency above 3 Hz. would significantly reduce the da/dN value.

The data from the four specimens tested at 30 Hz. are plotted in Figure 31. Least squares fits of the data are obtained for each range ratio in the form of Equation (34). For 30 Hz. and $R = 0.1$, the constants are

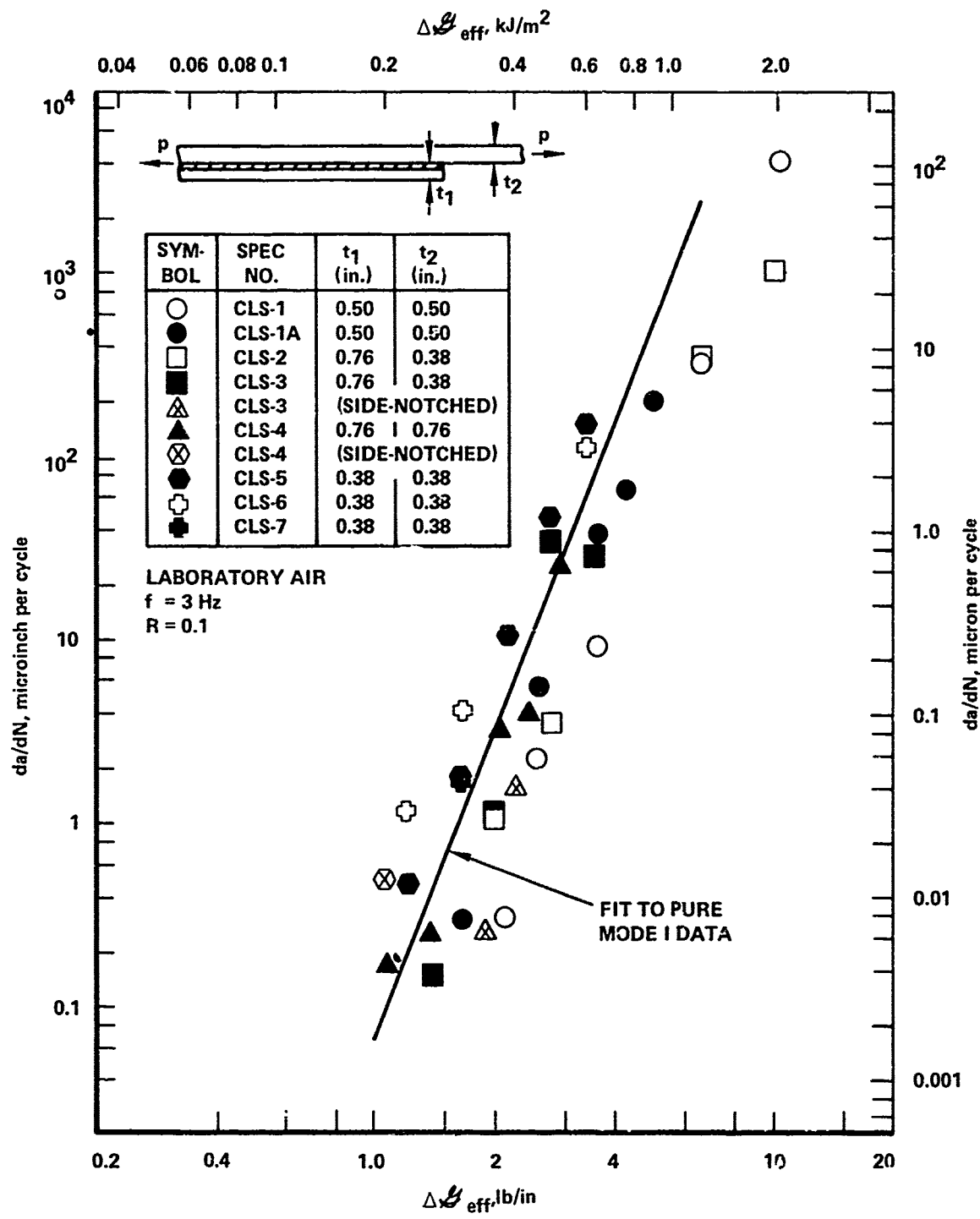


Figure 29. CLS fatigue data using $\Delta \sigma_{eff}$ to account for mode II

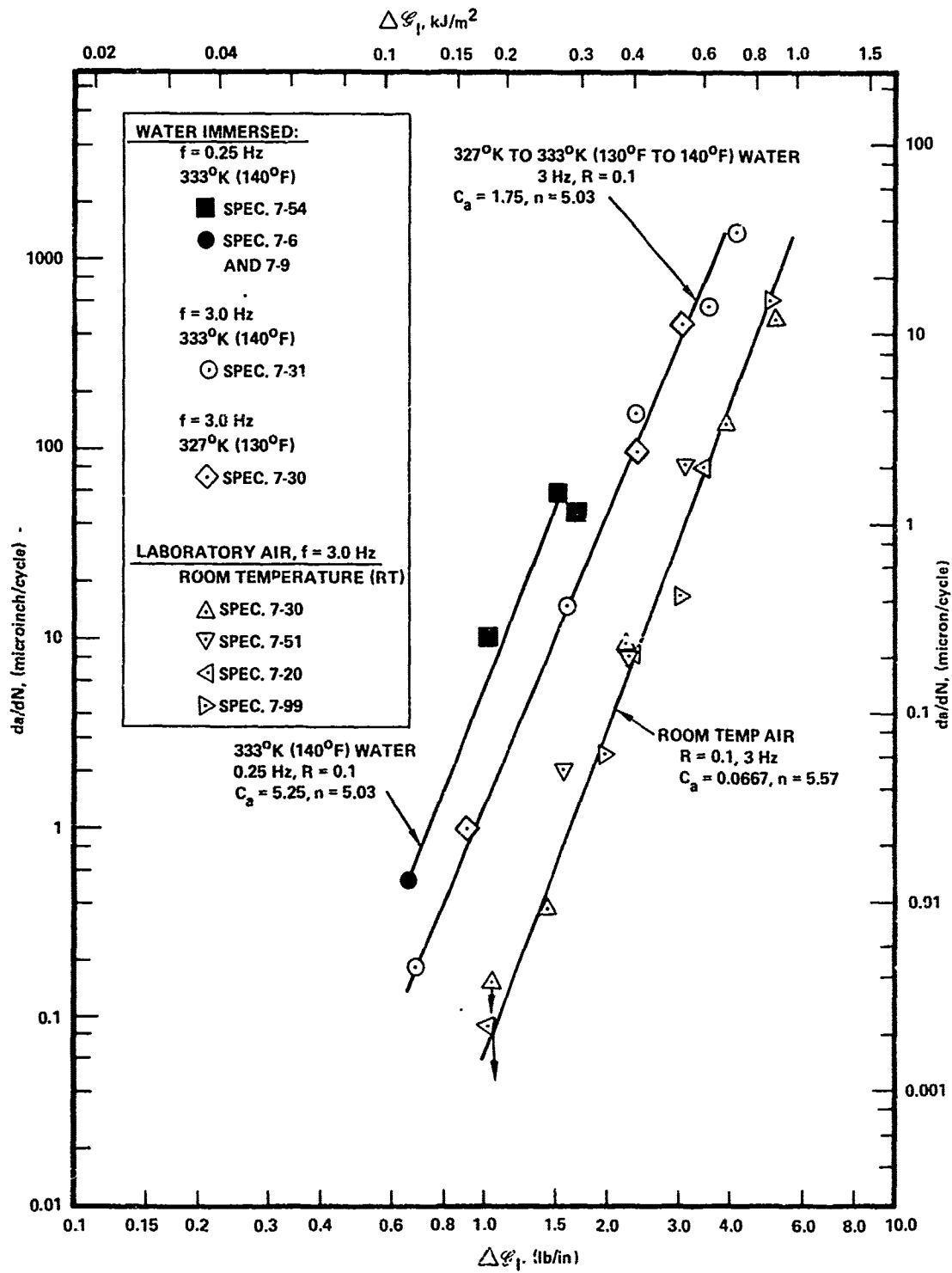


Figure 30. Mode I fatigue crack growth rate data, RT air and 333°K (140°F) water immersion

$C_a = 0.01$ and $n = 6.0$. For 30 Hz. and $R = 0.6$, the constants are $C_a = 7.2 \times 10^{-6}$ and $n = 9.8$. Figure 31 shows these best-fit lines and compares them to the best fit lines for the same two R values and $f = 3$ Hz. Increasing the cyclic frequency from 3 Hz. to 30 Hz. caused reductions in crack growth rate of a factor between 4 and 10.

3.5 Discussion of Baseline Fatigue Test Results

In pure Mode I, fatigue crack propagation of bondline cracks can occur at values of $\Delta\mathcal{G}_I/\mathcal{G}_{Ic}$ of 0.1 or less. Furthermore, the Mode II component has a definite detrimental effect in fatigue but seems not to affect the critical value of \mathcal{G}_I for increasing load testing. Thus fatigue will tend to be a more critical condition for a bondline crack than a single large increasing load.

The most striking thing about the fatigue crack growth data is the very steep power-law slope of the da/dN curve. For metals the relationship between da/dN and stress intensity K is often written in the form

$$da/dN = C_m \Delta K^{2n} \quad (38)$$

(where the 2 makes the n here comparable with that in Equation (34) because \mathcal{G} varies as $(\Delta K)^2$). For aluminum and steel, $2n$ is between 2 and 4, so n is between 1 and 2. This contrasts with n values of 5.02 to 9.8 for the bondline crack growth test results presented here.

The steep slope on the da/dN curve for adhesives means that small changes in stress cause large changes in crack growth rate. There is a greater sensitivity to changes in applied stress than in metals.

Furthermore, errors in estimated stress are greatly magnified when converted to errors in fatigue crack growth life prediction, because the factor error in stress is raised to the $2n$ power. For example, for $R = 0.1$, laboratory air, 3 Hz. the factor error in estimated da/dN arising from an error of 3 percent in estimated stress is calculated as

$$\text{Error} = (1.03)^{2n} = (1.03)^{11.14} = 1.39$$

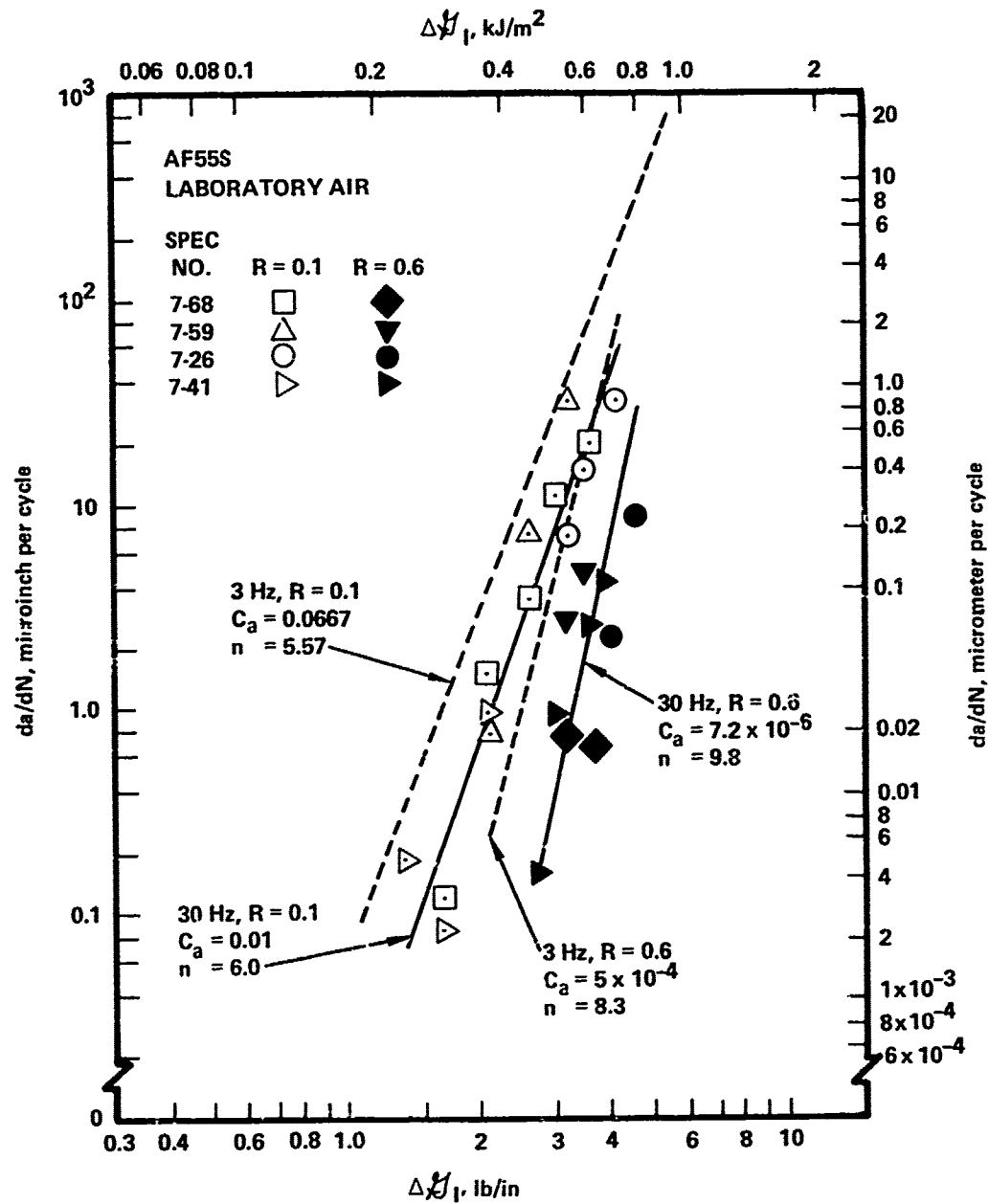


Figure 31. Effect of 30 Hz frequency on crack growth in room temperature air

With these steep slopes, it may often be difficult to design for finite life, since minor design alterations or small analysis errors could cause short lives for what had appeared to be an acceptably-fatigue-designed structural member. This means that the value of $\Delta\mathcal{G}_{Ith}$, the no-growth threshold, may be even more important for adhesives than for metals.

Crack growth threshold data are expensive to obtain because of the long test times required. This is even more true in adhesives than in metals because the material is time dependent (so high-frequency values of $\Delta\mathcal{G}_{Ith}$ may be misleading), and because the increment of crack growth required for a confident reading of da/dN seems to be substantially longer in adhesives than in metals.

However, the steepness of slope of the da/dN curve makes it reasonable to use a conservative procedure for estimation of $\Delta\mathcal{G}_{Ith}$. It is fairly certain that at lower values of da/dN the da/dN curve is concave downward in log-log space. Thus, extrapolation linearly downward to estimate low da/dN values is conservative.

Arbitrarily selecting 1 mm (0.04 in.) per year as a practical value for "no growth," and extrapolating the straight line fits of the da/dN data down to that value of da/dN , conservative estimates of $\Delta\mathcal{G}_{Ith}$ are obtained. These estimates of the threshold are listed in Table 4.

In addition to the slope of the da/dN curve being steeper, the cyclic frequency effect on da/dN (particularly in laboratory air) is stronger for these bondline cracks than is typical for cracks in metal. Thus, laboratory testing at high cyclic frequencies has at least two serious drawbacks. First and most obvious, the da/dN values at high frequency are inapplicable to prediction for service fatigue loading at slower frequencies, and such predictions would be unconservative. Secondly, because the metal da/dN properties do not significantly improve with increasing frequency, testing at higher frequency may cause metal failure prior to bondline crack growth.

For the purposes of this research effort, a cyclic frequency of 3 Hz. was felt to be a good compromise between the inapplicability of results obtained from testing at high cyclic frequency and the costliness of testing at lower frequency.

TABLE 4. CONSERVATIVE FATIGUE THRESHOLD VALUES BY EXTRAPOLATION

Environment	Frequency (Hz)	R	$\frac{da/dN}{a_0}$ @ σ_{Ith}	σ_{Ith}/σ_0
333 ^o K (140 ^o F) Water	0.25	0.1	5.07×10^{-3}	0.252
	3.0	0.1	4.23×10^{-4}	0.191
R.T. Laboratory Air	3.0	0.1	4.23×10^{-4}	0.403
	30	0.1	4.23×10^{-5}	0.402
	3.0	0.6	4.23×10^{-4}	0.980
	30	0.6	4.23×10^{-5}	1.198

*Growth rate for $da/dN = 1$ mm/year (1 in/25 yr)

SECTION IV
METHODOLOGY DEMONSTRATION

The work presented in this section covers the final phase of this research program, the verification of prediction methodology.

Baseline test results indicated that bonded thin-sheet structure has a high tolerance to bondline flaws. There is a tendency for the structure to be critical in the adherend, even with a bondline flaw in the adhesive. Careful selection of the test specimen configuration and test conditions is critical so that the bondline cracks actually do propagate. Several things can be done to increase the tendency for the bondline crack to propagate without the adherend yielding; namely:

1. Increase the adherend thickness.
2. Increase the Mode I component of strain energy release rate of the bondline crack by increasing the induced bending moment at the tip of the flaw.
3. Load in fatigue rather than monotonically.
4. Use a warm, moist environment.

The bonded structural specimen selected for methodology demonstration, based on the above considerations, was a single lap joint specimen. Two adherend thicknesses were selected. The thicker adherend specimens were tested first with the primary goal of succeeding in obtaining crack propagation and fracture in the adhesive layer. Having achieved this goal, the thinner adherend specimens were then tested in order to more closely simulate practical fuselage skin thicknesses.

1 TEST PROGRAM

1.1 Thick-Adherend Single Lap Joint Tests

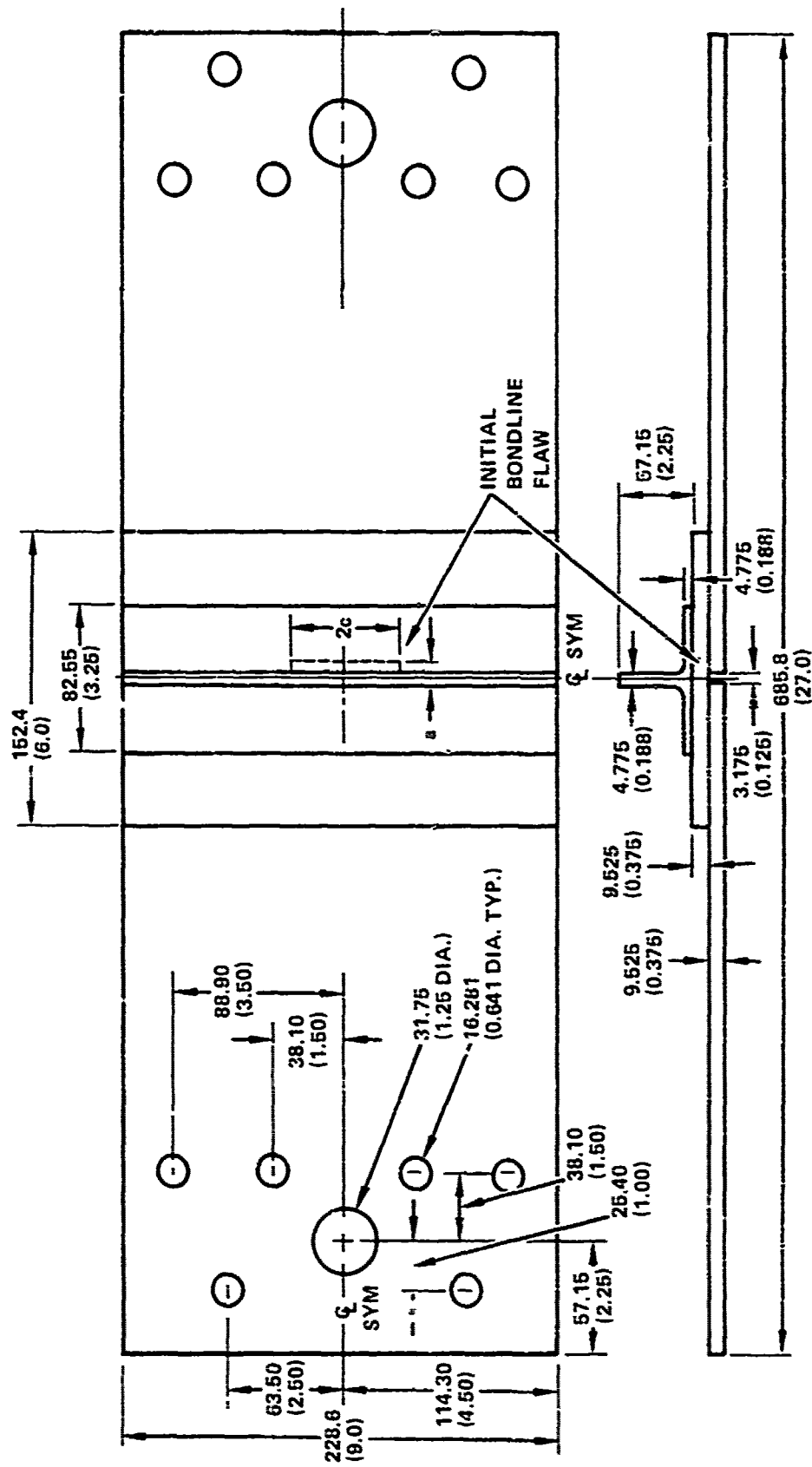
Six structural bonded single lap joints with initial bondline flaws were constant-load-amplitude fatigue tested in laboratory air (30-50% RH; 294^o-297^oK, 69^o-75^oF) at an applied maximum tension load of 0.525 kN per mm (3 kips per inch) of width, R = 0.1, and a cyclic frequency of 3 Hz.

The objectives of these tests were as follows:

1. To obtain crack propagation and fracture in the adhesive layer under cyclic loading in laboratory air without metal yielding or metal fatigue. In similar tests of joints with bondline preflaws (References 8, 9) the metal usually failed before the bondline flaw had grown any discernable amount.
2. To monitor crack growth and obtain data on crack size, shape, and location versus number of cycles.
3. To observe the sensitivity of the crack growth life to differences in initial flaw size.
4. To evaluate the use of baseline data and a LEFM approach in estimating the crack growth rates in the adhesive layer.

The following paragraphs discuss the specimen configuration for the thick adherend specimen and the steps in specimen fabrication, including introduction of preflaws. The test procedures are then described, including the two methods used in crack growth monitoring.

1.1.1 Specimen Configuration and Fabrication. - As shown in Figure 32, the test specimen was a single lap joint 229 mm (9 in.) wide. Thick (10 mm, 0.375 in.) 7075-T6 bare aluminum plate was used for the main skin and doubler plate to induce damaging stresses in the adhesive layer but not in the metal. The tee extrusion bonded to the doubler plate was not intended to carry much in-plane loading, but rather to provide an appropriate way to constrain the lateral bending of the joint. This was accomplished by connecting the out-standing leg of the tee to an externally mounted beam using flexures.



NOTE: DIMENSIONS ARE IN MILLIMETERS WITH CORRESPONDING VALUES IN INCHES GIVEN IN PARENTHESES

Figure 32. Structural single lap joint specimen with thick adherends

As a first step in specimen fabrication, a 229 by 686 mm (9 by 27 in.) piece of 10 mm (0.375 in.) plate was machined, including the grip holes. This piece was not cut in half until after bonding. In this way, the grip holes of the final specimens would be perfectly aligned. Along the eventual split line and across the full width of this piece, a groove 3 mm (0.125 in.) wide was milled partially through the thickness on the to-be-bonded surface. The tee and doubler pieces were machined to final size, and all pieces were cleaned by the Phosphoric Acid Anodize process and primed with BR-127A primer.

The initial flaw in each specimen was in the adhesive layer between the doubler plate and the main skin adjacent to the split line. During layup, teflon tape 89 micron (0.0035 in.) thick was attached to the skin piece and the adhesive was trimmed away where each initial flaw was required. By this method there was no initial degradation of the bond quality in the neighborhood of the flaw. Six specimens were fabricated: Specimen SLJ-1 and -2 contained no initial flaws; SLJ-3 and -4 contained across-the-width flaws 13 mm (0.5 in.) deep; and SLJ-5 and -6 contained 51 mm (2 in.) wide, 13 mm (0.5 in.) deep initial flaws, centered on the longitudinal centerline of the specimen.

All six specimens were cured together at $389^{\circ}\text{--}400^{\circ}\text{K}$ ($240^{\circ}\text{--}260^{\circ}\text{F}$) and 276-345 kPa (40-50 psi) pressure. A cooldown at 339°K (150°F) was employed prior to removal from the autoclave. The adhesive squeezed out into the split-line groove in the main skin, as would have occurred had the skin been split in half prior to bonding. The squeezed-out material blocked the edge of the joint, which could be important in reducing both the effects of environment and, to a lesser extent, the stress concentration at the edge of the bondline. After a C-scan of each specimen to confirm the dimensions of the intended flaws and the uniformity of bond quality, the skin piece was split in half with a 3 mm (0.125 in.) milling cut which precisely met the bottom of the existing groove, leaving intact the squeezed-out adhesive that had filled the groove.

1.1.2 Crack Growth Monitoring. - The primary method of flaw growth monitoring was an ultrasonic method using a contact technique. Three 13 mm (0.5 in.) diameter ultrasonic transducers were bonded into position around the existing precrack so that a signal was triggered after about 6 mm (0.25 in.) of crack growth in any direction. At that time a hand scan was

used to outline the estimated crack. Subsequent hand scans about every 2000 fatigue cycles outlined the progressing shape of the flaw throughout the test.

Part way through the test program, a second crack monitoring procedure was implemented. Displacement gages were placed across the gap of the joint, near the side edges of the specimen. Periodically during the tests, load-versus-displacement plots were obtained. The measured compliances (inverse slope of the load-displacement curve) were compared to computed finite element results given in Figure 33. From the comparison, the debond length was estimated. Note in Figure 33 that excellent correlation was obtained between the measured and computed compliances for the two known initial flaw conditions of no initial flaw and a 12.7 mm (0.5 in.) deep cross-the-width flaw. Furthermore, the estimated compliance is extremely sensitive to crack size, doubling during the first inch of crack growth. Due to its accuracy and sensitivity, the compliance method was a reliable method for crack growth monitoring in this case.

1.2 Thin-Adherend Single Lap Joint Tests

It was desired to conduct similar tests of precracked joints using thinner adherends in order to more closely simulate fuselage structure. The problem with thinner adherends is that the stresses in the metal adherends are higher, and the failure tends to occur by adherend fatigue rather than by crack growth in the adhesive. The results of the thick adherend tests and the baseline data from the Mode I RT fatigue and environmental fatigue tests were used to design thin adherend test specimens and test conditions which would be expected to fail by crack propagation in the adhesive.

Six preflawed structural single-lap joints with 3.2 mm (0.125 in.) adherends were constant-amplitude fatigue tested in 333°K (140°f) deionized water. The specimen configuration is shown in Figure 34. The specimen configuration is similar to the previously-tested single-lap-joint specimens with thicker adherends. The main differences other than the thickness are that, for the thin-adherend specimens, the width of the base of the tee-member was reduced from 76 mm (3.0 in.) to 61 mm (2.4 in.), and the overlap length between the doubler and each skin member was increased from 76 mm (3.0 in.) to

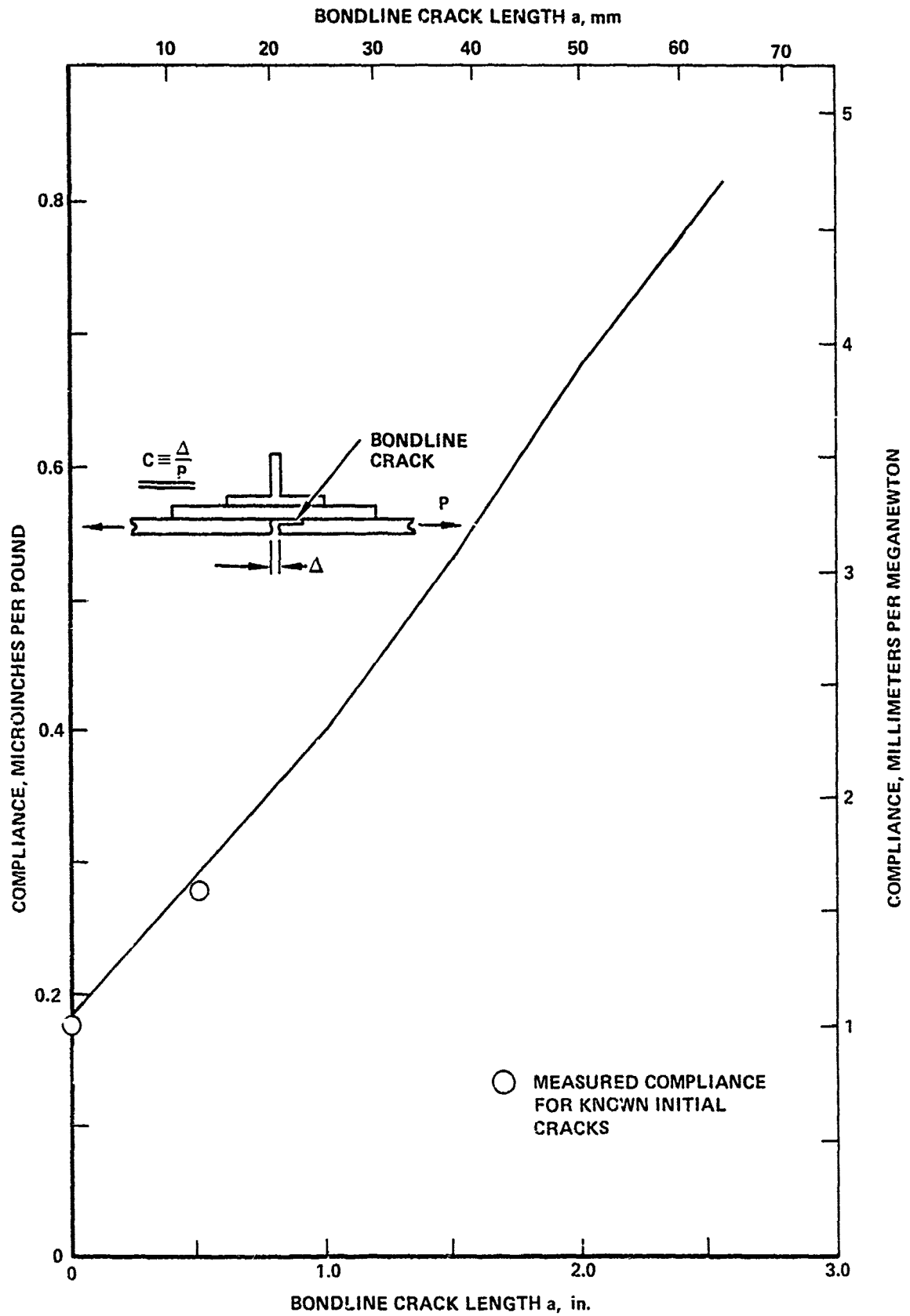
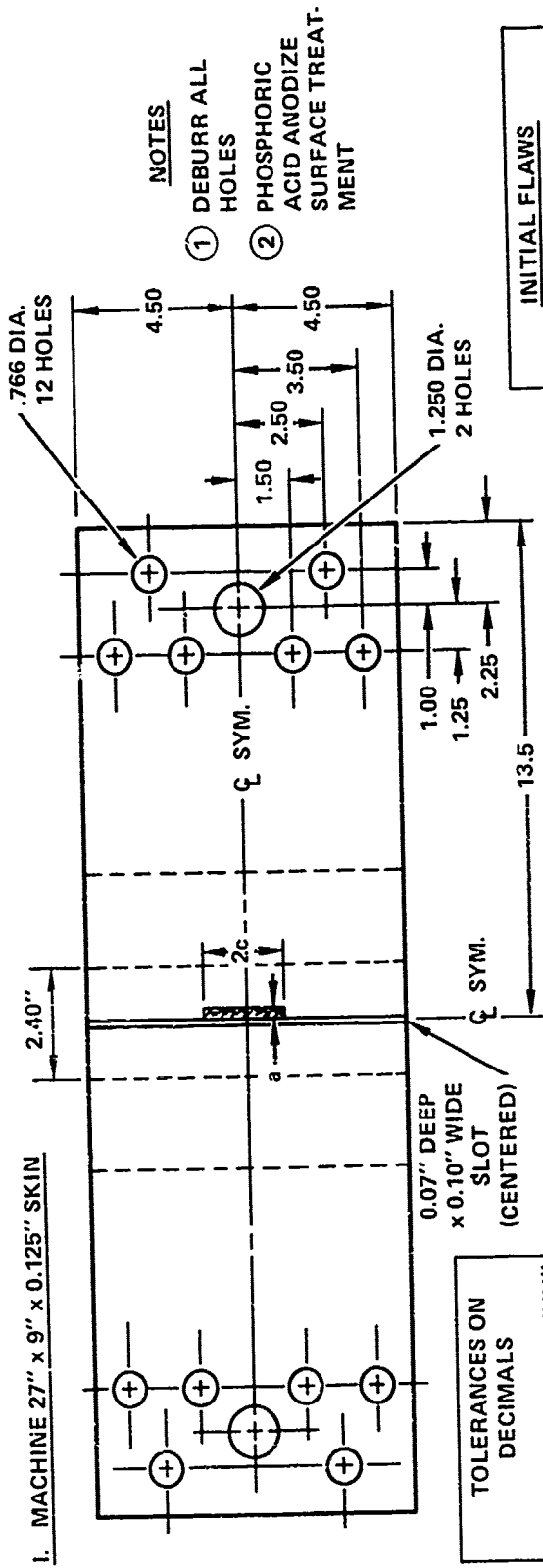


Figure 33. Compliance of SLJ specimen as computed by finite element analyses



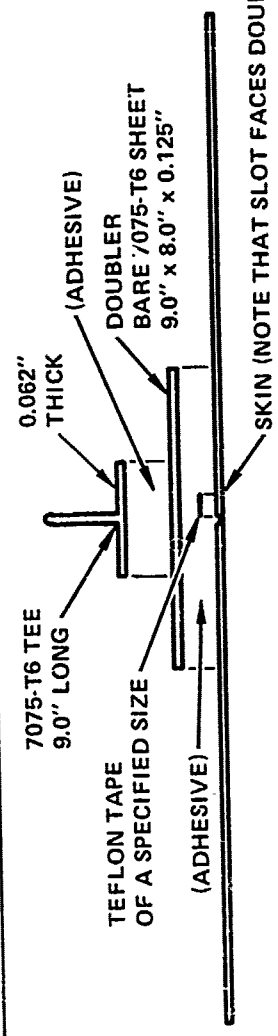
I. MACHINE 27" x 9" x 0.125" SKIN

- NOTES**
- ① DEBURR ALL HOLES
 - ② PHOSPHORIC ACID ANODIZE SURFACE TREATMENT

TOLERANCES ON DECIMALS	
.X"	.XX"
±.1"	±.03"
	.XXX"
	±.010"

INITIAL FLAWS	
SPECIMENS	a
2	0
2	0.3"
2	4.0"
	2c
	0
	9.0"
	0.5"

II. BOND WITH AF-55 WITH TEFLON-TAPE FLAWS:



III. AFTER BONDING, MACHINE SLOT THROUGH. FINAL CONFIGURATION IS A SINGLE LAP JOINT TEST SPECIMEN WITH A BONDLINE FLAW BETWEEN THE DOUBLER AND ONE SKIN MEMBER.

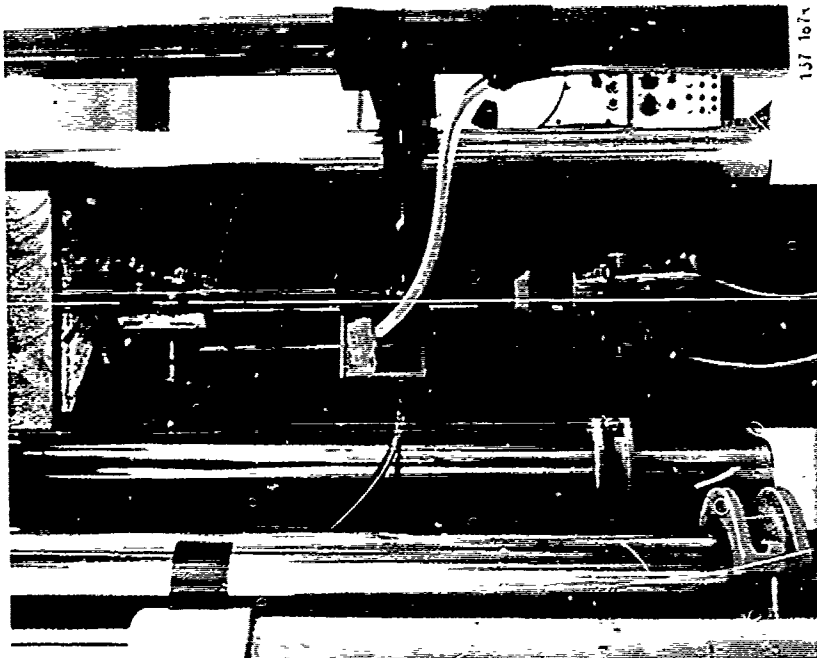
Figure 34. Single lap joint (SLJ) specimen with thin adherends

102 mm (4.0 in.). Specimens A and B contained no preflaws in the bondline; C and D each contained an across-the-width flaw extending 8 mm (0.3 in.) along the bondline from the gap of the joint; and E and F each contained a 13 mm (0.5 in.)-width flaw extending axially from the gap all the way to one edge of the doubler. Fabrication procedures of these specimens were similar to that discussed in subsection 2.1.

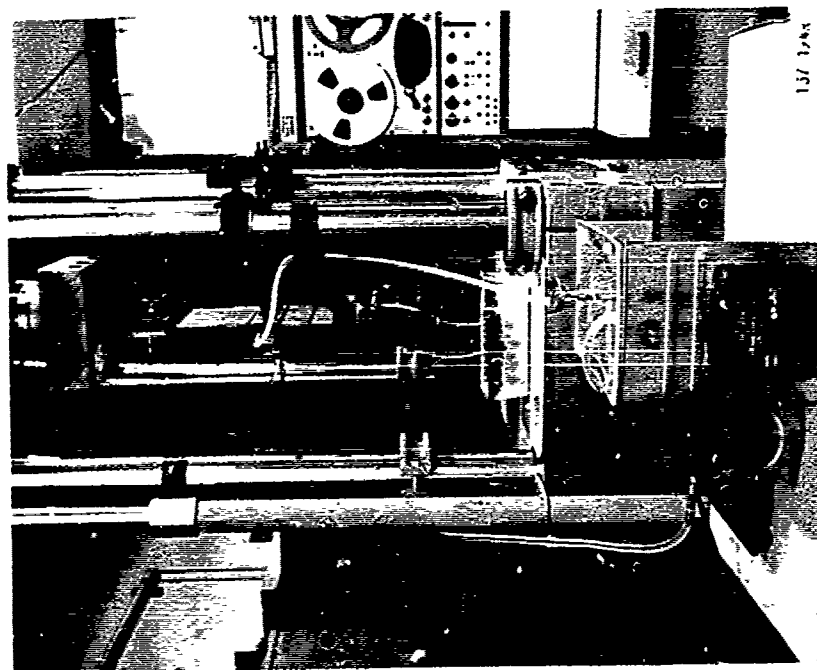
Figure 35 shows a profile view of the specimen in the 200 kip MTS machine. Axial cyclic loading was applied through rigid grip plates attached to either end of the specimen with a 31.2 mm (1.25-in.) diameter central alignment pin and six 19.2 mm (0.75-in.) bolts, tightened so that all load was introduced by friction. Lateral deflections were constrained by a pair of flex rods connecting the vertical leg of the tee to a steel channel beam that was mounted across the columns of the MTS machine.

Deionized water was pumped continuously from the thermostatically-controlled tank (bottom of Figure 35(a)) through a plexiglass box attached to the test section of the specimen. The plexiglass box was fastened directly to the specimen with water-resistant RTV silicone rubber adhesive sealant. The temperature as measured in the box (Figure 36(a)) was maintained within 1.1°K (2°F) of the required temperature. The specimen was always oriented with the preflaw on the bottom and totally immersed in the hot water.

Crack length was monitored indirectly by a compliance method. Load cycling was stopped intermittently and the water was drained from the box so that the displacement gage could be put across the gap of the joint as in Figure 36(b). The deflection for a tensile load of 49.4 kN (11.1 kip) had been calculated as a function of the crack length in the bondline by a nonlinear finite element analysis and plotted in Figure 37. The analysis assumed that the bondline crack would grow as a single, uniform across-the-width crack originating at the gap of the joint.

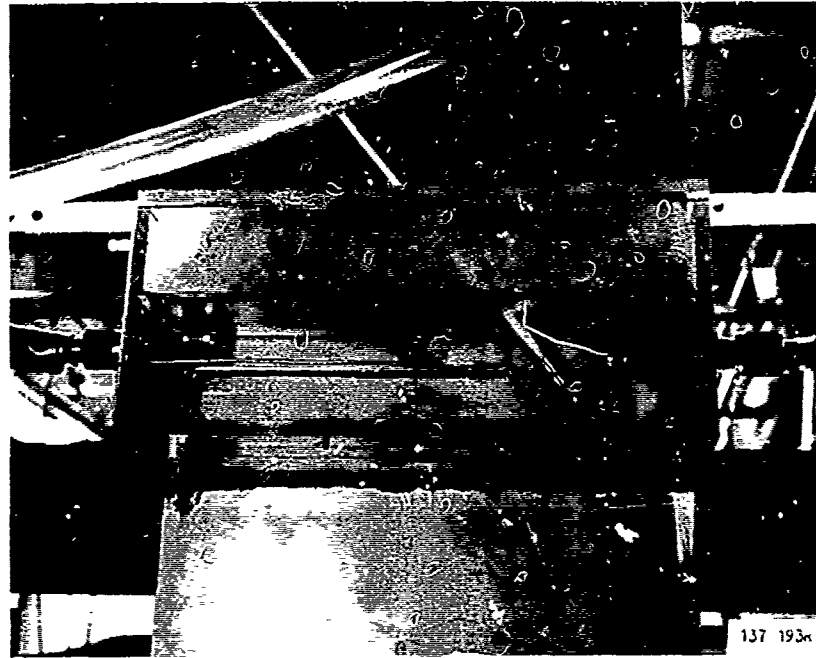


(b) Close up of specimen

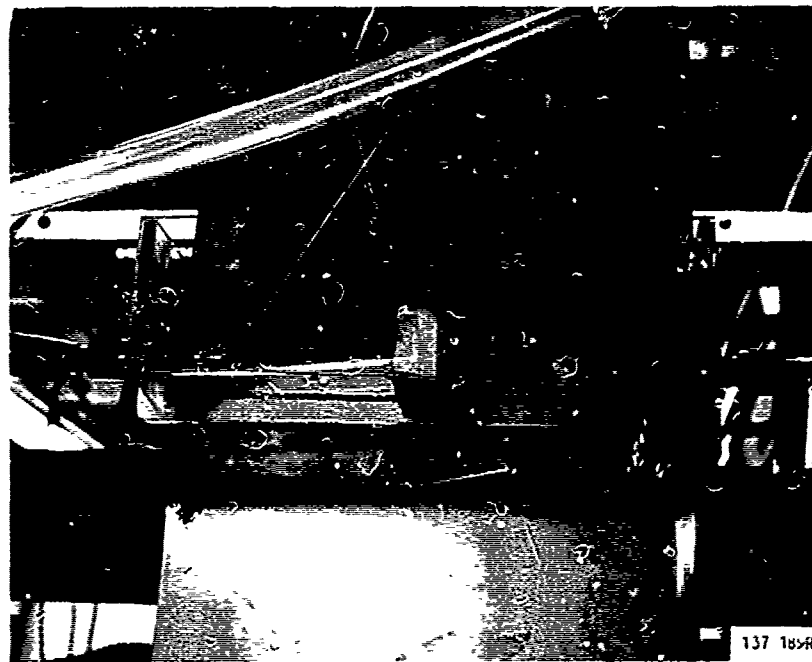


(a) Test machine, pump and tank

Figure 35. Test setup for thin-adherend SLJ specimens in hot water



(a) During fatigue cycling



(b) Stopped for measuring displacement

Figure 36. Environmental box and displacement gage

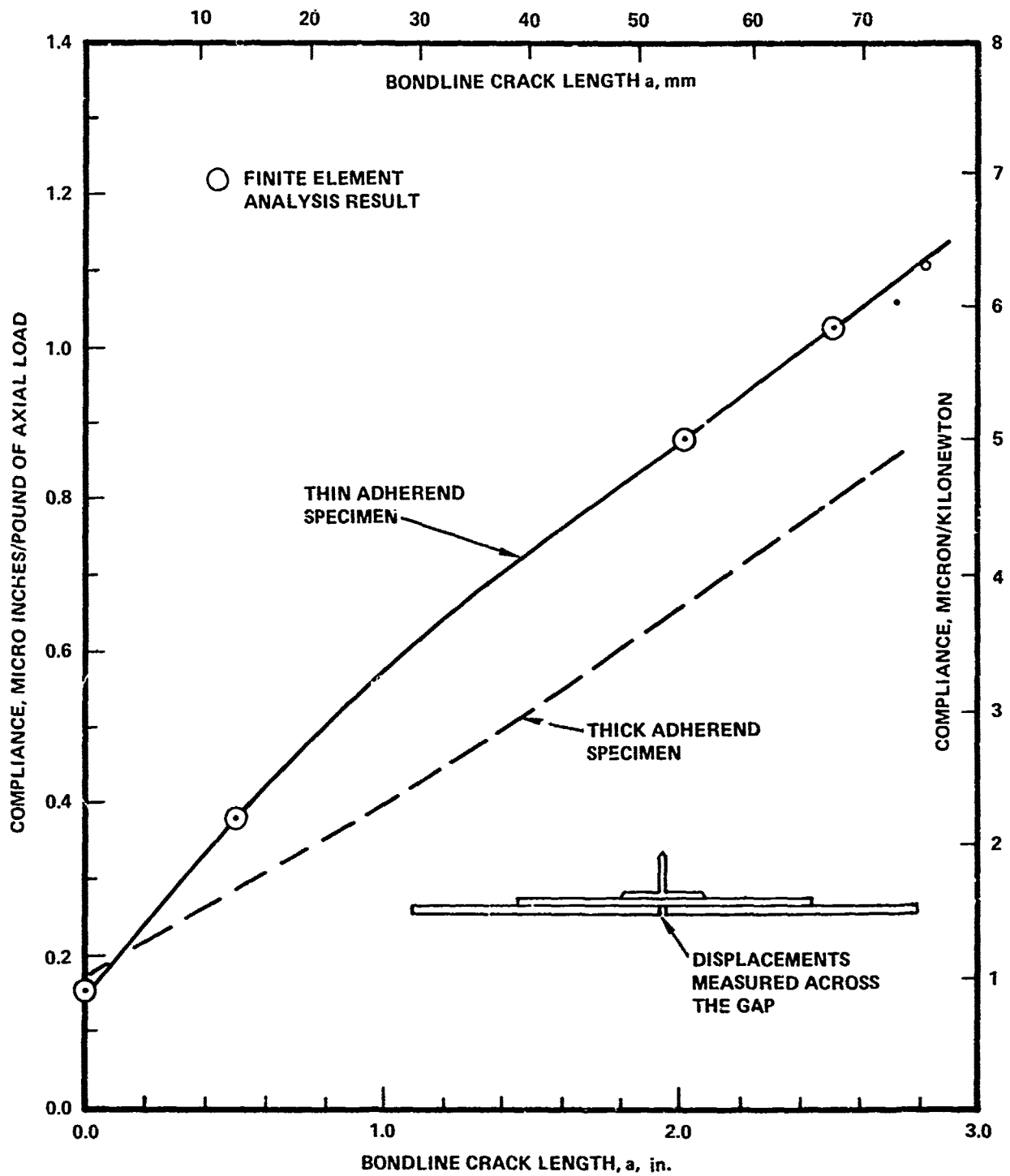


Figure 37. Compliance of thin-adherend SLJ specimen as computed by finite element method

2 ANALYSIS OF THE SINGLE LAP JOINT SPECIMENS

Analytical crack growth estimates were obtained for these tests using a linear elastic fracture mechanics (LEFM) approach. A finite element analysis was used to compute macroscopic bending and axial stresses. From these, the approximate Mode I and Mode II components of strain energy release rate and subsequently, the effective strain energy release rate, were calculated. Crack growth in the adhesive layer was then estimated using baseline fatigue crack growth data for the adhesive. Analysis results for the thick adherend and the thin adherend single lap joint specimens are presented separately.

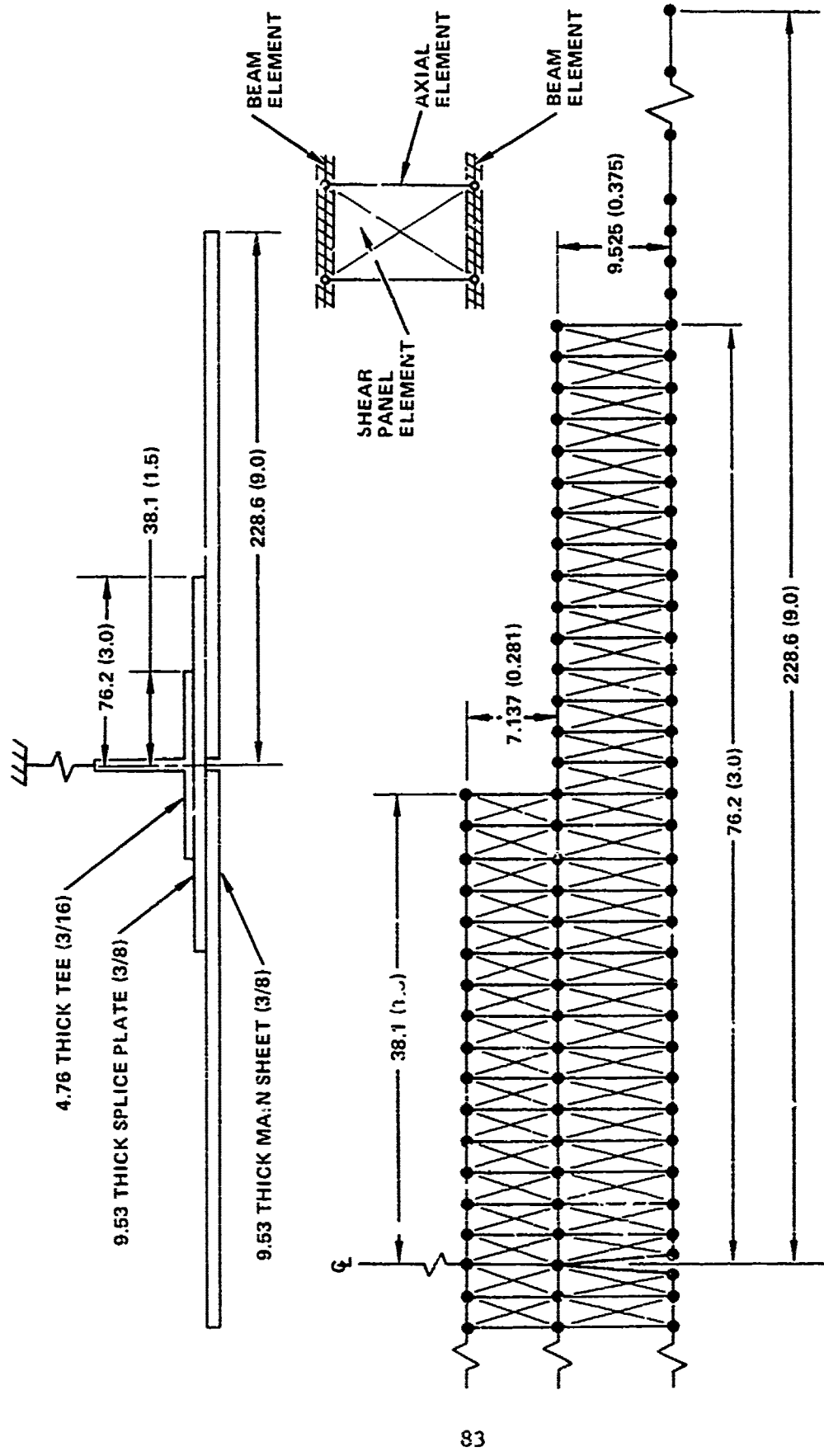
A finite element analysis of both SLJ specimen geometries was conducted for two reasons. One was to compute the distribution of bending and axial stresses, which provided a basis for estimating \mathcal{G}_I and \mathcal{G}_{II} , the Mode I and II components of the strain energy release rate. The second was to calculate the compliance for various bondline crack lengths, which was used to estimate crack lengths in the tests as discussed before.

The predicted crack growth rates were calculated from crack-tip bending moments using the following procedure:

- At a given debond length, the Mode I strain energy release rate, \mathcal{G}_I , was computed from the bending moment.
- The Mode II strain energy release rate, \mathcal{G}_{II} , for the test specimen was assumed to be equal to the value of \mathcal{G}_{II} induced in a cracked lap shear (CLS) specimen of the same adherends and subjected to the same amount of axial load and bending moment.
- Values of $\Delta\mathcal{G}_I$ and \mathcal{G}_{II} for the single-lap-joint specimen were used to obtain the effective strain energy release rate, $\Delta\mathcal{G}_{eff}$, from Equation (36), Section III.
- The predicted crack growth rates were calculated using appropriate baseline data, as shown in Figure 30 with $\Delta\mathcal{G}_{eff}$ replacing $\Delta\mathcal{G}_I$.

2.1 Thick Adherend Specimens

The finite element model of the thick adherend specimen is depicted in Figure 38. Very simple modeling was used. The adherends (tee, splice plate, and skin) were modeled as one dimensional axial and beam members, located in the midplane of each structural member. Axial and shear members were used to



NOTE: ALL DIMENSIONS ARE IN MILLIMETERS WITH CORRESPONDING INCH VALUES GIVEN IN PARENTHESES.

Figure 38. Finite element model of the profile section of the test specimen

model the normal and shear capability of the adhesive. The axial member modeling the lateral constraint contained the proper stiffness of the actual lateral support fixtures used in tests.

Calculations of bending and axial stresses in the adherends and displacement at the gap of the joint were done at a sequence of crack lengths. The crack was simulated by disconnecting axial and shear members representing the adhesive.

Equation (17) of Section II was used to estimate \mathcal{S}_I for the thick-adherend test specimens at the maximum applied load, using the computed values of bending moment induced in the splice plate. As shown in Figure 39, the bending moments in the splice plate are fairly uniform until the crack length reaches 38 mm (1.5 in.). At this point the crack tip is located just below the edge of the tee, and the abrupt change in stiffness appears to drastically affect the moment distribution. For larger crack lengths the moment distribution is nonuniform, but the portion of the distribution between the crack tip and the edge of the tee is approximately uniform and was used in Eq. (17) for the computation of \mathcal{S}_I . To indicate the likely error due to nonuniformity of bending moment, two estimates of \mathcal{S}_I were made, one using the average bending moment, the other the peak bending moment at the crack tip. These estimates are plotted in Figure 40.

Initially, it was felt that \mathcal{S}_I might be influenced by the finite length of the doubler. A correction factor was provided by the solution to the problem shown in Figure 41, a finite length, double-cantilever beam subjected to uniform bending. For the bonded single lap joint tested specimen, interest is limited to values of $H/(H+l)$ less than 0.4. In this range, it is clear from Figure 41 that no correction factor for finite length is needed.

The \mathcal{S}_{II} component of the SLJ specimen was estimated by analogy with the CLS Specimen. It consisted of two parts. The first part is induced by the bending moment and can be estimated using Equation (17) of Section II. The second part is the direct result of the axial load and can be estimated by subtracting \mathcal{S}_I (Equation (18)) from \mathcal{S} (Equation (5)). Combining these two parts, the value of \mathcal{S}_{II} is estimated by the equation

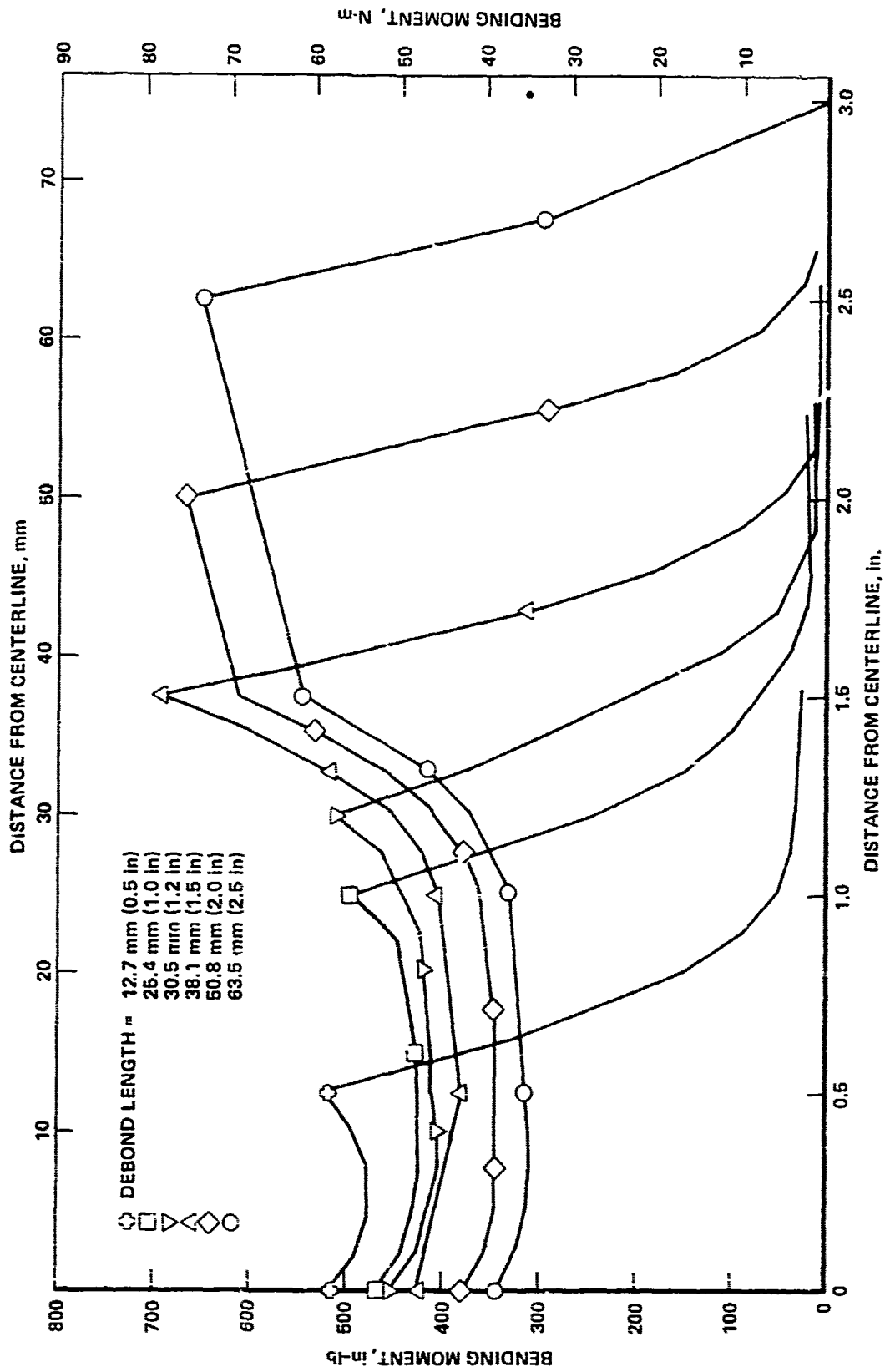


Figure 39. Distributions of bending moment in the splice plate

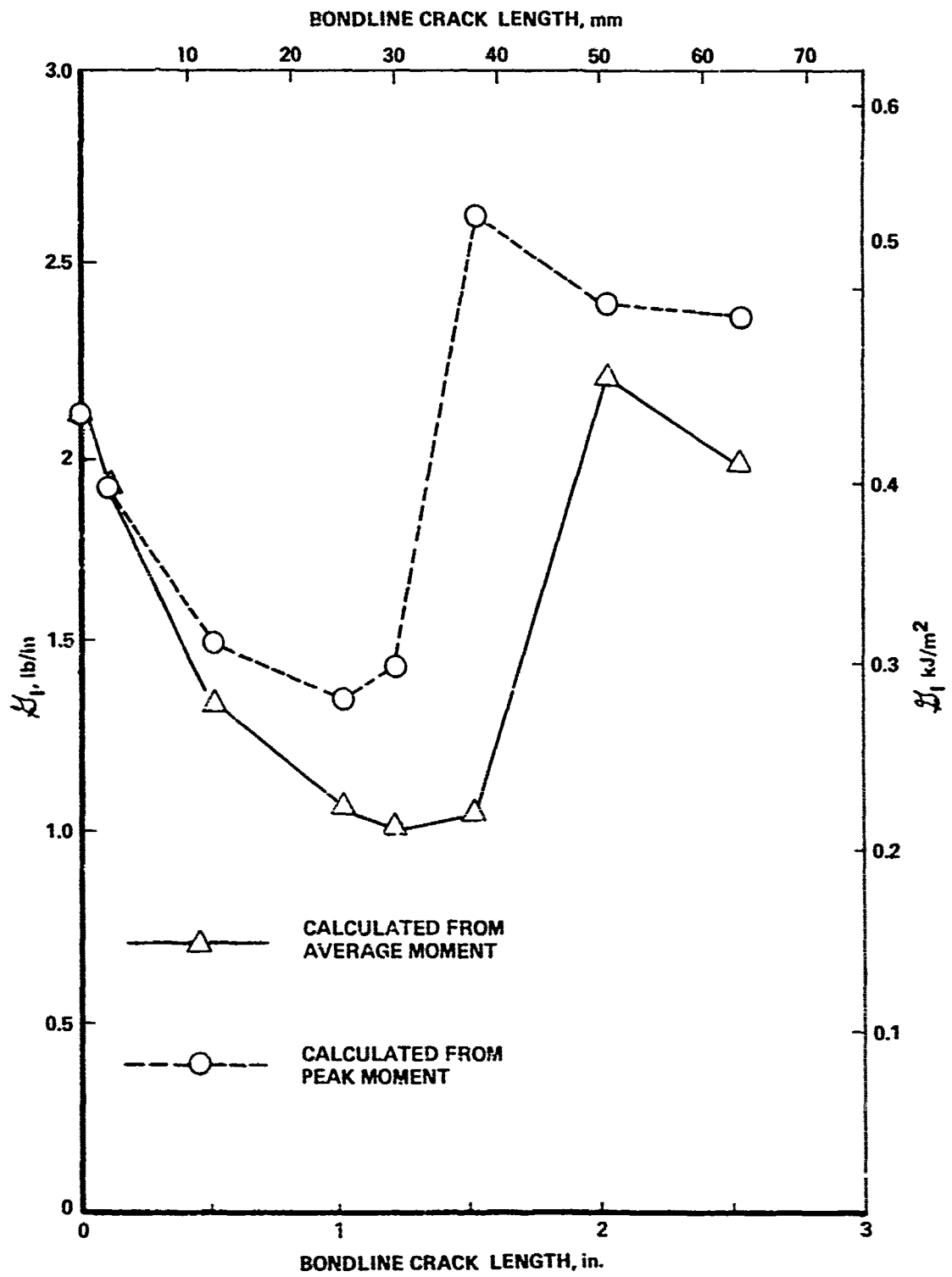


Figure 40. Calculated strain energy release rates at various bondline crack lengths

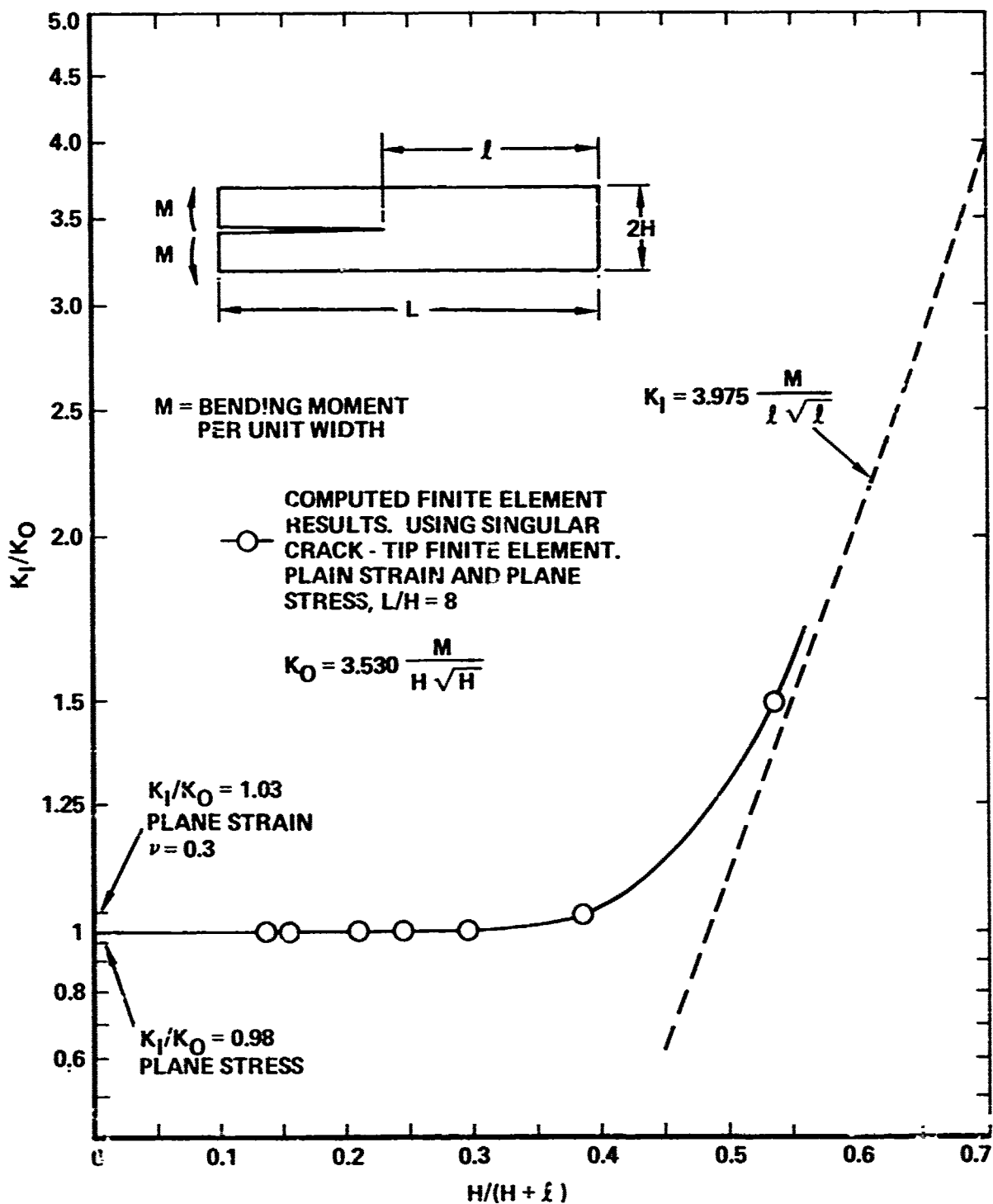


Figure 41. Finite length correction factor for a split beam subjected to uniform bending

$$\mathcal{G}_{II} = \frac{\sigma_2^2 t_2}{2E} \left(1 - \frac{t_2}{t_0}\right) \left[1 - \frac{3t_2}{t_0} \left(1 - \frac{t_2}{t_0}\right) \frac{1 - \sqrt{EI_2/EI_0}}{1 + \sqrt{EI_2/EI_0}}\right] \quad (38)$$

Here the subscripts 0 and 2 refer to the thick and thin ends of the CLS specimen, respectively. By analogy, 2 refers to the splice plate and 0 refers to the skin/splice plate laminate. σ_2 is the average axial stress in the splice plate and is defined as $P/t_2 b$.

The fatigue data shown in Figure 29 of Section III show that the effect of Mode II loading can be accounted for by the use of effective strain energy release rate $\Delta\mathcal{G}_{eff}$ in place of $\Delta\mathcal{G}_I$. Values of the estimated $\Delta\mathcal{G}_I$, ratios of $\mathcal{G}_{II}/(\mathcal{G}_I + \mathcal{G}_{II})$, $\Delta\mathcal{G}_{eff}$, and the crack growth rates are tabulated in Table 5. Comparisons of analytical estimates and test results are discussed in subsection 4.

2.2 Thin-Adherend Specimens

The thin-adherend, single-lap-joint specimen was analyzed using the same analysis procedure as for the thick adherend specimen. Two-dimensional geometrically nonlinear finite element analyses were conducted for this specimen at 4 debond lengths: $a = 0$ (the undamaged configuration) and $a = 13, 51,$ and 64 mm (0.5, 2.0, and 2.5 in.). The finite element analyses were conducted for two purposes. One was to calculate the compliance for various bondline crack lengths, which will be used to estimate crack lengths during testing. The second was to provide the distribution of bending moment in the doubler, which provides a basis for estimating the Mode I and Mode II strain energy release rates, \mathcal{G}_I and \mathcal{G}_{II} . The estimated \mathcal{G}_I and \mathcal{G}_{II} values were used to provide crack growth predictions, prior to testing these specimens, as a further demonstration of the applicability of fracture mechanics methodology to bondline failure.

The dashed line in Figure 37 is the compliance curve for this specimen subjected to an applied axial skin stress of 69 MPa (10 ksi). Compared to similar results for the thick-adherend specimen, the thin-adherend specimen is more flexible, except possibly when the specimen is undamaged.

TABLE 5. ESTIMATED EFFECTIVE STRAIN ENERGY RELEASE RATES AND CRACK GROWTH RATES, THICK ADHEREND SLJ SPECIMEN

Debond Length mm (in.)	$\Delta \mathcal{E}_I$ kJ/m ² (lb/in)	$\mathcal{E}_{II} / \mathcal{E}_I$	$\Delta \mathcal{E}_{eff}$ kJ/m ² (lb/in)	mm/cycle	da/dN (in/cycle)
(a) ESTIMATIONS BASED ON MAXIMUM BENDING MOMENTS					
0.0	0.375 (2.14)	0.50	0.749 (4.28)	5.56 x 10 ⁻³	(2.19 x 10 ⁻⁴)
2.5 (0.1)	0.338 (1.93)	0.52	0.690 (3.94)	3.52 x 10 ⁻³	(1.39 x 10 ⁻⁴)
12.7 (0.5)	0.263 (1.50)	0.55	0.552 (3.15)	1.02 x 10 ⁻³	(4.02 x 10 ⁻⁵)
25.4 (1.0)	0.240 (1.37)	0.53	0.494 (2.82)	0.55 x 10 ⁻³	(2.17 x 10 ⁻⁵)
30.5 (1.2)	0.256 (1.46)	0.55	0.538 (3.07)	0.88 x 10 ⁻³	(3.46 x 10 ⁻⁵)
38.1 (1.5)	0.464 (2.65)	0.50	0.928 (5.30)	18.34 x 10 ⁻³	(7.22 x 10 ⁻⁴)
50.8 (2.0)	0.424 (2.42)	0.48	0.830 (4.74)	9.85 x 10 ⁻³	(3.88 x 10 ⁻⁴)
63.5 (2.5)	0.418 (2.39)	0.48	0.819 (4.68)	9.14 x 10 ⁻³	(3.60 x 10 ⁻⁴)
(b) ESTIMATIONS BASED ON AVERAGE BENDING MOMENTS					
0.0	0.375 (2.14)	0.50	0.749 (4.28)	5.56 x 10 ⁻³	(2.19 x 10 ⁻⁴)
2.5 (0.1)	0.338 (1.93)	0.52	0.690 (3.94)	3.52 x 10 ⁻³	(1.39 x 10 ⁻⁴)
12.7 (0.5)	0.236 (1.35)	0.56	0.501 (2.86)	0.59 x 10 ⁻³	(2.32 x 10 ⁻⁵)
25.4 (1.0)	0.193 (1.10)	0.58	0.417 (2.38)	0.21 x 10 ⁻³	(8.27 x 10 ⁻⁶)
30.5 (1.2)	0.180 (1.03)	0.59	0.394 (2.25)	0.16 x 10 ⁻³	(6.30 x 10 ⁻⁶)
38.1 (1.5)	0.187 (1.07)	0.57	0.401 (2.29)	0.17 x 10 ⁻³	(6.09 x 10 ⁻⁶)
50.8 (2.0)	0.392 (2.24)	0.48	0.769 (4.39)	6.44 x 10 ⁻³	(2.54 x 10 ⁻⁴)
63.5 (2.5)	0.348 (1.99)	0.49	0.690 (3.94)	3.52 x 10 ⁻³	(1.39 x 10 ⁻⁴)

The estimated distributions of the bending moment in the doubler for a stress of 69 MPa (10 ksi) are shown in Figure 42. For the three debond lengths analyzed, the moment varies gradually throughout the entire debond region. The approach of using average bending moment values in calculating strain energy release rates thus becomes more difficult to justify. On the other hand, the alternative approach of using the bending moment at the crack tip (usually the maximum value) is still reasonable. For this specimen, the predicted crack growth rates were calculated from the maximum crack-tip bending moments only.

One purpose of the finite element analysis was to select a stress level sufficient to induce crack growth in the adhesive layer. Because of geometric nonlinearity the finite element analysis had to be rerun at several stress levels each for a set of debond conditions. The estimation of strain energy release rates and prediction of crack growth rates were made using the results of these analyses and following the same procedure as described for the analysis of the thick adherend single-lap-joint specimen. The estimated strain energy release rates and crack growth rates at two stress levels and 5 debond lengths are shown in Table 6. Note that the effective strain energy release rates shown are calculated from Equation (37), which include the influence of \mathcal{G}_{II} . The estimated crack growth rates, also shown in Figure 43, are obtained from the baseline data in Figure 30 for 333°K (140°F) water immersion at 3 Hz.

It can be seen from Figure 43 that the predicted crack growth rates decrease drastically as debond length increases. The predicted rate decreases almost to its minimum value at a debond length of 31 mm (1.2 in.). The higher applied load level of 172.38 MPa provides more desirable overall crack growth rates and a more reasonable test duration, but the peak stress (tension plus bending) is quite high, about 85 percent of the tensile yield strength of the adherend. Therefore, a slightly lower applied stress level of 165.48 MPa (24 ksi) was selected as the test load for the thin-adherend specimens. Analytical results were interpolated to provide necessary life prediction at this intermediate load level.

The selected load for these tests is identical to that used for the thick adherend single-lap-joint specimens tested earlier. The thick adherend tests had basically the same configuration and lateral support, but the

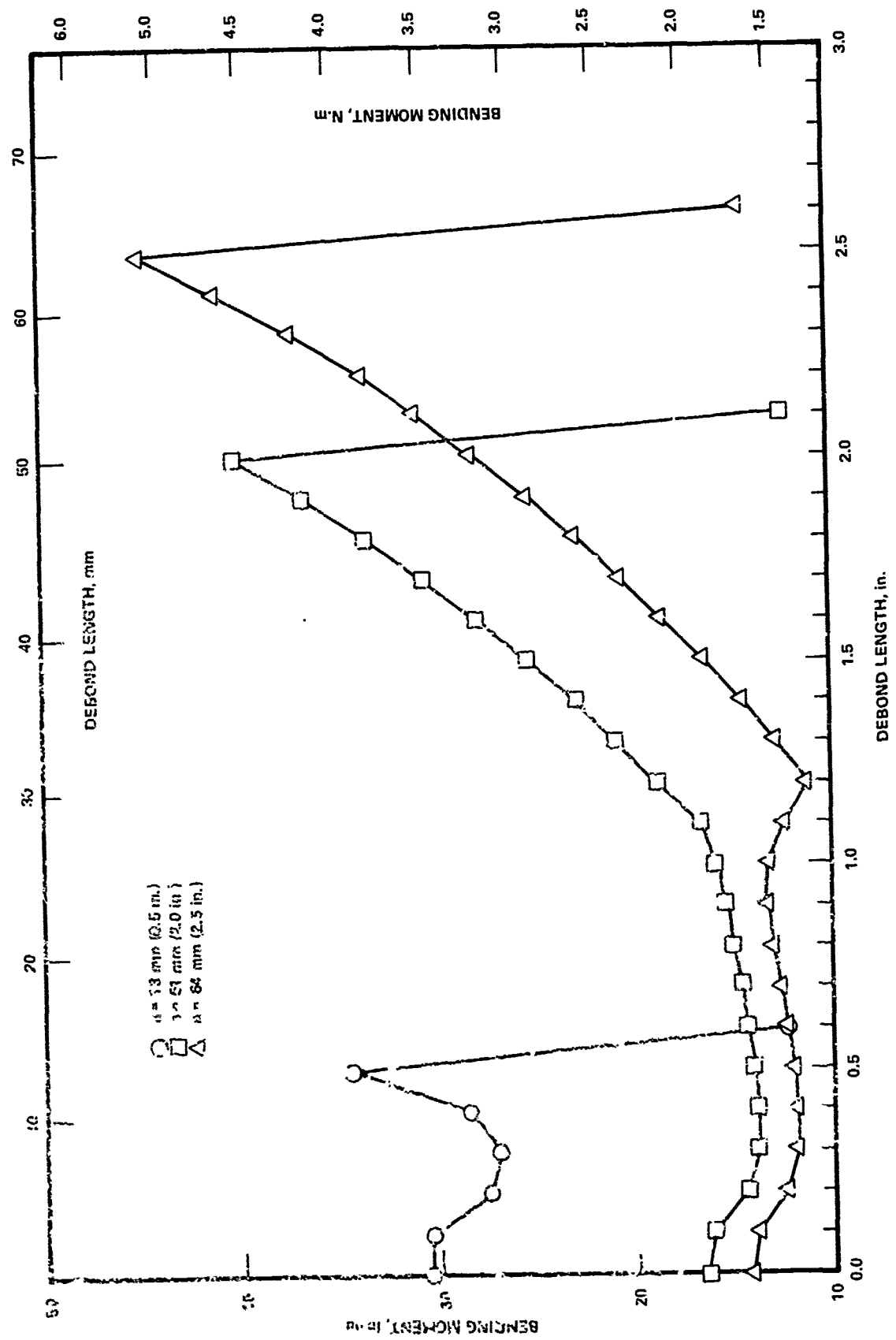


Figure 42. Bending moment distributions for thin-adherend SLJ specimen

TABLE 6. ESTIMATED EFFECTIVE STRAIN ENERGY RELEASE RATES AND CRACK GROWTH RATES, THIN ADHEREND SLJ SPECIMENS

(a) Applied Axial Skin Stress = 25 ksi

Debond Length	$\Delta \mathcal{G}_I$	$\mathcal{G}_{II} / \mathcal{G}$	$\Delta \mathcal{G}_{eff}$	da/dN	
	kJ/m^2 (lb/in)		kJ/m^2 (lb/in)	$\mu\text{m/cycle}$ ($\mu\text{in/cycle}$)	$\mu\text{in/cycle}$
0.0	0.298 (1.70)	0.59	0.650 (3.71)	31.34	(1233.86)
12.7 (0.5)	0.128 (0.73)	0.70	0.306 (1.75)	0.62	(24.41)
38.1 (1.5)	0.117 (0.67)	0.71	0.284 (1.62)	0.42	(16.54)
50.8 (2.0)	0.151 (0.86)	0.68	0.355 (2.03)	1.34	(52.76)
63.5 (2.5)	0.208 (1.19)	0.63	0.471 (2.69)	5.85	(230.31)

(b) Applied Axial Skin Stress = 20 ksi

Debond Length	$\Delta \mathcal{G}_I$	$\mathcal{G}_{II} / \mathcal{G}$	$\Delta \mathcal{G}_{eff}$	da/dN	
	kJ/m^2 (lb/in)		kJ/m^2 (lb/in)	$\mu\text{m/cycle}$ ($\mu\text{in/cycle}$)	$\mu\text{in/cycle}$
0.0	0.226 (1.29)	0.57	0.483 (2.76)	6.674	(262.76)
12.7 (0.5)	0.096 (0.55)	0.68	0.228 (1.30)	0.134	(5.28)
38.1 (1.5)	0.092 (0.53)	0.68	0.219 (1.25)	0.109	(4.29)
50.8 (2.0)	0.118 (0.67)	0.65	0.270 (1.54)	0.323	(12.72)
63.5 (2.5)	0.163 (0.93)	0.61	0.361 (2.06)	1.465	(57.68)

adherends were three times as thick and the test environment was much milder, i.e., laboratory air instead of 333°K (140°F) water.

The test lives of the thick adherend specimens ranged from 22,000 to 44,000 cycles. Using a fracture mechanics analysis, a longer life (118,000 cycles) was predicted for thinner specimens subjected to identical fatigue loads (thus, much higher adherend stresses) and a harsher environment. Comparisons between the estimated lives and test data are discussed in subsection 4.

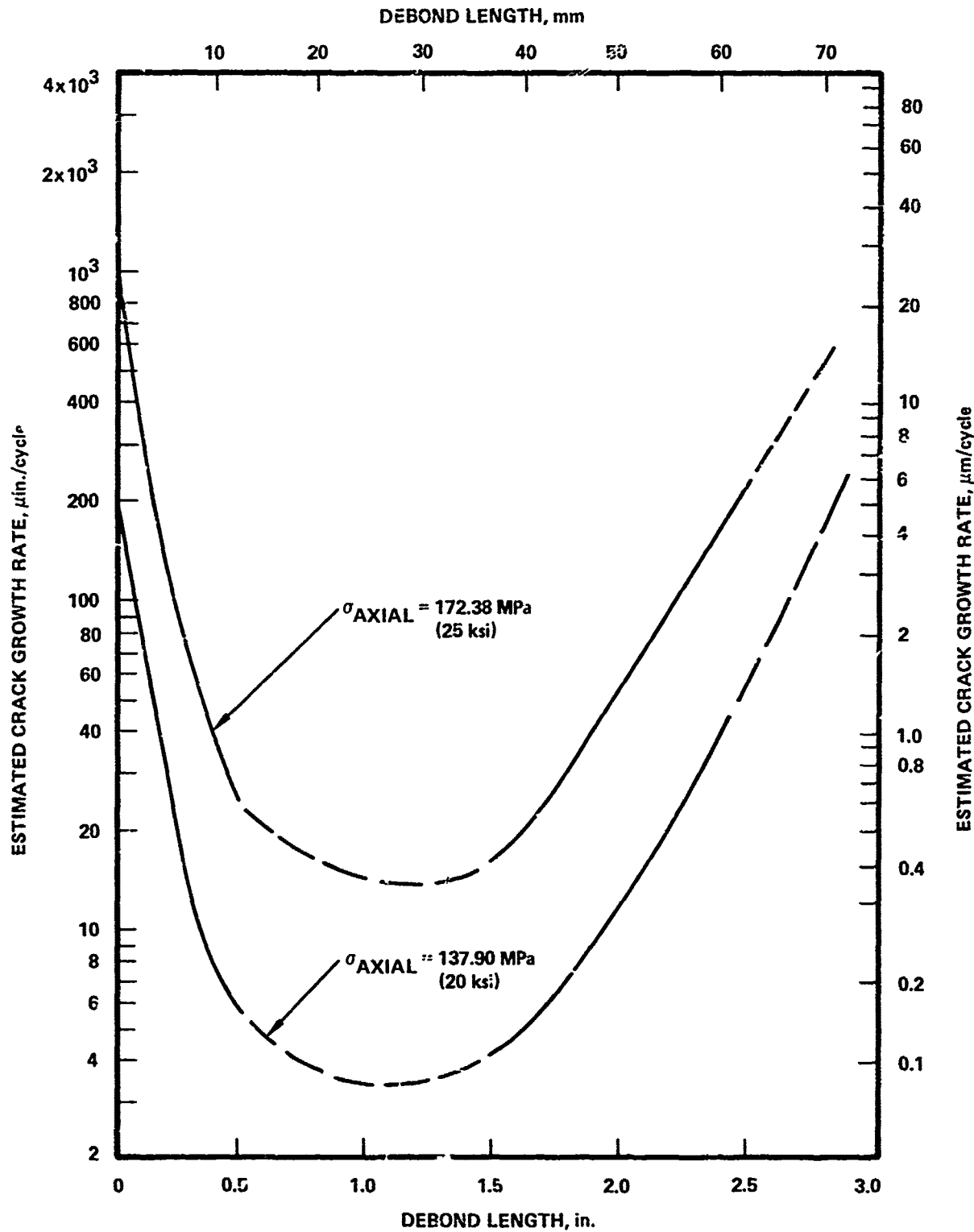


Figure 43. Estimated crack growth rates at two applied stress levels

3 TEST RESULTS AND DISCUSSIONS

3.1 Thick-Adherend Specimens

Figure 44 shows the total test lives for the six thick adherend specimens. The specimens with initial flaws failed earlier than the unflawed specimens. There does not seem to be a significant difference between specimens with across-the-width initial flaws and those with centered flaws only 51 mm (2 inches) wide. The latter flaws grew sideways very rapidly so as to become across-the-width flaws, as determined from ultrasonic measurements.

Scatter was low except for specimens SLJ-5 and SLJ-6, duplicates for which the lives differed by a factor of 1.8. Variations by factors of 1.8 are present throughout the baseline fatigue data given in Figures 27 through 31 of Section III. The scatter should be expected to exceed that of metal fatigue because, as discussed in Section III, the slopes of the fatigue crack growth rate (da/dN) curves for structural adhesives are extremely steep compared to those for metals. One consequence of this steepness of slope is a greater sensitivity of da/dN to small variations in stress or strength. Using $n = 5.57$ in Equation (34), one finds that a 5.4 percent difference in the ratio of the applied stress to the crack growth resistance would cause the factor of 1.8 difference in crack growth lives observed for specimens SLJ-5 and -6.

Figures 45(a) through 45(e) show the crack-length-versus-cycles data for all but the first specimen tested, SLJ-4 (for which just one data point was obtained, $a = 25$ mm (1.0 in.) at $N = 25,000$ cycles by the ultrasonic method). Debond length by the ultrasonic technique is defined as the debond area divided by specimen width. Since many of the flaws grew as uniform across-the-width flaws, this is in general an adequate definition. However, in Specimen SLJ-1 (initially unflawed) the debond flaw initiated at one corner and tended to grow faster along one edge than the other. Hence the area-to-width ratio definition of debond length may have tended to underestimate the true severity of the flaw. This would account for the poor correlation between ultrasonic and compliance-measured crack sizes for this specimen shown in Figure 45(a). For SLJ-2 and SLJ-5 the agreement was much better.

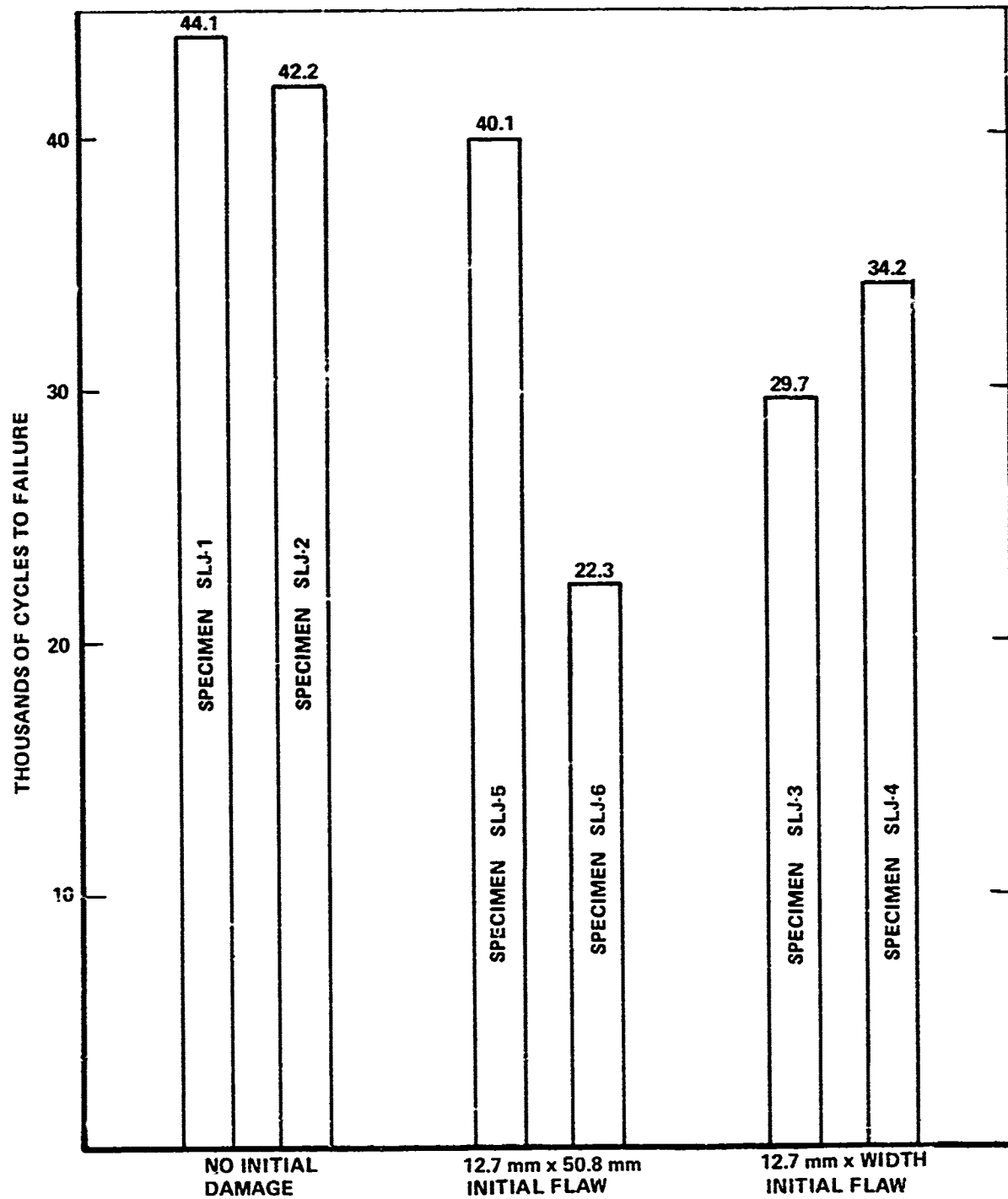
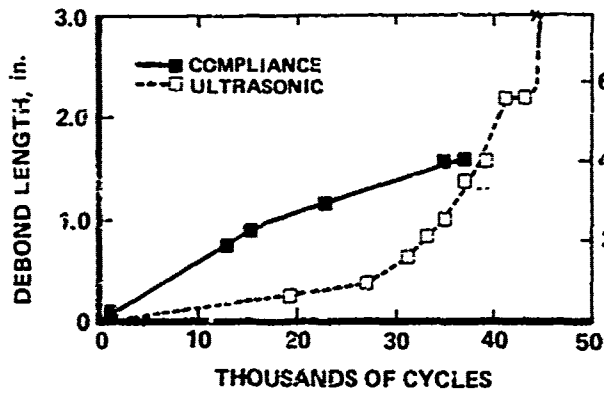
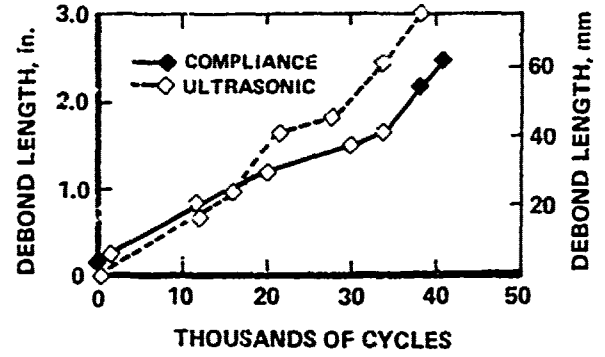


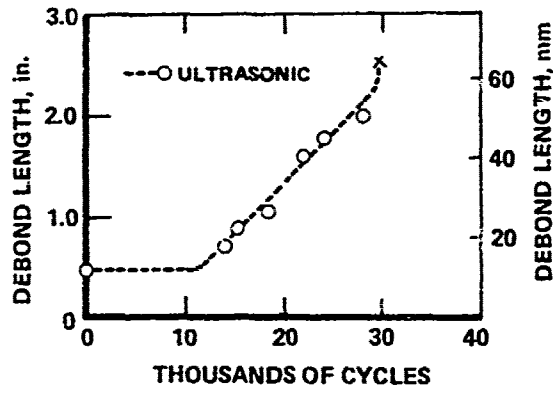
Figure 44. Total lives of SLJ specimens with or without initial bondline flaws



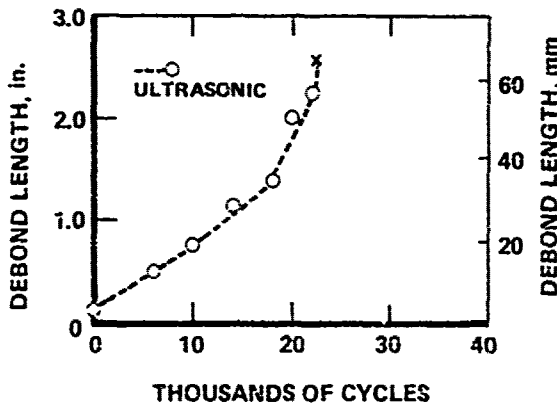
(a) SPECIMEN SLJ-1



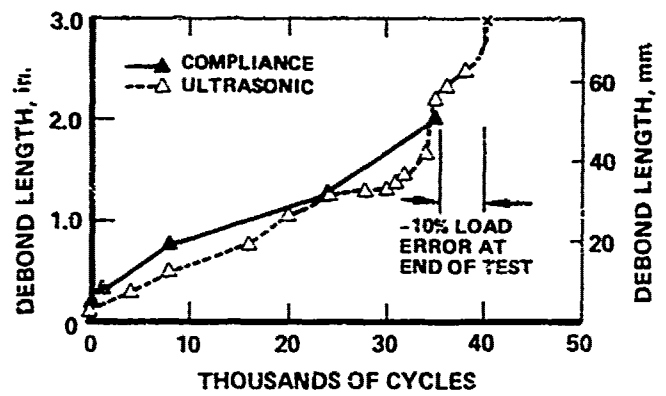
(b) SPECIMEN SLJ-2



(c) SPECIMEN SLJ-3



(d) SPECIMEN SLJ-6



(e) SPECIMEN SLJ-5

Figure 45. Bendline crack growth histories

Figure 46 shows a summary of crack growth rates for all six specimens as a function of crack size. The crack sizes and rates shown are as determined by both the ultrasonic measurements and the compliance measurements. The magnitude of scatter for the compliance measurement method is smaller than for the ultrasonic method, and the compliance method is less expensive to use in the laboratory. However, the information on flaw shape and location which was obtained ultrasonically cannot be obtained by the compliance method.

Growth rates of the bondline flaws in the test specimens were estimated from Figure 27; however, $\Delta \mathcal{S}_{\text{eff}}$ defined in Equation (37) was used in place of $\Delta \mathcal{S}_I$. The resulting crack growth rate estimates are compared to the empirical data in Figure 47. Two sets of estimates are shown; one based on the average bending moments and one based on the maximum moments. Of these, the rates estimated using maximum bending moment tended to agree more closely with the actual rates.

3.2 Thin-Adherend Specimens

Test results for the six thin adherend specimens fatigue tested in 333°K (140°F) water are summarized in Table 7. Specimen B, with no bondline preflow, failed in the bondline at 48,297 cycles. In Specimen C, significant growth of the bondline crack was measured but the final failure occurred in the skin at 53,976 cycles, right at the stress concentration at the end of the doubler. At least one fatigue crack origin could be clearly identified when the fracture surface of the failed skin member was visually examined.

To reduce this stress concentration the edges of the doubler were beveled on Specimens A, D, and F. Specimen D failed at 57,227 cycles due to fatigue failure of the doubler. However, extensive adhesive cracking was evident from compliance measurements. Specimen F and Specimen A both failed in the bondline at 58,338 and 57,398 cycles, respectively. No anomalies were observed for these two specimens.

Specimen E had a longitudinal flaw in the bondline but failed in the doubler across the split line after only 8599 cycles. The doubler failure was expected in this specimen because the split line had been machined too deep,

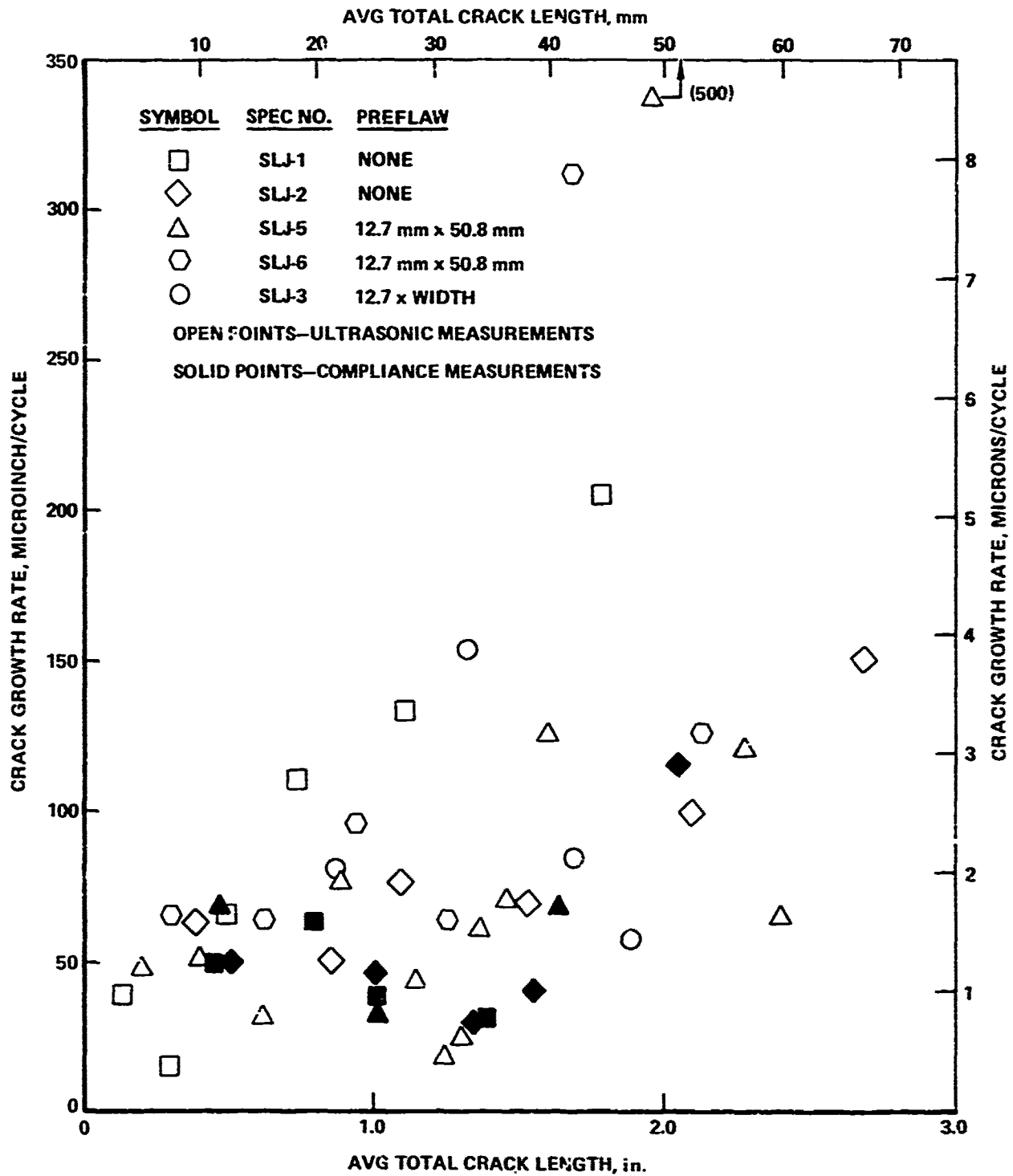


Figure 46. Crack growth rate by ultrasonic and compliance measurements

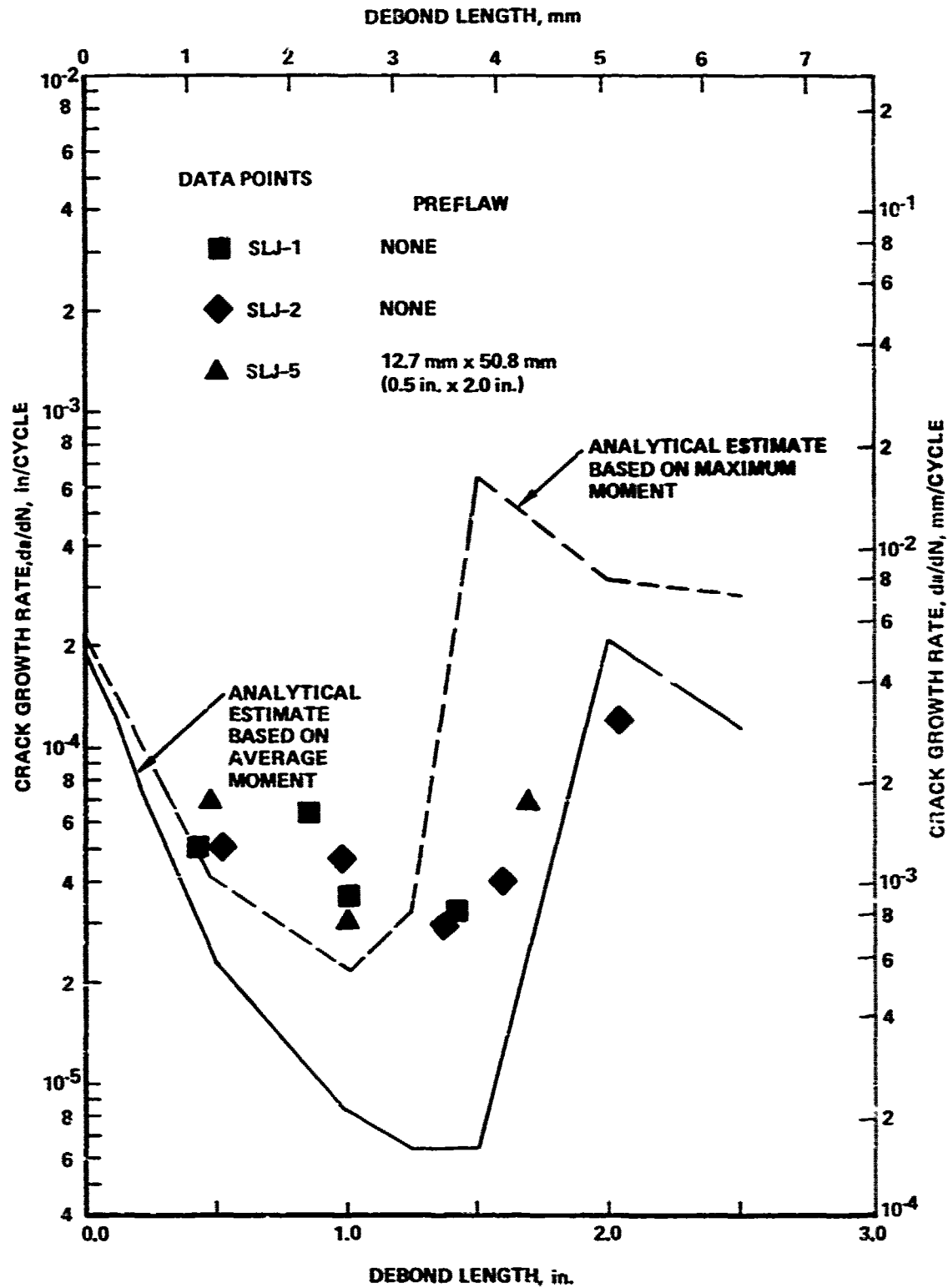


Figure 47. Estimated and empirical crack growth rates

TABLE 7. TEST LIVES, THIN-ADHEREND SINGLE-LAP JOINT

Specimen ID	Initial Flaw Condition	Failure Description
A (6)* B (1)	Unflawed	At 57,398 cycles. Failure in adhesive. At 48,297 cycles. Grip hole partially cracked at about 40,000 cycles. Failure in adhesive layer.
C (2) D (4)	7.6 mm (0.3 in.) across-the-width flaw (one side only)	At 53,976 cycles. Failure in skin after extensive debonding. At 57,227 cycles. Failure in doubler after extensive debonding.
E (3) F (5)	12.7 mm (0.5 in.) longitudinal flaw extends through the overlap region (one side only)	At 8,599 cycles. Failure in doubler due to known machining defect. At 58,338 cycles. Failure in adhesive layer.

* Numbers in parentheses indicate order of testing.

damaging the doubler at the edge of the specimen. It had been hoped, however, that the specimen would last longer than it did and thus provide more data on flaw growth in the bondline. No fatigue crack origins could be visually identified. However, approximately 50 to 75 mm (2 to 3 in.) of fracture surface (beginning at one edge of the specimen where machining damage occurred) was found to exhibit the typical flat appearance of metal fatigue cracking.

These specimens were very similar in their configuration to the thick-adherend single-lap joints tested earlier, and the test fixturing used was identical. Also, the identical magnitude of applied load per unit width was used. This means that the nominal tensile stress in the metal was increased by a factor of 3.0 by virtue of reducing the adherend thickness to one-third its prior value. Furthermore, the hot water environment is much more detrimental than laboratory air. Therefore, on a superficial examination one would expect shorter lives in the thin-adherend specimen. However, analysis prior

to testing indicated a lower reduced bending moment in the thin-adherend specimen to such an extent that the lives predicted by a fracture mechanics analysis would be longer. These predictions are supported by the fact that all the thin-adherend specimens (except Specimen E) had longer test lives than any of the six thick-adherend specimens tested earlier.

The exposed adhesive was visually examined after failure of Specimen A, B and F. It was possible to identify and separate the fatigue cracks and the static fracture, since the fracture appearances on the exposed adhesive layer are distinctively different. In addition, ultrasonic examinations were conducted of all failed specimens. It is reasonable to assume that all hidden bondline cracks were fatigue induced, not statically induced during the failure elsewhere in the specimen. Figures 48 to 53 show the extent of adhesive fatigue cracking detected visually and ultrasonically. The following can be observed:

- All specimens except Specimen E had more than one bondline crack at the time of failure.
- The reproducibility of the final adhesive crack configuration was extremely good for duplicate specimens with identical initial flaws.
- Crack front shapes of the final bondline cracks indicate that growth was most rapid along the free edges of the specimens. In Specimen F growth was most rapid adjacent to the longitudinal strip of teflon tape.

Figure 54 shows the bondline crack growth histories of all the specimens except Specimen E. The crack length shown is an apparent length as measured indirectly by the compliance method. In the compliance method the measured opening displacement of the gap of the joint is correlated to an apparent bondline crack size using the results from finite element analyses of the specimen with an across-the-width bondline crack of some selected length extending from one side of the gap of the joint.

The early apparent flaw growth rates of the unflawed specimens A and B were significantly faster than those of the specimens with initial flaws. The

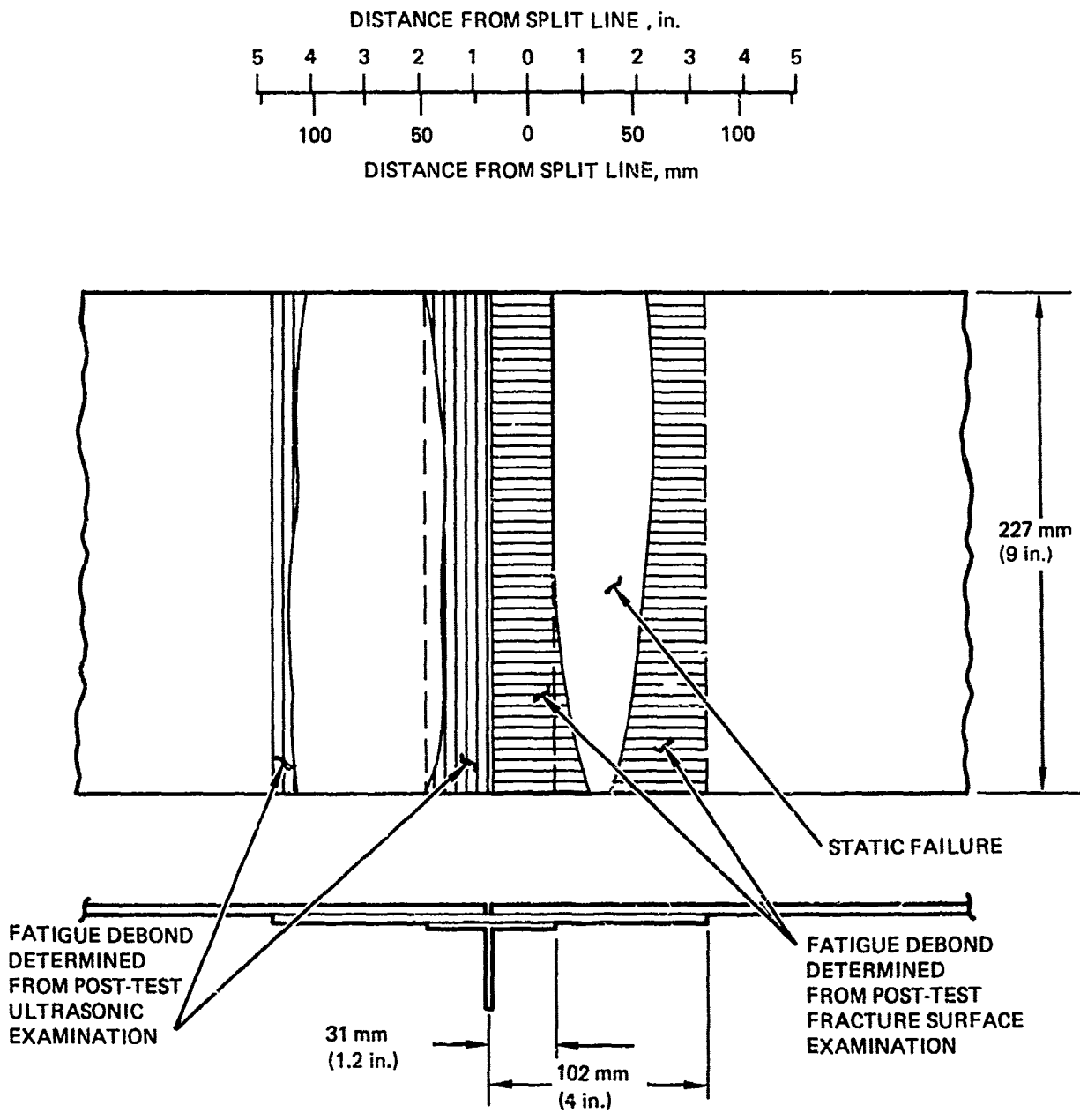


Figure 48. Final damage configuration, specimen A, No initial flaw

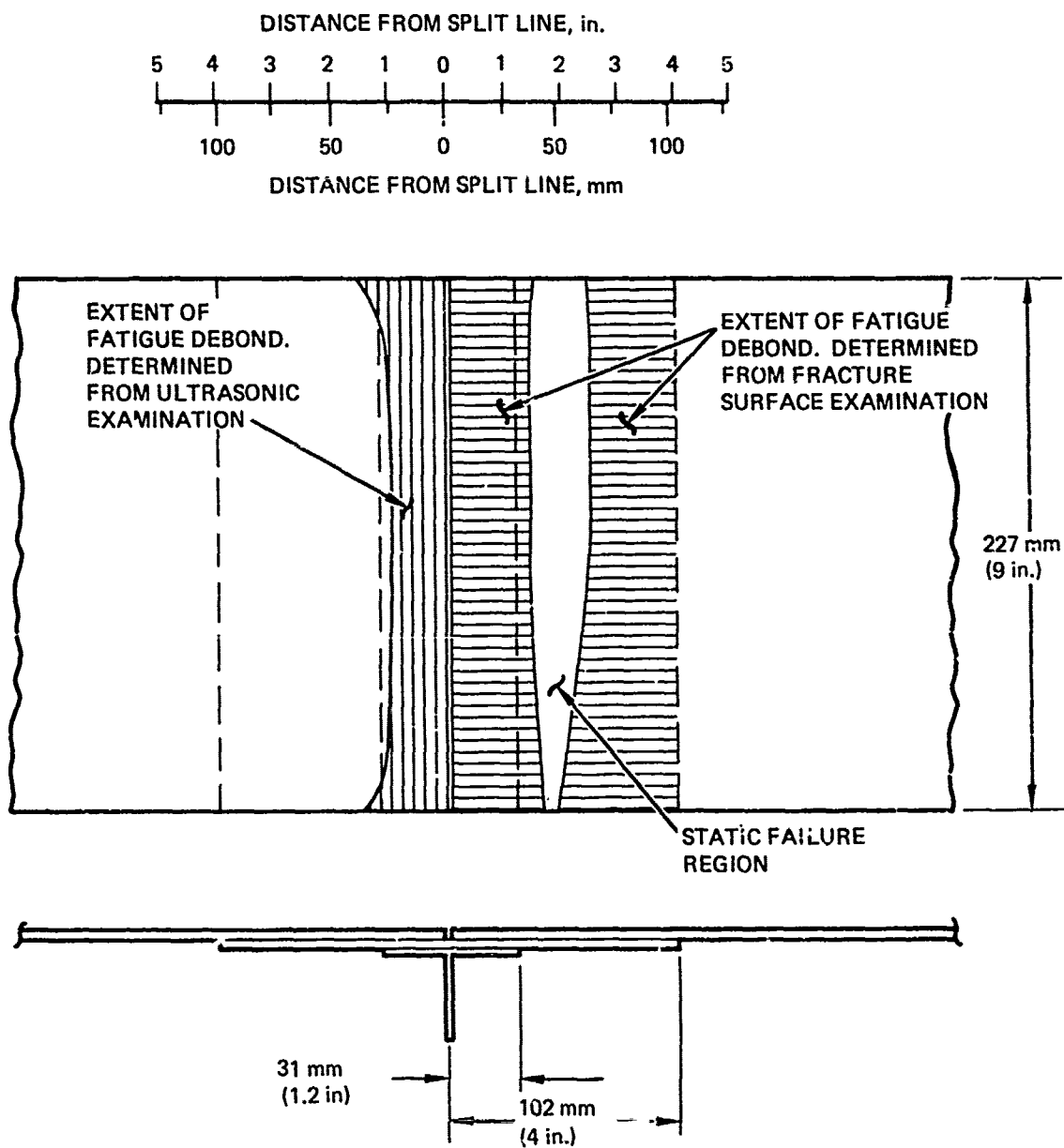


Figure 49. Final damage configuration, specimen B. No initial flaw

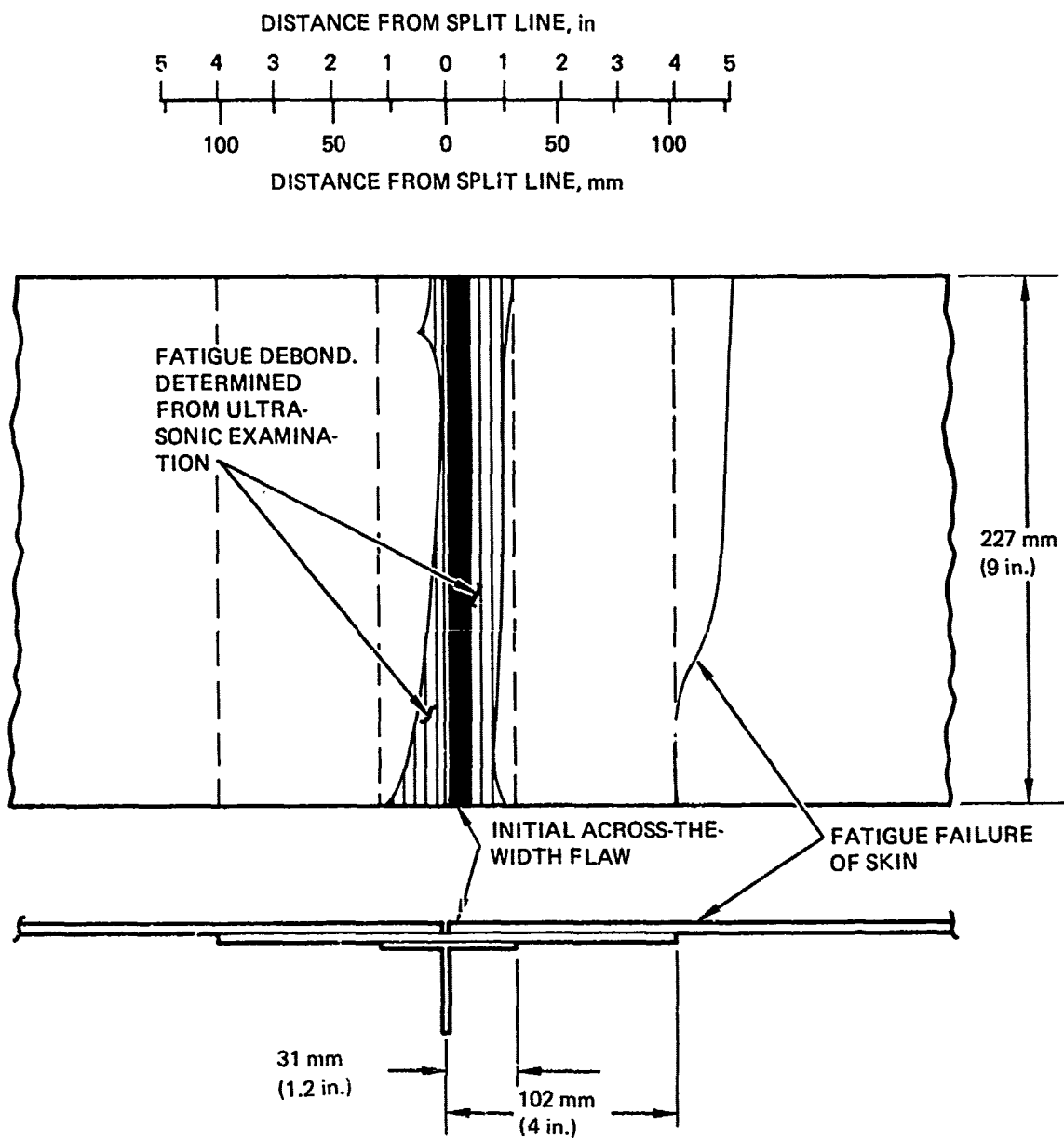


Figure 50. Final damage configuration, specimen C. Initial flaw is a 7.6 mm (0.3 in) deep across-the-width flaw

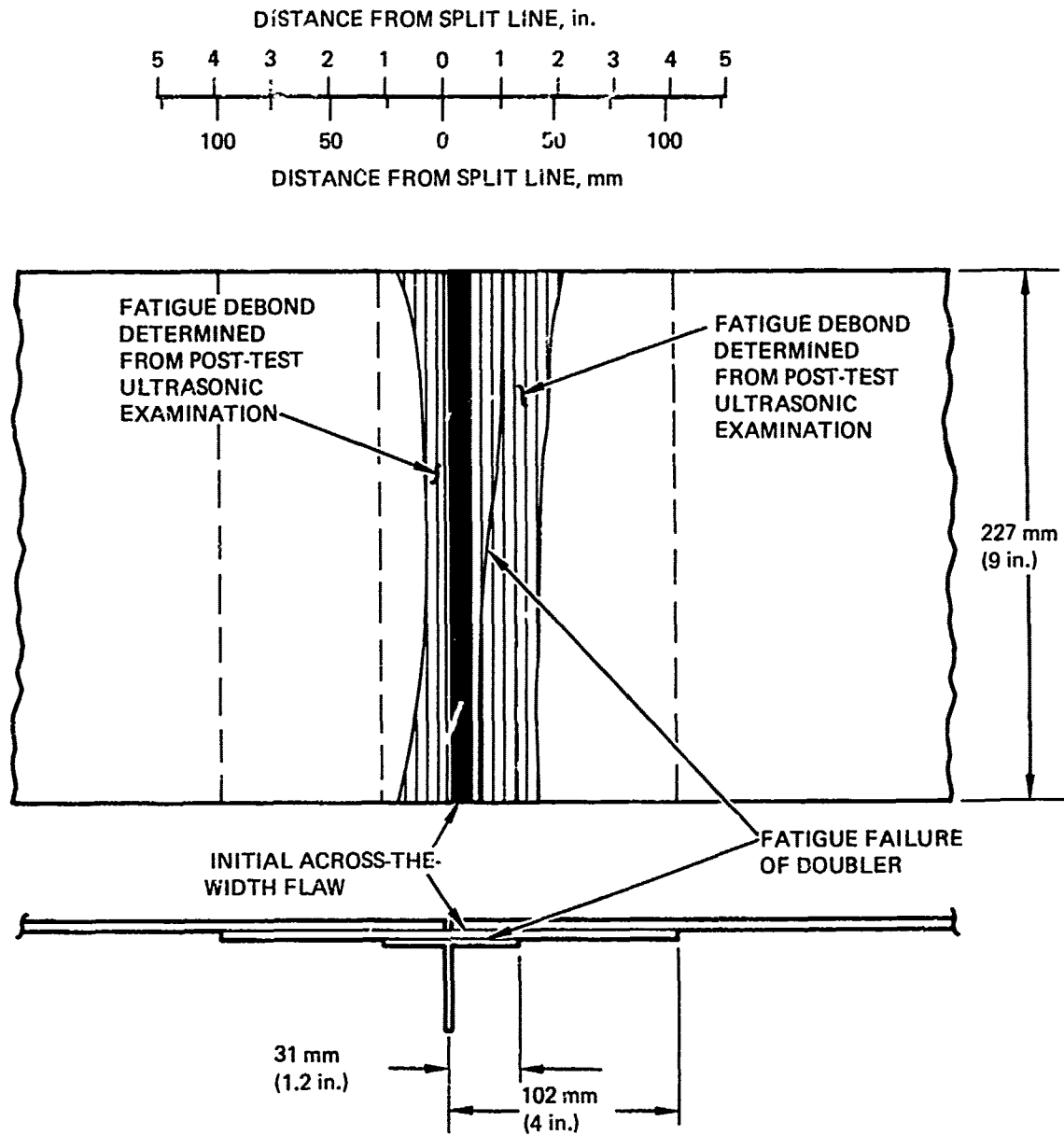


Figure 51. Final damage configuration, specimen D. Initial flaw is a 7.6 mm (0.3 in) deep across-the-width flaw

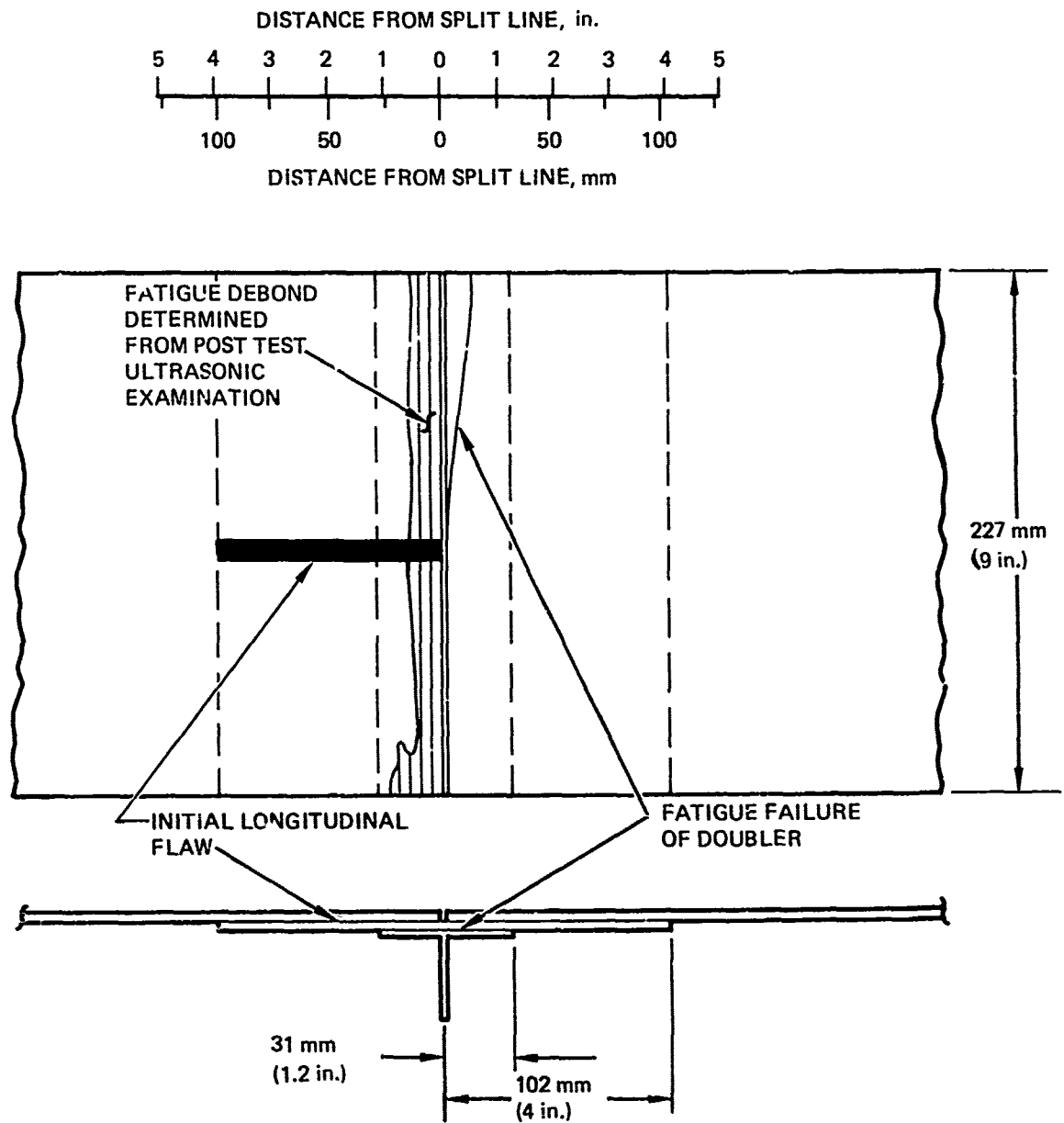


Figure 52. Final damage configuration, specimen E. Initial flaw is a 12.7 mm (0.5 in) wide longitudinal flaw at the center line

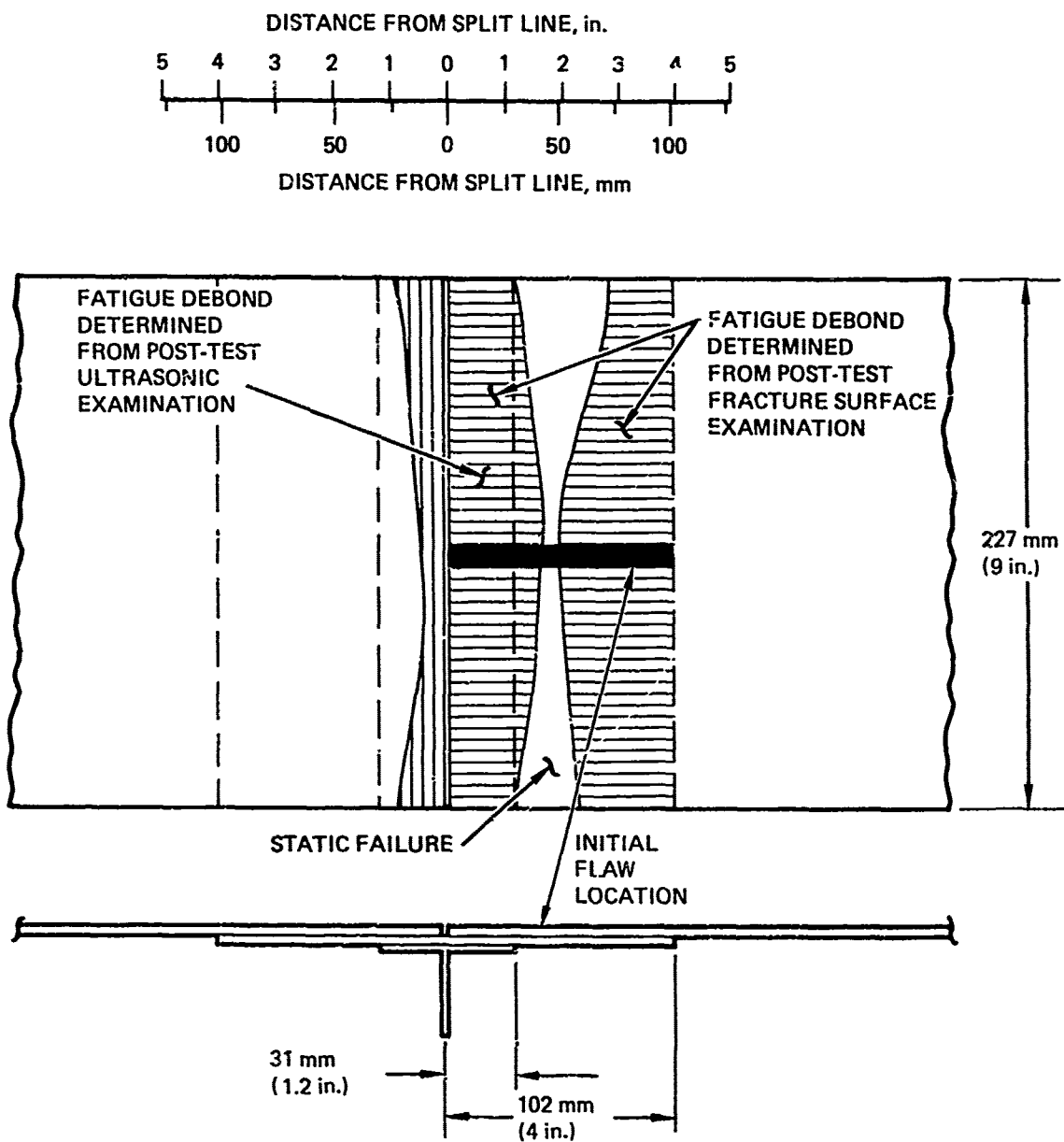


Figure 53. Final damage configuration, specimen F. Initial flaw is a 12.7 mm (0.5 in) wide longitudinal flaw

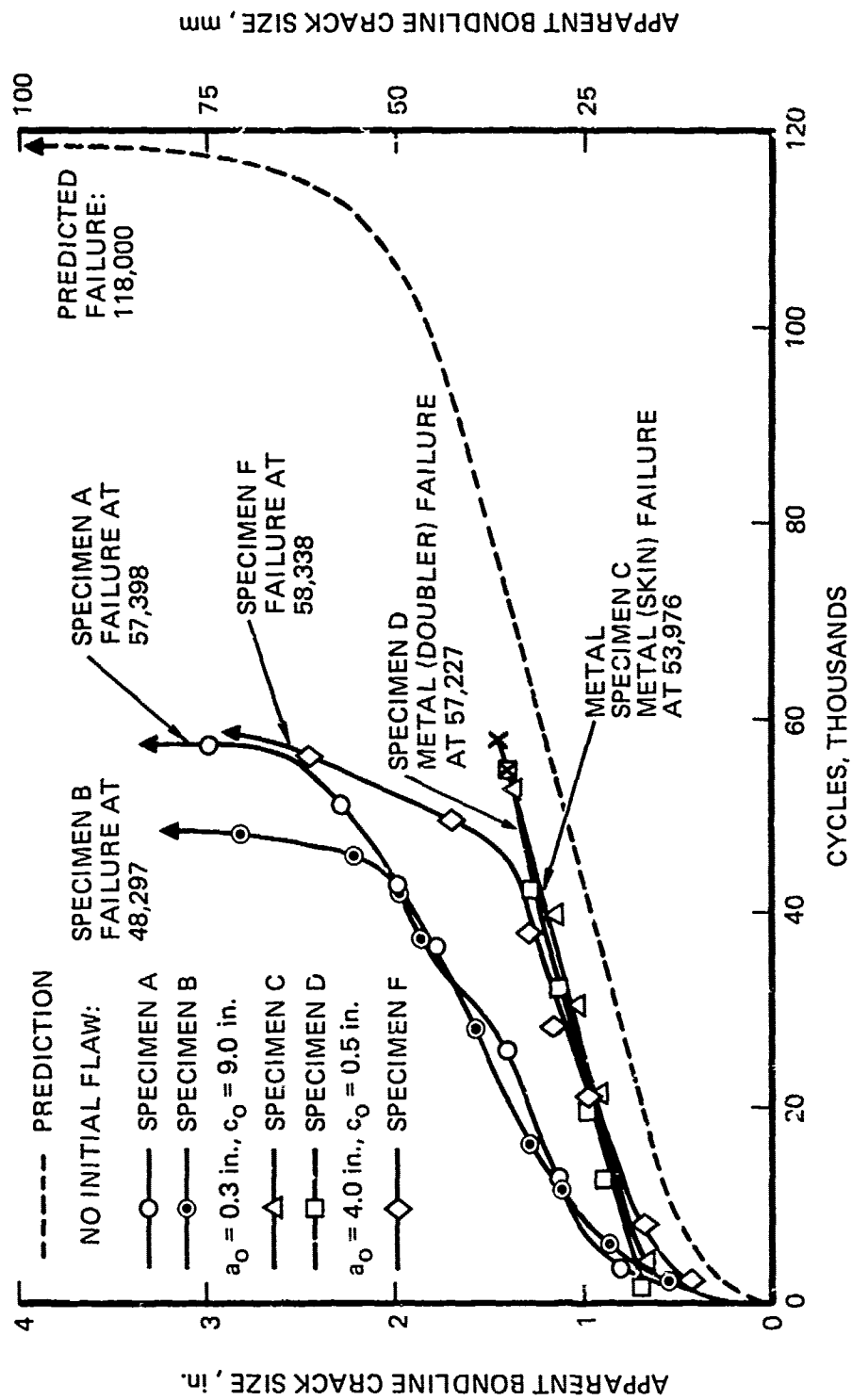


Figure 54. Predicted and experimental bondline crack growth

probable reason is that there were three or four separate bondline cracks in Specimens A and B but only two in preflawed Specimens C and D. Preflawned Specimen F also contained three cracks when it failed, but judging from the shape of its growth curve in Figure 54 the third crack may not have originated until after perhaps 45,000 cycles.

There is a notable absence of scatter in Figure 54 for specimens with similar initial flaws; that is, data from Specimens C and D matched each other as did data from Specimens A and B. The initial deflections were essentially equal; the growth curves coincided; and the final crack conditions at failure were similar in size and shape.

It must be pointed out that the data for Specimen A as plotted in Figure 54 have been adjusted. The Specimen A deflections as recorded in the raw data were lower than the deflections for Specimen B by a uniform factor of 2.0. These raw data when converted to crack length indicated unreasonably low crack sizes and growth rates, such as a final adhesive crack at failure of only 18 mm (0.7 in.). After review of all the facts and discussion with the operator who performed the tests, it is judged to be exceedingly likely that the calibration setting on the displacement gage plotter was half of the value recorded, and that the results for Specimen A as adjusted and as plotted in Figure 54 are correct.

The dashed line in Figure 54 is a crack growth prediction for the six test specimens. The predicted crack growth life was about twice the actual lives. In the prediction, it was assumed that only one bondline crack would grow. In the actual specimens up to four separate bondline cracks grew, two on each side of the split line. With two cracks propagating simultaneously across the same fracture surface, the time to fracture would be about half as long as in the single crack case. This is the approximate error in these predictions.

SECTION V

CONCLUSIONS AND RECOMMENDATIONS

Fracture mechanics methodology has been developed and experimentally demonstrated for the prediction of the growth of bondline flaws in adhesively bonded structure. This work is considered to be an initial step toward providing the technology required to assess the influence of possible pre-existing bondline flaws on the structural integrity of aluminum adhesively bonded fuselage structure.

Test procedures and analytical relationships for the Cracked Lap Shear (CLS) specimen are fully developed. The ratio G_I/G for this specimen is about 0.2, which is typical of many structural applications involving large area bonds. (The exact value of G_I/G depends upon relative adherend thickness and whether or not the specimen is side notched.) The value of G is independent of crack length, which simplifies the monitoring of tests. The specimen can be machined from large area bonded plates which are cured under exactly the same conditions as used for the structure, a feature not possible with the Mode I Contoured Double Cantilever Beam (CDCB) specimen. The CLS specimen as used is very long to maximize the applicability of a mathematical analysis which ignores end effects. Side notching has been a successful way to increase the stresses in the bondline so as to induce bondline cracking prior to metal failure. The use of the CLS specimen is strongly recommended for mixed Mode I and Mode II fracture mechanics testing of structural adhesives.

A Mode III fracture mechanics specimen for bondline cracks, the Modified Zero K-Gradient (MZKG) specimen, was increasing-load tested and fatigue tested. The cracks did propagate; however, the specimen has an undetermined amount of Mode I loading. Further study of the Mode III testing problem is recommended, especially to develop a mathematical analysis to estimate the G_I component in the MZKG specimen.

Increasing-load tests of 36 CDCB specimens resulted in a mean \mathcal{G}_{Ic} value of 2.19 kJ/m^2 (12.5 lb/in) with a standard deviation of 0.26 (1.5 lb/in) for the AF-55S adhesive system. Limited increasing load data on side-notched CLS specimens suggest that the addition of large amounts of \mathcal{G}_{II} loading does not significantly reduce the critical value of \mathcal{G}_I at the onset of crack instability. Because this high value of \mathcal{G}_{Ic} is maintained for mixed mode loading, structure bonded with AF-55S adhesive exhibits a very high resistance to crack growth in the adhesive layer when subjected to a monotonically increasing load in room temperature air. However, in Pure Mode I, fatigue crack propagation of bondline cracks can occur at values of $\Delta\mathcal{G}_I/\mathcal{G}_{Ic}$ of 0.1 or less, and the Mode II component has a definite detrimental effect on da/dN. Therefore, fatigue (and also environmentally-induced crack growth) tend to be the critical conditions for the adhesive system. It is recommended that greater emphasis be placed on fatigue and environmental effects in the fracture mechanics testing of adhesives.

Mode I stress corrosion cracking data for AF-55S adhesive and BR-127A primer in 333°K (140°F) water appear to show a strong dependence on adherend surface treatment method. Specimens prepared by FPL etch failed near the metal/primer interface. Specimens prepared by the Phosphoric Acid Anodize process failed cohesively within the adhesive, and the crack growth rates were up to 3 orders of magnitude slower at the same sustained value of \mathcal{G}_I . It was not possible to obtain a confident estimate of the threshold value of ISCC, due to practical limitations on test time.

The most important loading variable in the propagation of a bondline crack is \mathcal{G}_I , the Mode I component of strain energy release rate. However, fatigue testing of CDCB and CLS specimens has shown a significant effect of \mathcal{G}_{II} on da/dN. When da/dN data were plotted as functions of $\Delta\mathcal{G}_I$ only, the CLS data were segregated to the left of the CDCB data (that is, at higher da/dN values for the same value of $\Delta\mathcal{G}_I$). Based on these data an effective strain energy release rate, $\Delta\mathcal{G}_{\text{eff}}$, was defined in Equation (37) to account for the interaction of \mathcal{G}_I and \mathcal{G}_{II} on the fatigue crack growth rate in AF-55S adhesive. The empirical relationships between da/dN and $\Delta\mathcal{G}_I$ obtained from

Mode I testing can then be extended to mixed Modes I and II by replacing $\Delta\mathcal{K}_I$ with $\Delta\mathcal{K}_{eff}$. For other adhesives a slightly modified definition of $\Delta\mathcal{K}_{eff}$ may be needed, but the same general approach is expected to apply. In future testing of other adhesive systems it is recommended to test both Pure Mode I specimens and mixed-mode CLS specimens in fatigue and establish a specific definition of $\Delta\mathcal{K}_{eff}$ for use in data interpolation.

The slope of the plot of $\log(da/dN)$ versus $\log(\Delta\mathcal{K}_{eff})$ for adhesives is much steeper than that for metallic materials. This means that small changes in stress cause large changes in crack growth rate. Furthermore, small errors in estimated stress cause large errors in estimated crack growth life. This makes it difficult to design for finite life. Thus, estimation of $\Delta\mathcal{K}_{Ith}$, the no-growth threshold, is recommended as an important design parameter.

Crack growth threshold data are expensive to obtain because of the long test times required. This is even more true in adhesives than in metals because the adhesive is time dependent (so high-frequency values of $\Delta\mathcal{K}_{Ith}$ may be misleading), and because the increment of crack growth required for a confident reading of da/dN is substantially longer in adhesives than in metals. It is therefore recommended to estimate $\Delta\mathcal{K}_{Ith}$ by linearly extrapolating the da/dN curve downward in log-log space to a crack growth rate of 1 mm per year (1 inch per 25 years). Although probably conservative, this procedure tends to give a usable threshold value, by virtue of the steepness of slope of the da/dN curve.

The cyclic frequency effect on da/dN (particularly in laboratory air) is stronger for bondline cracks than is typical for cracks in metal. Thus, laboratory testing at high cyclic frequency has at least two drawbacks. First, the use of da/dN curves obtained at high frequency for prediction of crack growth in service at a slower frequency would be unconservative. Secondly, because the metal da/dN properties do not significantly improve with increasing frequency, testing at high frequency may cause metal failure before the bondline crack growth data can be obtained. For this research, use of a cyclic frequency of 3 Hz was a good compromise between the inapplicability of results obtained at high frequency and the costliness of testing at low frequency. Further study of time/frequency/environment interaction effects

and extended-time da/dN testing of adhesives is recommended to determine general guidelines for selection of cyclic test frequencies.

Crack growth rates from fatigue tests in 333^oK (140^oF) water were significantly faster than in laboratory air. Some fatigue testing in the extremes of the anticipated service environment is therefore recommended to obtain applicable baseline data for prediction.

Even with a preflaw in the adhesive layer there is a tendency for bonded thin-sheet structure to fail in the adherend. It is important to examine the conditions for crack growth in the bondline, even though the structural configurations considered lie outside the usual usage regime in design, so that margins of safety can be quantified. The following means were used in the simulated structural tests to increase the tendency for the bondline crack to propagate without adherend yielding:

- Increase the adherend thickness
- Increase σ_1 by increasing the induced bending moment at the crack tip
- Load in fatigue rather than by a single large increasing load
- Use a warm, moist environment.

The use of these means was successful in that nine of the 12 simulated structural specimens failed by fatigue crack growth in the bondline.

The bonded structural single lap joints exhibited very little sensitivity to initial flaw size. Some specimens were unflawed and some had initial across-the-width bondline flaws. The lives of all thick adherend specimens were within a factor of 2.0 of one another. Except for specimen E which failed prematurely due to an inadvertent machining flaw in the metal doubler, the lives of the thin adherend specimens were within a factor of 1.21 of one another. For the single lap joint geometry, the stress concentration at the gap of the joint is high, so a small flaw originating there grows rapidly at first and then decelerates. This phenomenon leads to crack growth lifetimes that are insensitive to flaw size. There may be other bonded structural configurations with flaw size sensitivity more similar to that of conventional metal structure with cracks in the metal. Further consideration

of flaw sensitivity is recommended to learn more about the importance of the initial size of bondline flaws.

Since the cracks could not be visually monitored, two methods of flaw growth monitoring were used in the structural tests, a direct contact ultrasonic method and a compliance method. The ultrasonic method utilized transducers in direct contact with the specimen. The compliance method measured periodically the opening displacement of the gap of the joint and compared it to finite-element-computed displacement estimates for a series of assumed crack lengths. The compliance method was more reliable and less expensive to use than the ultrasonic method, but the information on flaw shape and location obtained ultrasonically cannot be obtained by the compliance method:

A fracture mechanics method for predicting the growth of bondline flaws was demonstrated and evaluated. A finite element analysis was used to compute bending and axial stresses. From these, approximate values of G_I , G_{II} and ΔG_{eff} were estimated. Crack growth in the adhesive layer was then estimated using the baseline da/dN data. Calculations for the thick adherend specimens were completed after testing. However, those for the thin adherend specimens were done prior to testing. The predicted crack growth lives were about twice the actual lives. In the prediction it was assumed that only one crack would grow, but in the actual specimens two cracks propagated simultaneously in the same fracture surface. This could account for the factor of 2 error in the prediction. However, in light of the sensitivity of the adhesive crack growth process to small variations in estimated stress, larger errors than a factor of 2 could reasonably be expected for crack growth life predictions.

Continued efforts are recommended to apply linear elastic fracture mechanics theory for predicting the growth of bondline cracks in structural adhesive joints. As a continuation of the work reported herein, research is now in progress to extend the results to be applicable to the PABST program. Baseline data are being generated and the methodology is being tested using the selected PABST adhesive, FM-73. This work will demonstrate the generality of the baseline testing and analytical methods and will provide data specifically applicable to the PABST program. Further research will be required to

extend MIL-A-83444 to apply it to bondline flaws. These future efforts should include development of criteria for initial flaw size and type, and evaluation of the impact of such criteria on the design of bonded structure.

REFERENCES

1. Adkinsson, R.E., and Deneff, G.V., "Analytical Investigation of Medium STOL Transport Structural Concepts," Douglas Aircraft Company, McDonnell Douglas Corp., Technical Report AFFDL-TR-74-109, Volume 1, AD-8005-818, N7S-28060, August 1974.
2. McCarty, J.E., "Advanced Metallic Cargo Fuselage Design for Improved Cost, Weight, and Integrity," Boeing Commercial Airplane Company, Technical Report AFFDL-TR-73-53, June 1973.
3. Ripling, E.J., Mostovoy, S., and Patrick, R.L., "Application of Fracture Mechanics to Adhesive Joints", STP 360, ASTM (1963).
4. Ripling, E.J., Mostovoy, S., and Patrick, R.L., "Measuring Fracture Toughness of Adhesive Joints", Materials Res. and Stds., ASTM, Vol. 64, No. 3 (1964).
5. Mostovoy, S., Crosley, P.B., Ripling, E.J., "Use of Crack-Line Loaded Specimens for Measuring Plane-Strain Fracture Toughness", J. of Materials, Vol. 2, No. 3, ASTM, (1967).
6. Ripling, E.J., Corten, H.F., and Mostovoy, S., "Fracture Mechanics: A Tool for Evaluating Structural Adhesives", J. Adhesion, Vol. 3, pp 107-123 (1971). (Also published in SAMPE Journal, 1970.)
7. Mostovoy, S. and Ripling, E.J., "Fracturing Characteristics of Adhesive Joints," Final Report, Contract No. N00019-75-C-0271, for the period January 16, 1975 through January 16, 1976, Naval Air Systems Command.
8. Clark, H.T., "Definition and Nondestructive Detection of Critical Adhesive Bond-Line Flaws," PABST Industry Review Book 2, Douglas Aircraft Company, McDonnell Douglas Corporation, Long Beach, Calif. Oct. 5-7, 1976.
9. Hart-Smith, L.J., "Analysis of Bonded Joints," PABST Industry Review Book 3, Douglas Aircraft Company, McDonnell Douglas Corporation, Long Beach, Calif., Oct. 5-7, 1976.
10. Wang, S.S., Mandell, J.F., and McGarry, F.J., "Fracture of Adhesive Joints," Research Report R76-1, Dept. of Material Science and Engineering, MIT, Cambridge, Mass., Feb. 1976.